POLITECNICO DI TORINO

Master's Degree in Electronic Engineering

Politecnico di Torino

Master's Degree Thesis

Scalability of Electrode Supercapacitor Technologies

Supervisors

Prof. Andrea LAMBERTI

Dott. Pietro ZACCAGNINI

Dott.sa Mara SERRAPEDE

Candidate

Paolo GARDIOL s305891

March/April 2024

Summary

Supercapacitors, also known as electrochemical capacitors, have gained significant attention due to their high power density, rapid charge-discharge cycles, and long cycle life. However, while their features are well-established in small-scale devices and laboratory settings, transitioning to large-scale production poses significant challenges. This thesis focuses on the scalability aspects of supercapacitor electrode technology through a roll-to-roll (R2R) process, in which water-based slurry are used as the main vehicle for coating.

In first analysis the rheology of the slurries was under investigation, in order to extrapolate information about how the slurry behaves when it's disrupted. Properties such as viscosity, viscoelasticity and time response to a shear stress are useful parameters that define the quality of the coating in a R2R process. The goal was to reproduce an ink slurry, considered as a reference for the R2R coating, with different material and improve its recipe so that it'll be repeatable.

As a factor for improving the electrode's performance, the calendering step has been taken into consideration. The purpose of calendering is to enhance, by heat compression, the adhesion between electrode surface and current collector and reduce the porosity of the substrate, mainly for refine the electrode's structure and decrease internal parasitic resistance. The study was made to define the effectiveness of this step in terms of actual improvements and time required to perform it.

The electrodes taken into account for the scaling process are different in terms of physics working principle: Electrical Double Layer Capacitor (EDLC) and Pseudo-capacitor (PS). Activated carbon was used as EDLC active material, in particular the coconut-shell derived YP series, provided by the manufacture Kuraray Coal™, as it can provide high surface area per active material. Transition metal-oxide MnO_2 was the choice for the pseduo-capacitive one, whose synthesis was performed in laboratory by mixing $MnSO_4 \cdot H_2O$ and $KMnO_4$ in water solution.

First, the manufacture and characterization of electrodes was made in a laboratory environment, for extrapolate reference parameters like specific capacitance and bias window potential, and in order to compare them with the actual State of the Art. With the prospect of higher-performance and lower cost devices, with a

environment friendly outlook on the use of materials, the K-ion device idea was selected for this thesis. The choice of KPF_6 as the electrolyte salt was made for its properties and availability. Symmetric and asymmetric configurations, with the same electrode or different one, were also tested in order to define which is the best in terms of performance, first in small devices and then in bigger one where the electrodes manufacture were made with a R2R machine. As a future perspective in the field of supercapacitor, it was investigated the concept of hybrid configuration, in which a EDLC/PS electrode was combined with a battery-like one; in this case, carbon-black C65 was considered as active material.

Acknowledgements

In primis desidero ringraziare il professor Andrea Lamberti, nonchè mio relatore, che mi ha introdotto queste tematiche recenti e dalle quali si è sviluppata la tesi. L'energia e l'innovazione che mi ha trasmesso mi ha permesso di sviluppare una visione del mondo scientifico totalmente nuova.

Un sentito ringraziamento va al dottor Pietro Zaccagnini e alla dottoressa Mara Serrapede, correlatori di questa tesi, per il loro inquantificabile contributo e supporto quotidiano verso questo percorso sperimentale. L'intraprendenza, le conoscenze e la dedizione che mi hanno trasmesso sono state di importanza immensa per me e ne farò immensamente tesoro per ciò che verrà.

Un doveroso ringraziamento va al gruppo di ricerca del DISAT, per la partecipazione indiretta e non allo svolgimento della tesi, per l'integrazione che ho fin da subito ricevuto e per tutti i momenti di gioia e felicità a cui ho assistito e partecipato. L'altruismo e la passione che hanno dimostrato sono stati il motore che mi ha sempre permesso di affrontare le difficoltà con il sorriso.

I miglior ringraziamenti vanno alla mia famiglia, che mi ha sempre sostenuto durante il mio percorso universitario, che mi è sempre stata vicina e che mi ha sempre amato in ogni momento della mia vita. Siete stati sempre i miei fan numero uno, a credere sempre in me anche quando non riuscivo a credere in me stesso.

Ringrazio i miei nonni, i miei zii e i miei cugini per il loro affetto, la comprensione e l'interesse che hanno dimostrato durante il mio percorso universitario.

Un ringraziamento va ai miei amici, quelli con cui ho condiviso e trasmesso le mie felicità, le mie angosce e i miei successi e fallimenti.

Un ultimo ringraziamento lo rivolgo a tutte quelle persone che ho incontrato durante questi anni accademici, tra professori e colleghi, con i quali ho avuto modo di plasmare le mie conoscenze e il mio interesse verso il mondo scientifico.

Una dedica speciale va alle persone che al di fuori del percorso universitario mi hanno permesso di vivere, gioire, sorridere, amare, sognare, semplicemente a ricordarmi che, in fondo, sono un essere umano.

A coloro che nella scienza trovano il sapere, nel mondo la bellezza di ogni cosa, nell'amore il principio della vita.

Paolo Gardiol

Table of Contents

List of Tables

List of Figures

Acronyms

SC
Supercapacitor

EDLC
Electrostatic double-layer capacitor

PC
Pseudo-capacitor

HC
Hybrid capacitor

R2R
Roll-to-roll

SoA
State of the Art

FESEM
Field Emission Scanning Electron Microscopy

XPS
X-ray Photoelectron Spectroscopy

CV
Cyclic Voltammetry

OCP
Open Circuit Potential

EIS

Electrochemical Impedance Spectroscopy

GCD

Galvanostatic Charge/Discharge

ESW

Electrochemical Stability Window

ESR

Equivalent Series Resistance

IR

Internal Resistance

WE

Working electrode

CE

Counter electrode

Ref

Reference

CS

Cyclic Stability

FT

Float Test

SB

Springback

DI

De-ionized

AC

Activated Carbon

CMC

Carboxymethyl cellulose

OCE

Oversized Carbon Electrode

CB

Carbon-black

C/D

Carge/Discharge

Chapter 1

Introduction

1.1 Supercapacitor: an overview

A supercapacitor (SC), also known as ultracapacitors or electrochemical capacitors, is an energy storage technology that belongs to the family of electrochemical storage device. Traditional SCs store and release energy through the physical separation of charges, like capacitor, but they can exploit reversible reaction (pseudo-capacitance) in order to achieve higher energy density. This approach allows them to bridge the gap between conventional capacitors and rechargeable batteries, and, to better understand this difference, it would be useful use parameters as energy and power density plotted in a Ragone plot (fig. 1.1). SCs can deliver high power density, as an electrolytic capacitor, with a good compromise in terms of energy storage, like a battery.

As technological advancements continue to push the boundaries of energy storage, the trajectory of research leans towards hybrid solutions (explained later) that harness the strengths of both SCs and batteries. The Ragone plot, as a dynamic tool, not only emphasizes the existing disparities but also underscores the potential for integration, forming the way for a future where energy storage devices strike a balance between energy and power density.

Additional advantages of this technology are high cycling life, mainly related to the physics of charge/discharge, and low heat production, as the electrodes that make up the SC have low equivalent series resistance (ESR), affording to the device high current rate. The second feature is a huge inconvenience when comes up the scalability of the electrode, as the industrial processes differ from the ones made in laboratory.

The structure of a SC consists of two electrode, with their current collector, separated by a separator soaked in electrolyte. As the layout is the same for all, they differ from each other based on the principle of physical operation, listed

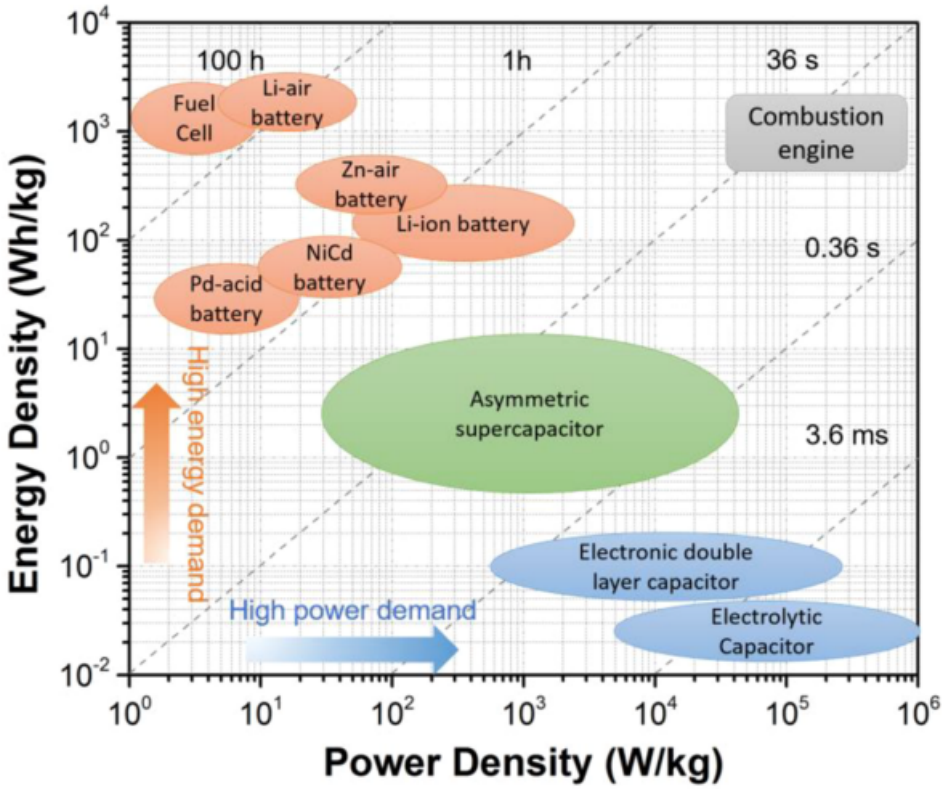

Figure 1.1: Ragone Plot [1], which graphically represents the trade-off between energy (x-axis) and power (y-axis) density of different energy storage technologies

below:

- **Electrostatic double-layer capacitor** (**EDLC**): involves the physical separation of charges at the electrode-electrolyte interface, forming an electric double layer, and this process occurs rapidly, allowing energy storage/release quickly;

- **Pseudo-capacitor** (**PC**): a phenomenon where redox and reversible reactions take place at the electrode-electrolyte, contributing to additional charge storage;

- **Hybrid capacitor** (**HC**): combine the characteristics of both EDLC and pseudo-capacitors.

1.1.1 Electrostatic double-layer capacitors

The electrostatic double layer is a consequence of the interaction between charges at the electrode surface and ions present in the electrolyte. When a voltage is applied across the supercapacitor, two layers of opposite charges are formed, respectively one to the electrode surface and the other to the liquid boundary, separated by an atomic distance (order of Å), in such a way that a capacitor is built. As the device presents two electrode in series, the overall capacitance of it is the parallel of the two electrode capacitance, approximately assumed equal.

This model was presented by the physics Hermann von Helmholtz [2], however some working principles aren't explained in that simplified theory, so more studies where made in order to complex the physics behind (showed in Figure 1.2). The contribution of the physics Gouy and Chapman led to consider an inhomogeneous distribution of ions, modelled by the Poisson-Boltzmann theory [3], since the ions aren't located in static and compact array but are affected by thermal fluctuation. O. Stern, in particular, proposed the existence of an additional layer beyond the initial compact Helmholtz layer where ions distribution is better described in terms of adsorption, in contrast to the layer next to this where the Gouy-Chapman model is optimal. Due to that assumption, the interface is split into two, leading to two series capacitor, a Helmotz compact one (C_H) and a diffusion one (C_{diff}) [2], meaning that the overall double layer capacitor is:

$$\frac{1}{C_{dl}} = \frac{1}{C_H} + \frac{1}{C_{diff}} \tag{1.1}$$

To complete the model, Grahame extended Stern theory adding the nature of the cations and anions of the electrolyte, like the size and polarization, leading to a subdivision into three layer, the Inner Helmotz Plane (IHP), Outer Helmotz Plane (OHP) and the diffusion plane, mainly related to the closest distance from the electrode surface [2].

1.1.2 Pseudo-capacitors

Pseudocapacitance is a phenomenon observed in materials that exhibit reversible faradaic redox reactions at the electrode-electrolyte interface.

During the charging and discharging cycles, ions from the electrolyte either insert themselves into the crystal lattice of the electrode material or undergo reversible redox reactions on the surface of the electrode. As ions are passing into the substrate, electrically speaking it's flowing some current, phenomena that happen in a battery system, but instead of forming new compounds the ions are limited in forming new bonds where the energy is stored. Transition metal oxides, like ruthenium oxide RuO_2 or manganese dioxide MnO_2[2], are among the

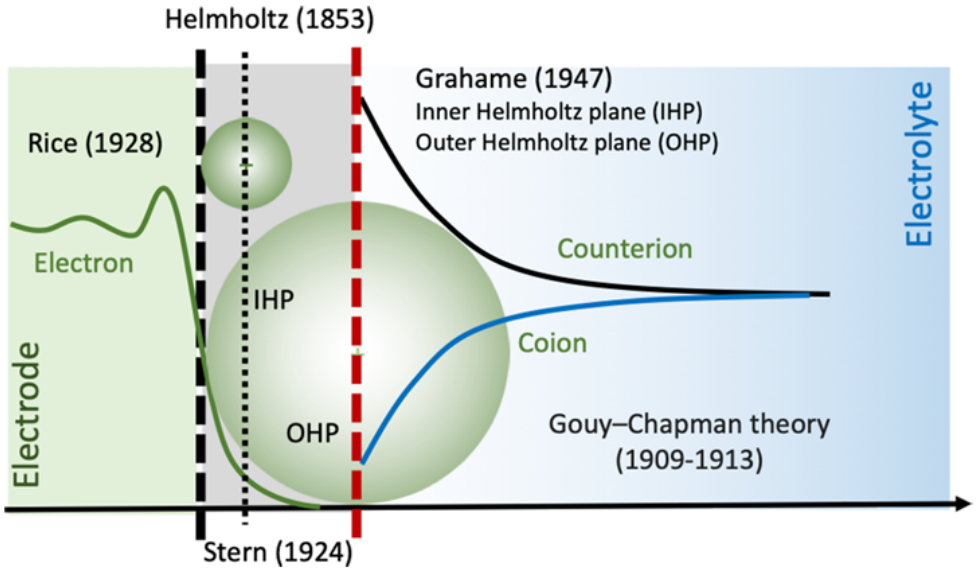

Figure 1.2: Model of EDLC [3]; include all the theories developed in history (Helmotz, Grahame, etc.).

materials renowned for their pseudocapacitive characteristics, taking into account the multiple oxidation states that can have.

Pseudocapacitors offer a host of advantages over traditional capacitors, as the redox reactions incorporation allows for a higher capacitance, so increased energy density. The reversible nature of these reactions ensures excellent cycle life, but due to the faradaic nature of the process, it can provide a lower power density w.r.t a electrostatic one.

1.1.3 Hybrid capacitor

The fundamental operation of hybrid capacitors (HCs) hinges on the utilization of both electric double-layer capacitance and pseudocapacitance within a single device. The combination of rapid physical separation of charges at the electrode-electrolyte interface with reversible faradaic redox reactions into the system allows swift energy storage and release with a good compromise with its density. This versatile combination makes hybrid capacitors suitable for a wide range of applications where both high power and energy density are crucial, like in the automotive field.

Metal ion based HCs, particularly, have come to the foreground in recent years. It comes with a series of properties, such as cost-effective, safety and environmental benignity that can also connect features of batteries and SCs[4]. Inspired by the line of Li-ion batteries, in this thesis it's explored the behaviour of HCs based on

K-ion, since Li has caused rising concerns on its sustainability and the mining process, while the choice of potassium originates from its large abundance in the Earth's crust and its natural recyclable element[5].

1.2 Roll-to-roll electrode process

In the realm of electrode manufacturing, especially in the production of batteries and capacitors, the roll-to-roll (R2R) process with metal foil as the wrapping material, i.e. aluminum and copper, stands as a cornerstone of efficiency, precision, and scalability. This continuous manufacturing technique streamlines the production of electrodes, facilitating the scalability of energy storage devices production. A simplified scheme of the complete process is reported in figure 1.3.

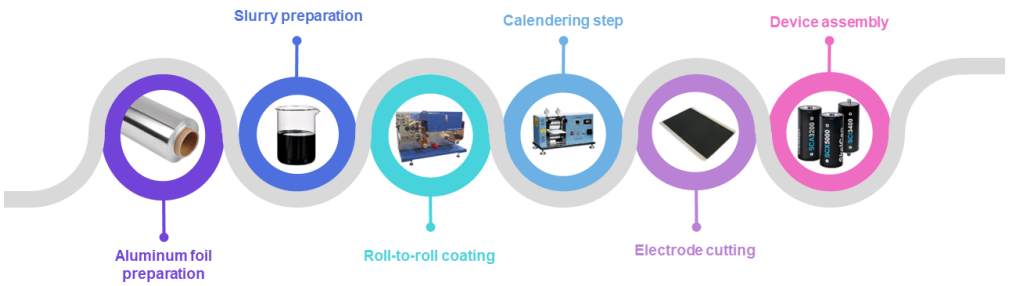

Figure 1.3: Process flow of the supercapacitor device in a roll-to-roll system.

The R2R process initiates with the unwinding of a large roll of aluminum foil into multiple roller that act as guide, (un)reeling and/or coating. This foil is typically a thin, flexible sheet, that act as the current collector of the device. The use of aluminum foil brings several advantages, including its lightweight nature, excellent conductivity, and compatibility with active material, however aluminum can be replaced with copper, especially in battery system, according to the working principle of the electrode (anode/cathode).

As the aluminum foil advances through the R2R system, it undergoes coating step, involving the application of a "slurry", a mixture of electrode active materials into a solvent, which can be organic or water-based. The choice of electrode materials depends on the specific type of energy storage device being manufactured. Common materials include active materials, conductive additives and binders. The

uniformity of the deposition is related mostly to the precision of the machine, but recent analysis defined the rheology of the slurry a crucial factor.

Following the coating step, the foil passes through drying station. This stage is essential to remove solvents or other liquids present in the coating. Drying ensures that the electrode materials adhere firmly to the current collector.

Calendering, a mechanical process involving the compression of the coated aluminum foil, follows the drying stage. This step contributes to the desired thickness, density, and smoothness of the electrode. Also, it can improve the adhesion between the electrode and the foil, which is a dominant feature in defining its ESR.

Once the aluminum foil has traversed the entire R2R process, complete with coating, drying and calendering, the resulting electrode material is rewound into a roll. This final roll of electrode material can then be used in subsequent manufacturing steps to assemble energy storage devices, or also to proceed with an additional coating in the opposite face of the foil, in order to produce a multi-layer device.

1.2.1 Viscosity

Viscosity is a measure of a fluid's internal resistance to flow. In the context of slurries used in electrode manufacturing, viscosity characterizes the ability of the mixture to spread and adhere uniformly to the electrode substrate. The viscosity of a slurry is influenced by factors such as the concentration of solid particles, the properties of the liquid medium, and the temperature. Understanding the viscosity is crucial, as it directly impacts the coating process and, subsequently, the uniformity and performance of the electrode. Viscosity is often measured using units such as centipoise (cP) or pascal per seconds ($Pa \cdot s$). Generally speaking, low viscosity slurries flow more easily, resembling a viscous liquid, while high viscosity ones exhibit greater resistance to flow, behaving more like a elastic solid[6].

Rheology is the scientific study of the flow and deformation of materials, encompassing both liquids and solids. In the context of slurries, rheology plays a crucial role in understanding and characterizing the flow behavior, viscosity, and overall mechanical properties of these complex mixtures. It provides valuable insights into how slurries respond to various forces, such as shear stress, force applied parallel to the material's surface, and conditions, like temperature.

1.2.2 Calendering

Calendering, a mechanical process widely used in various industries, also plays a critical role in the manufacture of supercapacitor electrodes. The calendering process is instrumental in shaping and enhancing the properties of materials to

achieve optimal electrode characteristics. It involves passing a material through two or more rolls to modify its thickness, surface texture, and porosity, which can define how wettable the electrode is to electrolyte.

The core of the calendering process lies in the rolls. These rolls can have specific surface features, diameters, and temperatures to achieve desired modifications in the electrode material; they exert pressure on the slurry-coated substrate, compressing and shaping the electrode material. The pressure applied reduces the thickness of the electrode material while influencing its porosity.

In addition, the rolls can be heated, making the substrate more pliable, so more susceptible to pressure, enhancing the process. In specific system, instead of controlling the applied pressure, the variable under control is the thickness itself, so the gap between the rolls is adjust in order to achieve the desired one; despite the simplicity, it's more dependent on the elastic properties of the electrode, since the applied pressure is constant[7].

1.3 Aim of the thesis

The aim of the thesis is create different final devices, whose electrodes are manufactured with R2R process, and compare them in terms of power and energy density, and suitability for scalability in an industrial environment. According to the evaluated performance and their position in the Ragone plot, it'll be possible to define which field can be suitable for them, i.e. automotive when high power density is available or portable device if it can provide high energy density.

As a starting point the slurry preparation is investigated in order to evaluate possible modifications to be implemented for an industrial process. This investigation includes the proportion of each single component, the amount of solvent, the time of preparation and so on.

The electrodes are first manufactured in a laboratory environment, with manual technique and in small quantity with respect to (w.r.t) a bulk process, looking for how to scale up each steps. Then the electrodes are characterize, using method that are explained later, for extract all the information related to them and make a comparison with the actual State of Art (SoA).

The electrodes are then combined together for building small device (i.e. button cell), where a first evaluation is made for defining if the device works properly and it's worth it to be scaled up for a bigger device. This step is crucial, since all the properties must be replicated in the industrial process, such as electrode thickness and weight, and strength and flexibility of the coating. The choice of the separator is included in these tests.

Finally, all the steps under investigation are replicated in a industrial-like environment, defining if the device can be scaled up without going beyond the

laboratory expectation. It's still not a complete industrial process, since all the passages aren't made by a single machine, so the overall process is semi-automated.

Chapter 2

Characterization technique

In this chapter are described various analytical as well as electrochemical techniques for the characterization of electrode materials to be used in a final devices. These methods are related to specific area of interest, which in some cases they are combined each others[8]. There are analytical characterization methods based on electron microscopy, which analyzed properties such as the size, shape, morphology and crystalline structure of the materials employed, i.e. Scanning Electron Microscopy (SEM). Analysis on the structures, compositions and definite physical properties of the electrode materials are defined by X-ray spectroscopy. Furthermore, electrochemical techniques such as Cyclic Voltammetry (CV), Electrochemical Impedance Spectroscopy (EIS), and Galvanostatic Charging/Discharging (GCD) are employed to study the electrochemical performance of electrode materials, usually referred to three main parameters: the overall (total) capacitance C_T, the electrochemical stability window (ESW) ΔV and the cell impedance. In addition, as the viscosity of the slurry mainly affect all the features described before, rheology analysis is needed for providing parameters of quality of the mixture.

2.1 Electrode model and characterization

To better understand how an electrochemical measurement works, it's helpful to describe the working principle of an electrode in terms of equivalent circuit. According to the working principle of the electrode, this model can change as the physics behind change. A simplified EDLC electrode is presented in Figure 2.1. The ESR represents the ohmic resistance of the electrolyte and electrode materials, and it's the main factor of the losses. Following, a parallel between a non-ideal capacitance, Q, called also Constant Phase Element (CPE) and a charge-transfer resistance in parallel, denoted as R_P, is related to the kinetics of ions and may include the resistance of any Faradaic reactions occurring at the electrode surface.

The Warburg impedance, Z_W, is associated with diffusion processes of ions within the electrode material, particularly in porous structures, allowing the formation of the double-layer structure. Finally, a double-layer capacitance C_{dl} define the overall capacitance of the electrode, where the charge is stored.

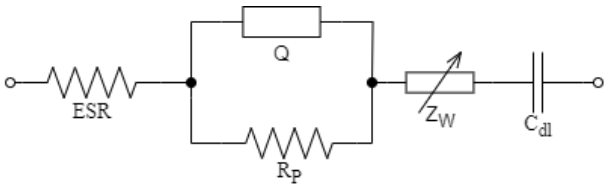

Figure 2.1: Simplified electrode-electrolyte equivalent circuit in a EDLC interface. The ESR and CPE elements depend essentially on the specific material used for electrode and electrolyte[9].

Of course this model isn't valid for all the electrode, since it doesn't include element that explain pseudocapacitance or Faradic charge transfer. Equivalent circuit showed in Figure 2.2 explains the pseudocapacitance contribution in a simplified way. The pseudo-capacitance C_P is in parallel with the double-layer one and it has in series a Faradaic resistance R_F, which corresponds to the reciprocal of the potential-dependent charge-transfer rate in the pseudocapacitance processes. Their contribution is usually related to a single (or more) semicircle in the high frequencies range in a Nyquist plot (explain later). When overcharge occurs, a continuous Faradaic reaction takes place[2] leading a constant non negligible current leakage and this contribution is defined by a Faradaic impedance, $R_F^{'}$, in parallel to C_P.

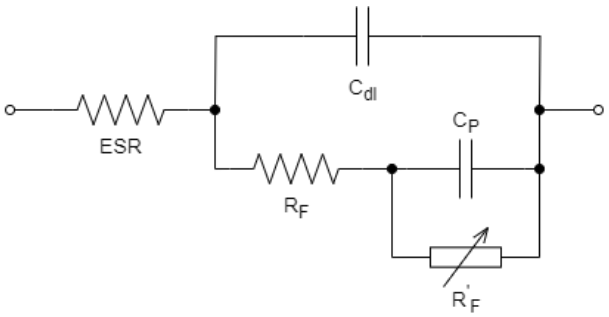

Figure 2.2: Simplified electrode-electrolyte equivalent circuit of a PS electrode.

2.1.1 Three electrode characterization

The three-electrode configuration in electrochemical characterization, particularly in the context of supercapacitor electrodes, allows for detailed investigations of the electrochemical mechanisms and properties, such as capacity, coulombic and energetic efficiencies, and internal resistance. The three electrode system consists of a working electrode (WE), counter electrode (CE), and reference electrode (Ref).

The working electrode represents the material under investigation, where the electrochemical reactions, such as charge storage and release, take place. The counter electrode completes the electrical circuit and serves as a counterpoint to the working electrode, facilitating the flow of current during electrochemical processes. The reference one's role is to act as a reference in measuring and controlling the working electrode potential, without passing any current, and should have a constant electrochemical potential at low current density. Additionally, since the reference electrode passes negligible current, the IR drop between the reference and working electrode is often very small, leading to a more stable potential. This translates into superior control over working electrode potential.

Block diagram in Figure 2.3 explain of a three electrode measurement works. A signal generator generates the voltage (potentiostatic mode) or current (galvanostatic mode) signal, according to the type of measurement, and send it to a control amplifier, whose role is to adjust the amplitude and compare it with the reference potential, if needed. The electrometer measures the potential difference between reference and working electrode; it's accurate to consider that this difference is related to the material of the reference, as changing it will change its value, so when reported must be included the typology of the reference electrode. The current that flow in the system is measured by a I/E gain unitary converter, using a fixed and known resistor R_m.

2.1.2 Two electrode characterization

The two electrodes measurement is used to characterize the final device. Since both the electrodes are characterized, the device can be assembled and an overall voltage, evaluated in the three electrode measurement, can be applied between the two electrodes. In this configuration, the reference and the counter electrode are linked together to the cathode, instead the other electrode is represented by the working electrode, alias the anode. Major data that can be evaluated are energy and power density, correlated also to capacity retention, cyclic stability and resistance to float test.

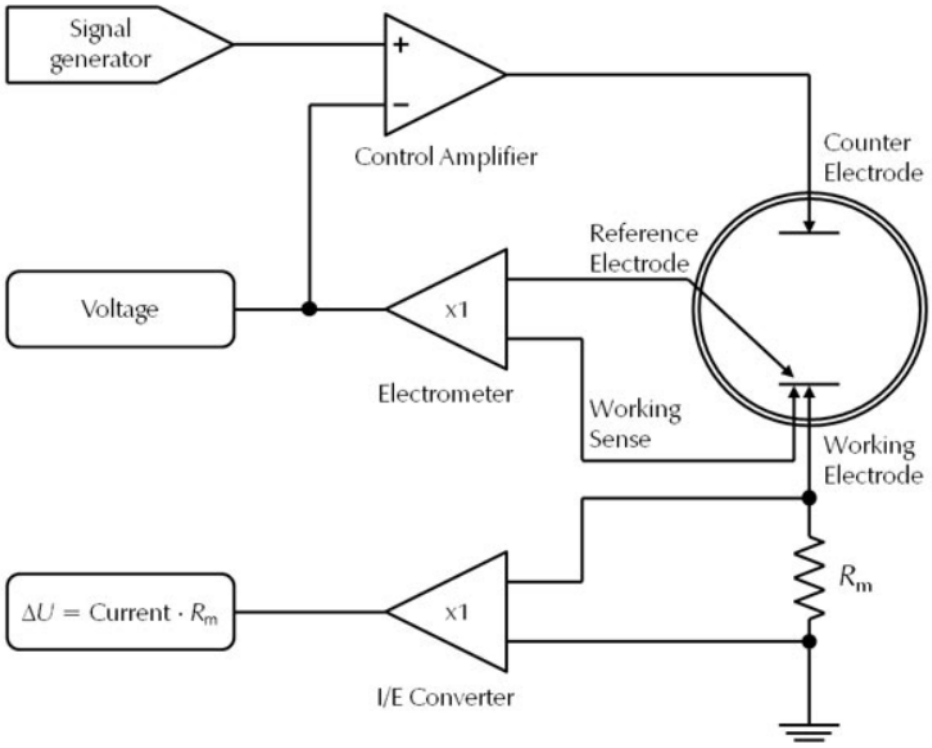

Figure 2.3: Block diagram of a potentiostat for electrochemical characterization at three electrode.

2.2 Electrochemical measurement

In detail are explained the electrochemical measurement techniques that can be used for the characterization of the SCs, both in three electrode and two electrode system: the Cycling Voltammetry (CV), Galvanostatic Charge and Discharge (GDC) and Electrochemical Impedance Spectroscopy (EIS). In addition to GCD are presented additional techniques, such as Cyclic Stability (CS) and Float test (FT), that are related to the device characterization.

2.2.1 Cyclic Voltammetry

Cyclic Voltammetry (CV) is an electrochemical technique used to study the redox behavior which involves sweeping the potential applied to an electrode in a linear or triangular manner while measuring the resulting current. The speed of the potential change in mVs^{-1} is designated as the sweep rate or scan rate, ν, and the range of potential change is called the potential window or operating potential.

The instantaneous current during the anodic/cathodic (red/ox) sweeps is sampled to characterize the electrochemical reactions involved. The plot current (mA or A) versus potential (V) is typical for defining at a glance the charge storage mechanisms of the electrode, faradaic or non-faradaic, and usually it's referred to a three electrode configuration, since the most reliable[10].

The current that flows onto a capacitor equals the product of a constant, its capacitance C, and the rate of change of the voltage, in other word the scan rate ν:

$$I = C \cdot \frac{dV}{dt} \tag{2.1}$$

In an ideal capacitor, the capacitance is constant, so also the current is constant, and this behaviour in a CV is represented by a rectangular shape, as in Figure 2.4(a). But due to the non-ideal structure of the electrode, some contributions of resistance are present, which leads to a not perfectly rectangular shape, as presented by 2.4(b),(c) and (d). This equivalence is appreciable mostly when a EDLC is considered, since its mechanism is almost equal to the ideal capacitor one, where the charge is stored in the double-layer and no reactions are happening. In PC electrode this model can still be applied, as the EDLC contribution isn't negligible, but it isn't enough to explain which charge storage mechanism is prevalent by only seeing the CV shape[8].

In Figure 2.5 are showed three different real CV of three different electrodes. The subplot 2.5a presents the CV shape of a EDLC electrode, surrounded by a dash-line rectangle representing the ideal behaviour, in which one can notice the parasitic resistance effect; in addition, two peaks at the boundaries of the potential window are shown, indicating that the electrode is being overcharged, leading to parasitic side reactions, such as decomposition of the electrode material, the electrolyte, or a combination of both[11]. In Figure 2.5b the CV is typical to a pseudo-capacitance, where the vicarage EDLC shape shows two peaks related to the redox reaction; particularly, in transition metal oxide, these peaks are related to the shift into oxidation state. However, i.e. RuO_2 or MnO_2, the oxidation state shift can happen for little variation in the potential window, and this involves that multiple redox reactions occur simultaneously, so in the final CV these status changes aren't visible. This confirm the not complete reliability of information proceeds by only looking at the CV. A battery-like behaviour is presented in the plot 2.5c, mainly in one potential side, in which the contribution of charge storage is presented by the highest peak in current.

A way to define the electrode working principle is to examine the material's intrinsic charge storage kinetics. Using the Grahame-Stern model, the total charge storage can be define as the sum of the inner (diffusion-controlled) and outer (surface-controlled) charge surfaces contribution. The foundation of this idea is that the instant storage of charged species (ions) at the outer electrode surface is

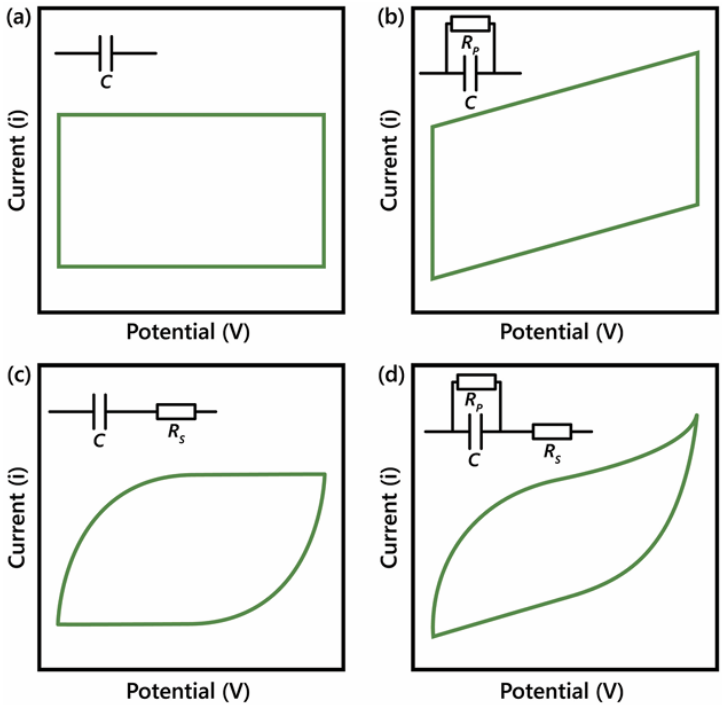

Figure 2.4: Equivalent circuits under Cyclic Voltammetry analysis[11]. C is the capacitive element, R_S and R_P are respectively the series and parallel resistances.

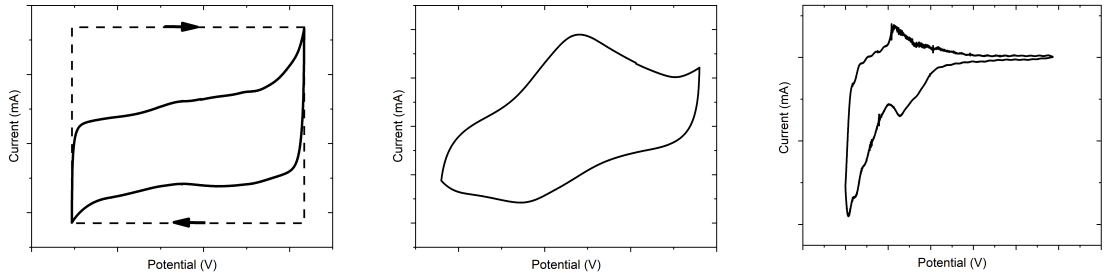

Figure 2.5: Cyclic voltammogram curves in example. In (a) an ideal rectangular dash-line shape, typical of capacitor, and a real EDLC CV, not perfectly rectangular with high polarization peaks. In (b) a Pseudo-capacitance behaviour, in which are recognised the two redox peaks among the EDLC shape. In (c) a faradaic CV, in which the peaks are predominant.

independent of the scanning rate (non diffusion-controlled), while charge storage at the inner surfaces is dependent on the potential rate[11]. Due to the correlation

between (inner) charge and scan rate in a CV, the relationship between response current (i) and the scan rate (ν) is given by the sum of the contributions from the surface-controlled and diffusion-controlled currents[12]:

$$i = i_{surface} + i_{diffusion} = a\nu^b \tag{2.2}$$

where a and b are adjustable parameters in the equation. A way to define these parameters is to set multiple CV with variable scan rate, following a logarithmic scale, since:

$$log(i) = log(a) + b \cdot log(\nu) \tag{2.3}$$

For b value equal or near 1, the current response will be linearly proportional to scan rate, characteristic of surface-controlled behavior, so EDLC type. When b is equal to 0.5, the dependency on scan rate is square root, meaning that at higher scan rate the current will grow slowly, a characteristic of diffusion-controlled processes, so battery-like. Defined the two boundaries, in the middle is preferable to say that the process are pseudo-capacitive, since the mechanisms of charge storage are a combination of the two ones, but it's not restrictive as a concept, but serves as a guideline for careful interpretation of the electrode nature.

All these evaluations are made considering fixed the potential window, however its width must be defined before this analysis, because small bias could not include all the redox reactions, leading to an inaccurate interpretation of the information. The ESW is the maximum polarization that can be applied to the electrode without encountering parasitic side reactions, i.e. decomposition of electrolyte, and overcharge status. In an safe and optimal potential window, the coulombic efficiency must be higher than 99%, so the charge lost during the charge/discharge step is negligible. In order to evaluate the operating potential, sequential CV at low scan rate (1 to 5 $mV \cdot s^{-1}$) are made in which the potential bias is increased in small variation (preferable 0.1 V) until the previous condition isn't meet anymore or some unwanted reactions happen. In a EDLC electrode, going further than the operating potential usually is represented by current peaks at the highest potential, meaning that the electrode starts to overcharge, leading to a complete degradation of it.

The evaluation of the capacitance from a CV is made by calculating the area under the CV shape, divided by the scan rate and the double of the operating potential window:

$$C = \frac{1}{\nu 2\Delta V} \int_{V_{min}}^{V_{max}} i(v)dv \tag{2.4}$$

where ν is the scan rate, ΔV is the operating potential window, V_{max} and V_{min} are the two boundaries of the window, and i(v) is the current related to the voltage.

Also, the evaluation can be made by taking the response current and evaluate its integral:

$$C = \frac{\int_0^t i(t)dt}{\Delta V} \tag{2.5}$$

where i(t) is the response current, assuming 0 s as the starting time.

When capacitance is used as comparison parameter, it's better if its value is expressed in relation with the active material mass or surface:

$$C_{a.m.} = \frac{C}{m} \tag{2.6}$$

$$C_s = \frac{C}{S} \tag{2.7}$$

where $C_{a.m.}$ is the specific capacitance per active material expressed in F/g, C_s is the surface capacitance expressed in F/cm^2, m is the active material mass and S is the surface area of the electrode.

Finally, from the CV are obtained the coulombic and energetic efficiencies, evaluated according to the following equations:

$$\eta_C = \frac{Q_D}{Q_C} \tag{2.8}$$

$$\eta_E = \frac{E_D}{E_C} \tag{2.9}$$

2.2.2 Galvanostatic Charge/Discharge

Galvanostatic Charge/Discharge (GCD), denoted also with the acronym CCCD (Constant Current Charge/Discharge), measurements are the most utilized methods to characterize the final supercapacitor devices in direct current. The test consists in repetitive charge and discharge cycles for the supercapacitor cell at a constant current or with different current rate, mainly expressed as current per active material, i.e. 0.1 A g^{-1} or 1 A g^{-1}, including or not a period between charge and discharge when the peak potential V remains constant (dwell time)[8]. The resulting response is a variation of potential V versus the charge/discharge time. While the CV analysis was the best for define the features of the single electrode, GCD tests are considered the most adaptable and reliable method to characterize the device itself.

In an ideal capacitor situation, the dependence of voltage on current follow the integral of the second one, but as it's constant in time, the voltage will be dependent linearly with time:

$$v(t) = \frac{1}{C} \cdot \int_0^t i(t)dt = \frac{I \cdot t}{C} \tag{2.10}$$

where I is the current applied, C the constant capacitance and t the test time.

The assumption of constant variation of voltage in time is reliable in an EDLC system, as the working principle follows the separation of charge, like in a capacitor, so the overall charge/discharge will be presented in a voltage-time plot by a triangular shape. In a real electrode there are parasitic resistance ESR, which leads

to a charge loss, so a decrease in efficiency, and in the same plot as before this leakage is represented by an offset in the charge/discharge steps, defined as *iR-drop*. In Figure 2.6 this situation is showed. From that it's possible to quantify the ESR by applying Ohm's law on it:

$$ESR = \frac{iR - drop}{i} \tag{2.11}$$

where iR-drop is the potential drop showed in the Figure and i is the applied current.

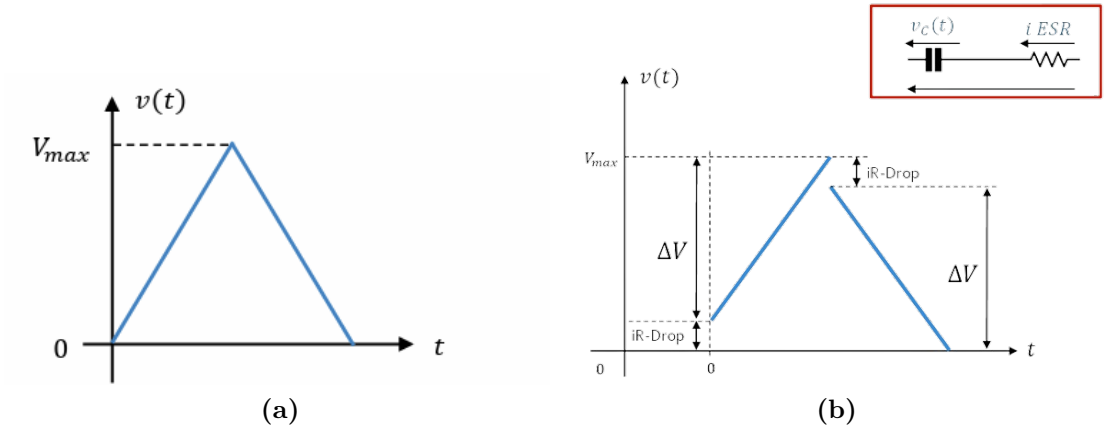

Figure 2.6: Galvanostatic Charge/Discharge curves in example, plotted as voltage VS time. In (a) an ideal triangular shape, typical of capacitor, with no resistance contribution. In (b) real shape of a charge/discharge step in a EDLC electrode, in which are noted the two iR-drop offset.

For pseudocapacitive electrode, charge-discharge profiles have non-linear variation due to (quasi) reversible redox, in which ion diffusion takes place, and it's dependent on the applied potential window, unlike the EDLC case where the potential window is related mainly to the safe zone (no overcharge). The selection of the potential limit in a pseudocapacitance system is crucial in the determination of the charge that pass on and through the surface. Case similar is for battery-like electrode, in which only faradic reactions happen, where almost all charge flowing occurs at a small fixed bias window. Figure 2.7 shows three different GCD curves, according to the type of active material.

The contribution of the applied current rate intensity must also be taken into account. For large current the time of charge and discharge is reduced, but the contribution of parasitic resistances becomes more evident, leading to an higher iR-drop, which will result in less charge stored on the surface and so a lower specific capacitance. Related on that, higher contribution of iR-drop can be associated to a

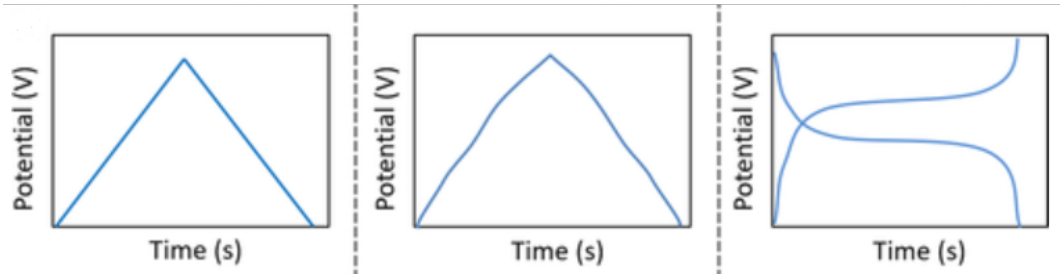

Figure 2.7: Different GCD according to the active material in question[13]. **Left**: Ideal EDLC. **Middle**: EDLC with pseudocapacitance contribution. **Right**: Battery-like.

overheating of the device, in which the electrolyte starts to degrade and the device will be destroyed. On the contrary, small current may enhance recoupling of ions and passages of charge between the electrode, with the result that self-discharge is favoured and leakage current is increasing[8].

2.2.3 Electrochemical Impedance Spectroscopy

Electrochemical Impedance Spectroscopy (EIS) is a measurement that is employed in the analysis of electrode impedance. It consist in applying a small amplitude AC signal (±5 mV on average) over a broad frequency range of 10 mHz to 1 MHz, superimposed on a steady-state potential which is the open-circuit potential of the cell, and analyze the response in frequency. Unlike CV and GCD tests, in which we can also evaluate resistance contribution but the electrochemical state is constantly disrupt due to their dynamic nature, EIS experiments are performed on systems that are in an equilibrium state[11], so the overall impedance is dependent only by the OCP.

EIS measurements are employed not only to evaluate the charge storage mechanisms and the redox reactions which occur at the interface between the electrode and the electrolyte, inside and outside, but also to determine parameters that limit the performance of the electrode materials, such as electrode conductivity, charge transfer properties, and ESR.

All the data are generally represented graphically in two different plot: Bode and Nyquist. In a Bode plot the equivalent circuit that define the supercapacitor behavior is described by the evolution of impedance module and phase angles among different frequencies. The Nyquist plot, the popular one, shows the imaginary and real parts of the supercapacitor impedance in one complex plane. An ideal capacitor, with a ESR in series, has the impedance that follow the equation:

$$Z(\omega) = R(\omega) - jX(\omega) = R - j\frac{1}{\omega C} \tag{2.12}$$

where ω is the angular frequency, R is the ESR value, and C is its capacitance, and it is obvious to note that the dependency on frequency is mainly related to the imaginary part, so in a Nyquist plot it can be represented by a straight line that for f $\to \infty$ matches with ESR, as it shows Figure 2.8

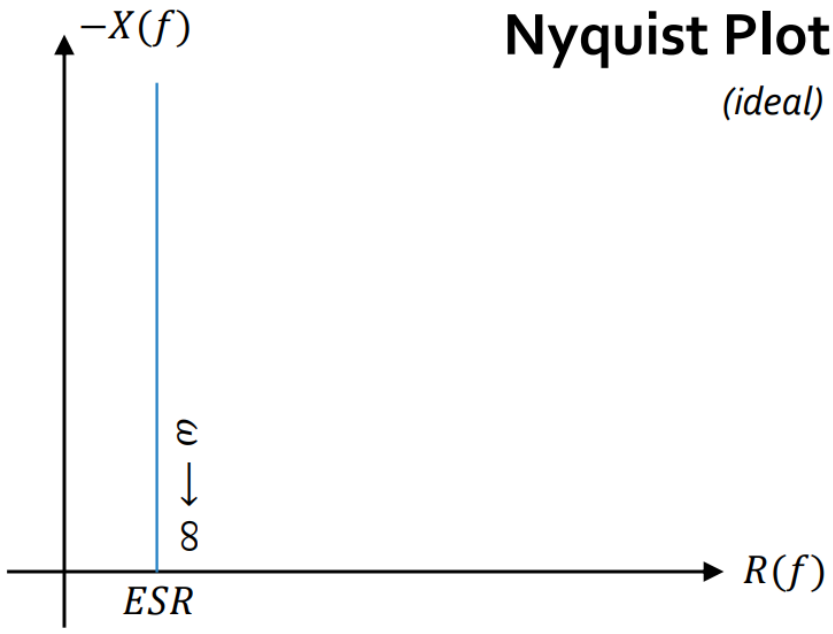

Figure 2.8: EIS of an ideal capacitor, without any contribution of resistance. The impedance graphically follows the equation 2.12.

As the equivalent circuit of an electrode, presented in Figure 2.1, is the sum of different contribution, including resistance in series/parallel, the real Nyquist plot differs from the ideal one, even if the capacitance behaviour is the same. An example of real Nyquist plot, accompanied by the corresponding Bode one, of an EDLC electrode is presented in Figure 2.9.

In the high-frequency region, a semicircle is usually observed (region between 10^4 and 10^5 Hz) that represents the resistance of the interface electrode-electrolyte. The intercept in the real axis corresponds to the electrode ESR. The diameter of the semicircle presents the charge transfer resistance, mainly a pseudo-capacitive effect related to the porous nature of the electrode. True EDLC super-capacitors should never show a semicircle in the high-frequency region[11], as this effect is related only for pseudo-capacitor material. A reason why in a EDLC we have a semicircle at high frequency can be related of impurities or dopants that contribute

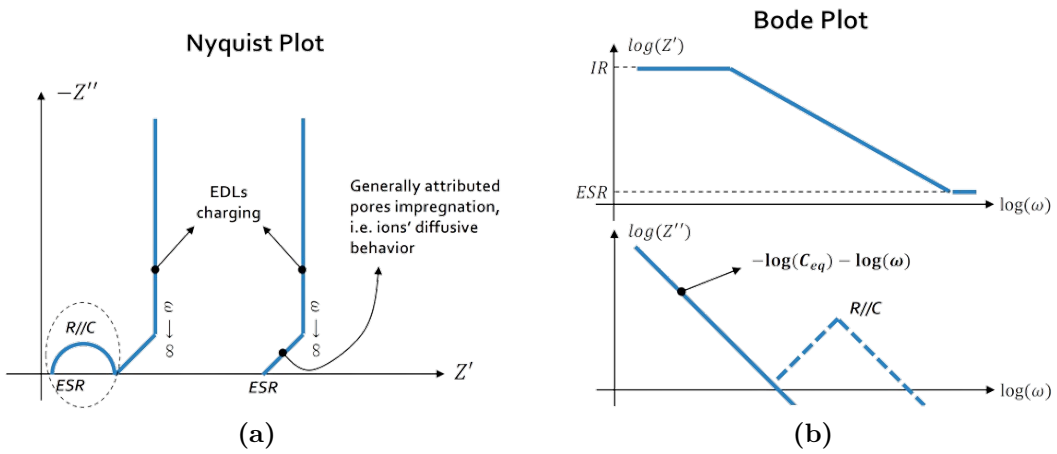

Figure 2.9: In (a) the response of shear stress w.r.t shear rate[14]. As the shear thinning effect becomes dominant in non-Newtonian liquid, the response in stress decreases. In (b) the response of viscosity w.r.t shear rate[14]. In a range of shear rate its magnitude start to decrease until it reaches a steady value.

in charge transfer events, but the most likely cause could be interfacial impedance occurring at the current collector/active material interface[11]. A 45° line after ESR is the one excepted, which is typical for porous electrodes and corresponds to the ion's diffusion mechanisms among Warburg diffusion[8], followed by a vertical line that is parallel, or close to parallel, to the imaginary impedance axis in the lower frequency region (lower than 1 Hz). The shorter is this 45° line, the faster the impedance starts to increase the imaginary part, the better the performance of the electrode. as evidence that all the reactive sites are fully accessible in a short time, leading to capacitor-like behavior[11].

The Bode plot (Figure 2.9b) demonstrates that at frequency near to zero the dominant parameters are the internal resistance (IR) and the EDLC formation, as expected, but the capacitance decreases in the high-frequency region, leading to a pure resistor behaviour. The latter indicates that the ions are unable to diffuse into the micro-pores of the electrode materials[8], making the formation of the double charge layer impossible. In other words, the impedance of SCs falls between the pure resistor (phase angle 0°) and a pure capacitor (phase angle 90 ∘). The dash line representing the pseudo-capacitance contribution is an indication that this factor increases the imaginary part of the impedance, as expected.

Different expected EIS according to the nature of charge storage of the electrode are presented in Figure 2.10.

The divergence from the parallel line is a matter of redox reaction at the electrode surface that give rise to pseudo-capacitance behavior, leading to additional resistance

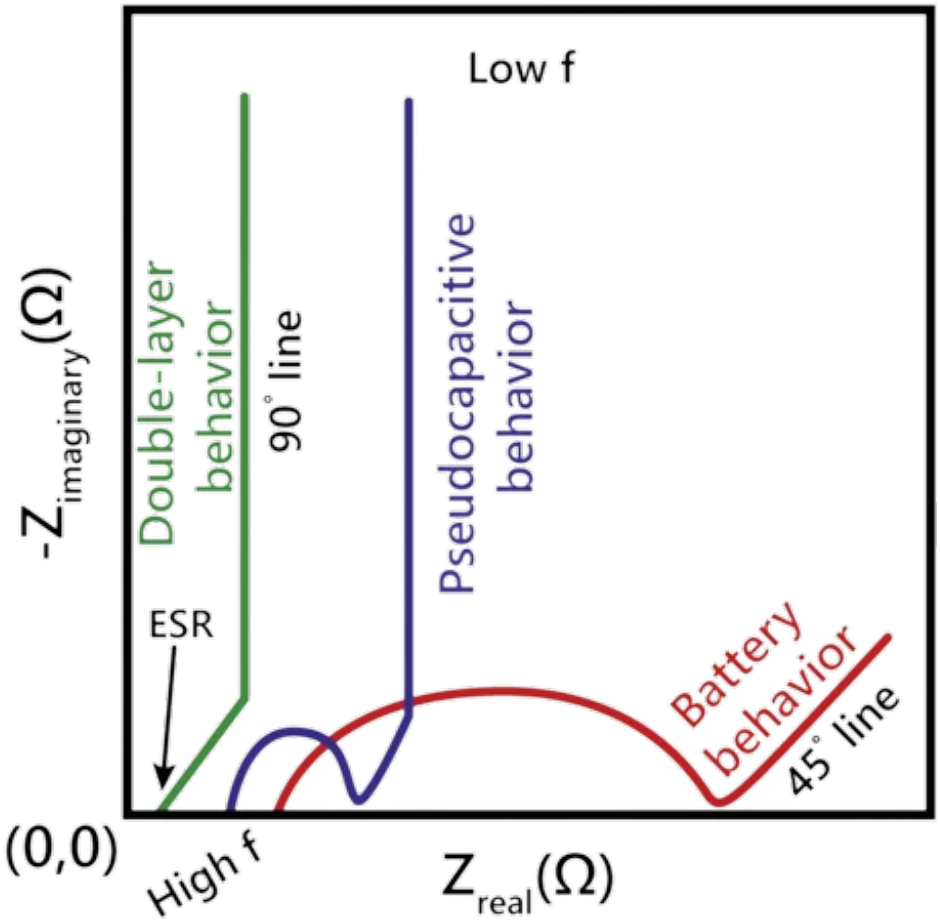

Figure 2.10: Typical Nyquist plot according to the nature of the electrode[11]. The pseudo-capacitive behaviour doesn't include internal Faradic reactions that happen in the low frequency range, which usually is represented by a tilted diffusion line.

contribution which are felt more at lower frequencies. In a battery-like system, the capacitance effect is nearly zero, as the major contribution of charge storage is due to faradic reactions, so the straight line is hardly noticeable.

Knowing how to interpret the Bode and Nyquist plots, it's possible to quantify the capacitance of the electrode. Taking the value of the imaginary part at the lowest frequency (approximately 10 mHz), its value can be obtained by the equation 2.13

$$C = -\frac{1}{2\pi f Im\{Z_C\}} \tag{2.13}$$

where f is the lowest frequency value and $Im\{Z_C\}$ is the imaginary part of the electrode impedance. Using equation 2.6 and/or 2.7 it's possible to derive the corresponding specific capacitance.

2.3 Rheology

Rheological characterization of electrode slurry is essential when a R2R coating is considered. For suspensions, the most important rheological property is the viscosity, a property that define the resistance of a fluid to deformation at a given rate, measured in Pascal per second ($Pa \cdot s$) or centipoise (cP). It directly influences the behavior of the slurry formulation and the uniformity of particle dispersion during mixing, production of electrode through coating and subsequent drying[6]. In general, a slurry is a non-Newtonian complex mixture of various sizes and shapes particles, polymeric binder and water or organic solvent. Other rheological properties concerning the slurry are viscoelasticity and yield stress, which correspond to the behavioural response when a force is applied.

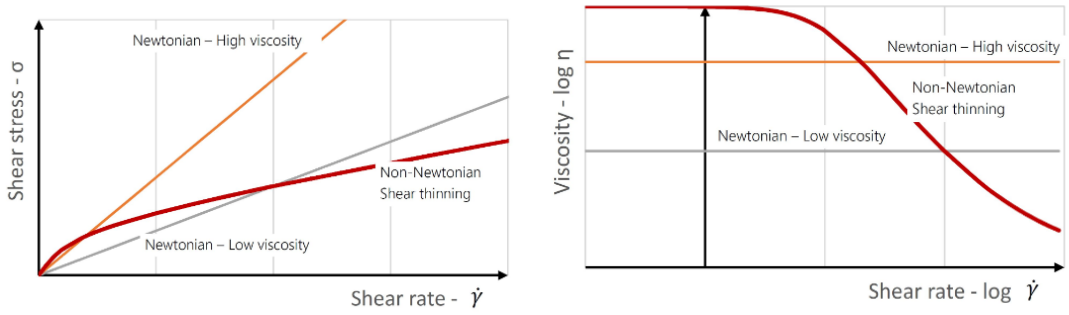

(a) **(b)**

Figure 2.11: In (a) the response of shear stress w.r.t shear rate[14]. As the shear thinning effect becomes dominant in non-Newtonian liquid, the response in stress decreases. In (b) the response of viscosity w.r.t shear rate[14]. In a range of shear rate its magnitude start to decrease until it reaches a steady value.

Usually, when a slurry is considered, due to its non-Newtonian behaviour, the viscosity is dependent on the Brownian and hydrodynamic forces, maximum solids packing fraction, particle charges, particle/particle and particle/polymer interactions, which lead to exhibit a shear-thinning behavior where the shear-viscosity reduces with increasing shear rate[6]. At higher shear rates, the network

particle structure tends to destroy, forcing them to realign themselves in a more orderly structure parallel to the strong shear field, causing the viscosity to decrease and reach a Newtonian plateau at high shear rates. These effects are illustrated graphically in shear stress and viscosity versus shear rate plots, respectively Figure 2.11a and 2.11b, which are compared with Newtonian cases. Another factor that is crucial in a coating process with this kind of slurries is the relax time, a parameter that define the time required to the fluid to achieve again the same internal structure after a high stress perturbation. In a R2R system, the instability of flow between two counter-rotating rolls may leads to a coated film non-uniform, which can have a quasi-sinusoidal profile[15], so a short relax time can provide a self-correction before the complete drying.

In accelerated/decelerated flows, viscoelasticity comes into play. Rheological measurements are normally carried out under oscillatory shear mode where the storage and loss moduli, G' and G'', are reported in function of angular frequency.

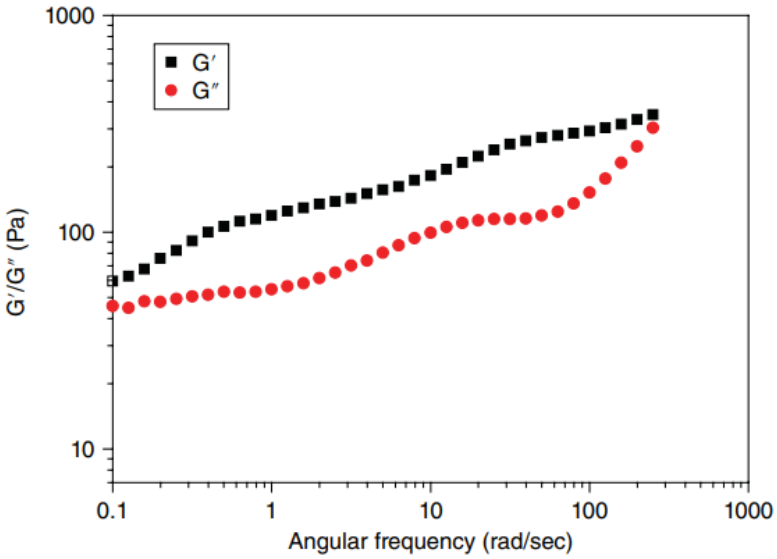

Figure 2.12: Example of storage/loss moduli graph VS angular frequency[6]. In this case, in the range between 0.1 and 200 rad/s the storage modulus is higher than the loss one, suggesting a fluid that is acting as a elastic solid. No additional information are provided outside that range.

In Figure 2.12 these two parameters are in comparison with each other and this suggests the response of the fluid at the stress perturbation. According to literature[6], when the storage modulus is greater than the loss one ($G' > G''$) the internal structure of molecules is intact and the slurry behaves like an elastic solid, while, on the contrary ($G'' > G'$), when the force applied is enough to destroy this

orientation and a realignment of the molecules with respect to strain stress takes place, the slurry behaves like a viscous liquid. The transition between the two states, i.e. $G' = G''$, is defined by the yield stress. This property must be taken into account during electrode manufacturing, as it can influence its structure. During mixing, this point must be overcome in order to provide a better homogeneous blending of particles, while in the drying step the stress that is subjected the electrode surface can increase, since the solvent evaporates and the solid content fraction increases, providing an higher yield stress.

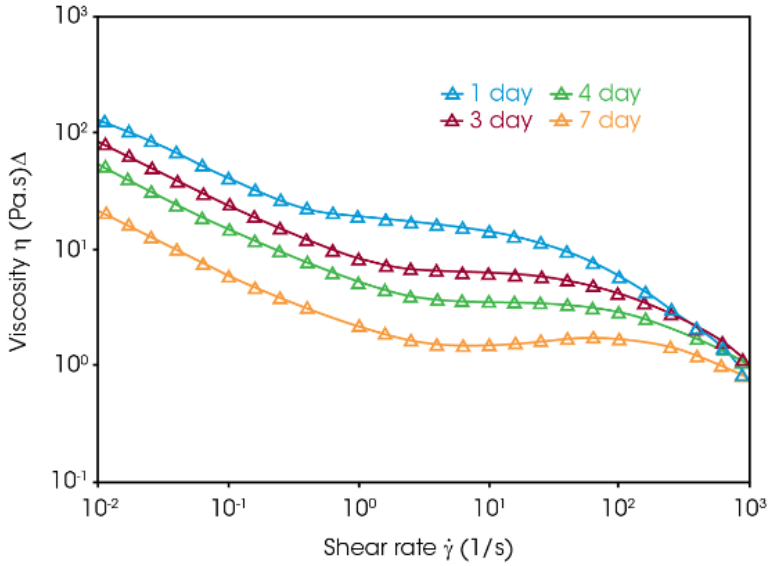

Figure 2.13: Viscosity VS shear rate of the same slurry in different time after the mixing step[16].

Other external aspects that can affect the rheology of slurries are temperature and time. Increasing the temperature, particles have higher energy, so they oscillate more frequently and can destroy internal bonds, so as a consequence of that the viscosity can decrease at lower shear rate, changing its behaviour during the coating. Attention must be paid to not overheat the fluid, as it can lead to solvent evaporation, so a increase of solid content fraction, which cause the opposite of the case before. As in common slurries a binder component is present, which are the main causes of increased viscosity, some of them can degrade into the solvent after long time, causing a decrease in viscosity. This topic was investigated[16] by analyzing the same slurries with a binder component in different times after the mixing step, confirming a degradation of it and a reduction in viscosity of one order of magnitude just after one week.

2.4 Calendering process

Calendering, in the context of electrode manufacturing for supercapacitors, is utilized to thinner the electrode and conform its structure with controlled porosity and density, which are crucial for optimizing electrochemical performance. Since materials that define the electrode aren't of metallic origin, the equations don't follow the principle of metal calendering, but instead they include the springback (SB) effect[7], known as fast elastic recovery. When a load is applied to the surface, or the electrode passes through two rolls with a fixed gap, the final thickness won't be the expected one, since the internal structure has elastic properties that allow it to regain the same thickness before or almost.

The current collector foil of the electrode can be considered incompressible[7]. It's an approximation since metal can decrease its thickness with an external force, but due to its low thickness in comparison with the electrode one and also SB effect of metal (aluminum or copper), the approximation is valid. The scheme of the two rolls calendering is showed in Figure 2.14, in which are defined all the involved parameters.

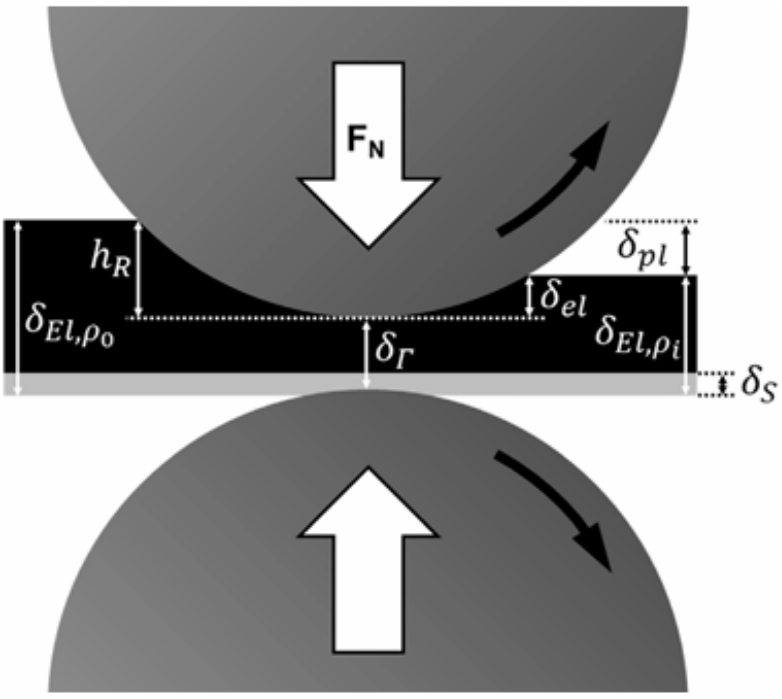

Figure 2.14: Schematic view of the two rolls calendering process[7].

From this scheme we define parameters as:

- δ_{EL,ρ_o}: thickness of the electrode, before the calendering step;
- δ_{EL,ρ_i}: thickness of the electrode, after the calendering step;
- δ_Γ: gap between rolls;
- δ_{el}: elastic coating deformation;
- δ_{pl}: plastic coating deformation;
- h_R: depth of roll penetration.

Plastic deformation is related on how much the coating is susceptible to external force, while the elastic one defines the effect of SB. A better way to define these values is the normalized one w.r.t the max depth of roll penetration[7]:

$$\delta_{el,n} = \frac{\delta_{el}}{h_R} \qquad (2.14) \qquad\qquad \delta_{pl,n} = \frac{\delta_{pl}}{h_R} \qquad (2.15)$$

The springback effect is evaluated as:

$$SB = \frac{\delta_{EL,\rho_i} - \delta_\Gamma}{\delta_\Gamma} \qquad (2.16)$$

From these parameters it's possible to evaluate the topology of response of the electrode to an external force, in this case compression. Despite the variation of thickness provide us preliminary information about porosity and how much the substrate is wettable to electrolyte, it doesn't give further details about the interface between electrode and current collector. As explained in Section 2.2.3, the poor contact between them is defined by a semicircle in the Nyquist plot at high frequency, a parasitic contribution that decrease the performance of the electrode. Compression through calendering can lead to an improvement of the contact at the interface aluminum/carbon electrode or to a better internal particle particle contact[9], removing defects that affect its conductibility.

2.5 Field Emission Scanning Electron Microscopy

Field Emission Scanning Electron Microscopy (FESEM) is an advanced microscopy technique used for high-resolution imaging of surfaces. This method allows to examine the morphology, topography, and composition of various materials at nanoscale levels.

Through a focused electron beam, the images of the surface is obtained by the signal response, which include secondary electrons, useful for imaging surface topography, back-scattered electrons, which provide information about atomic composition and density variations in the sample, and characteristic X-rays. The emitted electrons are accelerated and focused by a series of electromagnetic lenses, which improve the electron beam shape maintaining its coherence. To prevent charging effects during imaging, the sample may need to be involves in coating with a thin layer of conductive material, such as gold or carbon.

The FESEM has a large depth of field, around the range 4 mm - 0.4μm, with a magnification of 10X - 3000000X and a nanoscale resolution (1 - 10 nm), which allows a large amount of the sample to be in focus at one time and produces a sort of 3D imaging. In Figure 2.15 a schematic of it is presented.

2.6 Energy Dispersive X-ray Spectroscopy

Energy Dispersive X-ray Spectroscopy (EDX), also known as Energy Dispersive X-ray Analysis (EDXA) or Energy Dispersive X-ray Fluorescence (EDXRF), is an analytical technique used for elemental analysis of materials, which operates in conjunction with scanning electron microscopes (SEM), providing information about the elemental composition of a sample.

The process begins with the bombardment of the sample by a focused electron beam generated by the SEM. When the high-energy electrons interact with the atoms in the sample, they can dislodge inner shell electrons from the atoms in the sample. When inner shell electrons are ejected, outer shell electrons drop down to fill the vacancy, releasing energy in the form of characteristic X-rays. Each element emits X-rays at specific energies unique to that element. The characteristic X-rays emitted by the sample are detected by an energy-dispersive X-ray detector positioned near the sample. This detector is typically a silicon semiconductor detector with a solid-state crystal structure. As the X-rays strike the detector, they produce electrical signals proportional to their energies. These signals are then processed to generate an energy spectrum. The spectrum displays peaks corresponding to the energies of the detected X-rays, with each peak representing a specific element present in the sample.

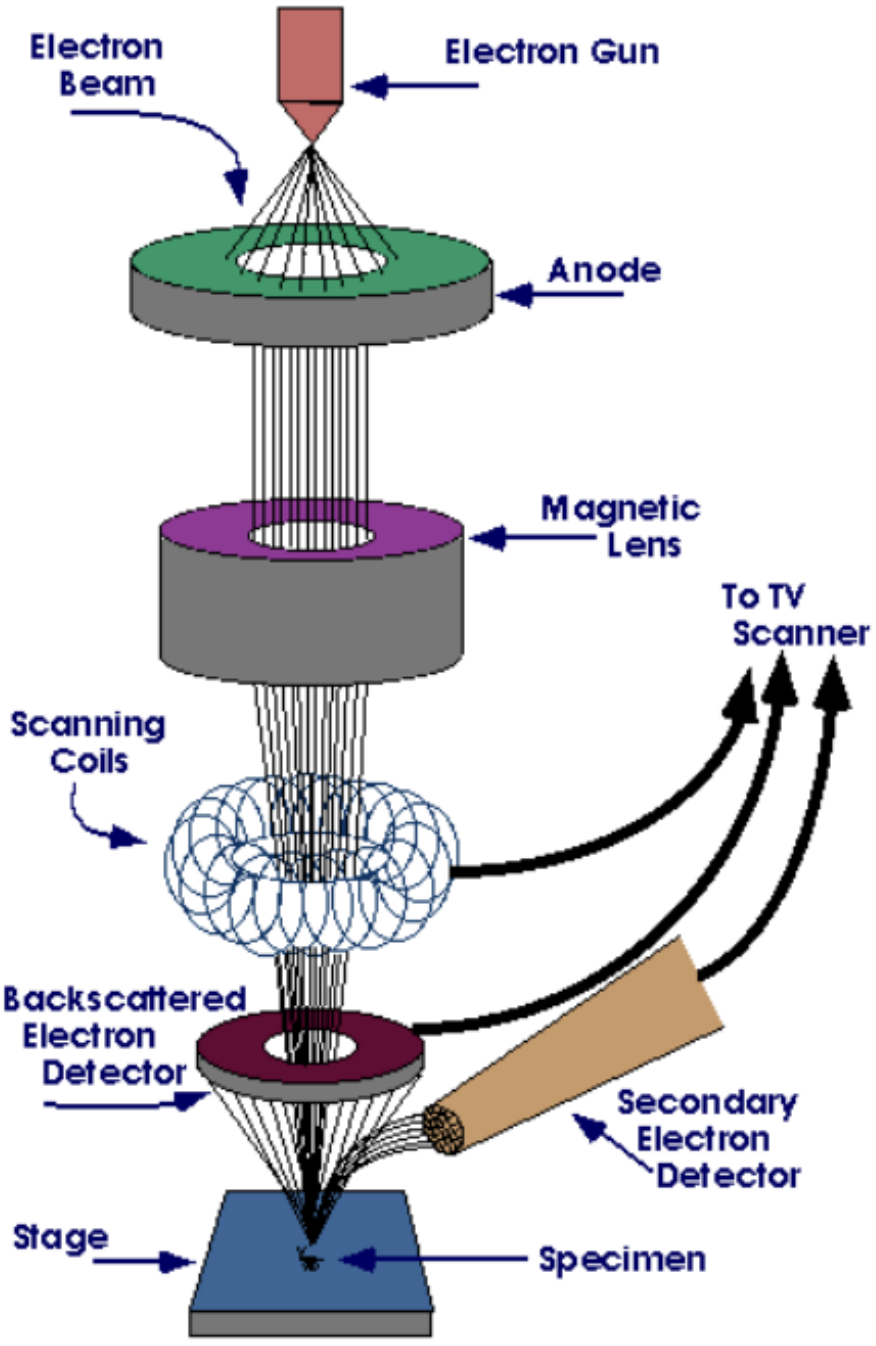

Figure 2.15: A schematic of FESEM[17].

2.7 Raman spectroscopy

Raman spectroscopy is an analytical technique used to study vibrational, rotational, and other low-frequency modes in a system. It provides detailed information about the chemical composition, molecular structure, and physical properties of materials.

Raman spectroscopy involves the scattering of light. A laser beam, typically in the visible or near-infrared range whose wavelength match the energy levels of the vibrational modes of interest, is directed onto a sample. When the laser light interacts, most of it is elastically scattered, meaning the photons retain their original energy and wavelength. However, a small fraction of the incident light undergoes inelastic scattering, known as Raman scattering. The incident photons interact with the molecules in the sample, causing them to undergo energy changes. These energy changes correspond to the vibrational and rotational modes of the molecules. The scattered photons emerge from the sample with different energies, either higher or lower than the incident photons, depending on the energy exchanged during the interaction. The scattered light is collected and analyzed using a spectrometer. The Raman spectrum is generated by plotting the intensity of scattered light as a function of the energy difference (wavenumber) between the incident and scattered photons. The spectrum consists of peaks at specific wavenumbers corresponding to the vibrational modes of the molecules in the sample.

Raman spectroscopy offers several advantages, including non-destructive analysis, minimal sample preparation requirements, and the ability to analyze samples in various physical states (solid, liquid, gas). It is used in a wide range of applications, including identification of unknown substances, characterization of polymers and biomolecules, analysis of pharmaceuticals, investigation of cultural heritage artifacts, and monitoring of chemical reactions.

2.8 X-ray Photoelectron Spectroscopy

X-ray Photoelectron Spectroscopy (XPS), also known as Electron Spectroscopy for Chemical Analysis (ESCA), is an analytical technique used to determine the elemental composition, chemical bonding, and electronic state of elements within a material.

XPS involves irradiating a sample with a focused beam of X-rays. The energy of the X-rays must be higher than the binding energies of the electrons in the sample's atoms. Typically, monochromatic X-rays generated from a suitable X-ray source, such as a magnesium or aluminum anode, are used for excitation. When the X-rays interact with the atoms in the sample, they can eject inner-shell electrons through the photoelectric effect. The probability of electron ejection depends on the binding energy of the electrons and the energy of the incident X-rays. Electrons

from different atomic orbitals (e.g., 1s, 2s, 2p) may be ejected depending on the energy of the X-rays. The ejected photoelectrons have energies characteristic of the binding energies of the electrons in the atomic orbitals from which they were ejected. These photoelectrons are emitted from the sample surface and carry information about the elemental composition and chemical environment of the atoms they originated from. The emitted photoelectrons are collected and energy-analyzed using a hemispherical analyzer or similar device. The analyzer measures the kinetic energy of the photoelectrons, which is proportional to their binding energy within the material. Figure 2.16 shows a schematic of a XPS.

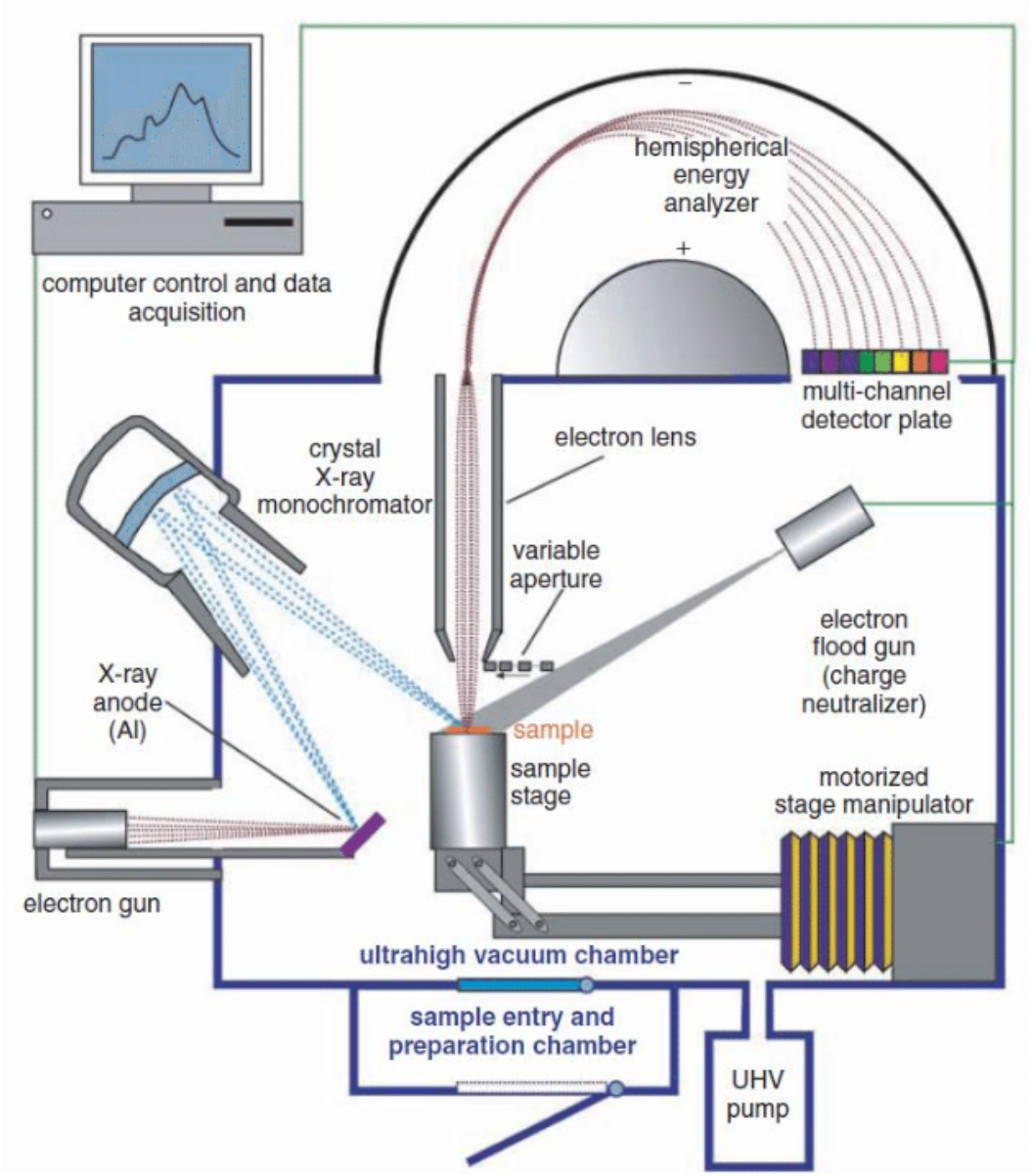

Figure 2.16: A schematic of XPS[18].

Chapter 3

Material and methods

3.1 Electrode fabrication

3.1.1 Slurry preparation

Three different active materials were investigated in slurry preparation: activated carbon, MnO_2 and carbon black. The recipe used as reference is the one made with AC Kuraray® YP-50F as active material, combined with carbon black Timical SUPER C65 from MTI® corporation as conductive agent, sodium carboxymethyl cellulose (CMC) and styrene-butadiene rubber (SBR), both from MTI® corporation, as binder, all in solvent of deionized (DI) water. The mass ratio of AC:CB:binder used was 85:10:5, where the binder CMC:SBR were in proportion 1:1. The volume of DI water was 3.7 mL per 1 gram of solid content (3.7 mL/g). All the component were mixed using a digital magnetic and hot plate stirrer (VWR® VMS Advanced). The mixing step consisted of pre-heat much of DI water taken (85-88 % from the total) at 70°C, then add the CMC power and mix at 70°C for 1 hour or until complete absorption, after add the C65 power and continue to mix for another 1 hour always at 70°C, after which add the AC in several parts (3 to 5) when the previous one was completely mixed, and continue to mix for another half hour at 70°C, followed by other 2 hours of mix but at room temperature (20 - 25°C), and finally add SBR diluted with the remaining DI water and mix for half hour.

In this thesis the activated carbon under investigation was Kuraray® YP-80F, which in comparison with YP-50F it presents an higher surface area (1692 m^2/g for YP-50F, 2271 m^2/g for YP-80F), so theoretically it can have an higher specific capacitance. The recipe for AC-based electrode was the same as the reference, except for the mass ratio, which in this case was 85:9:6 with binder content CMC:SBR ratio of 1:2, and for the volume per solid content, in which was selected 4.3 mL/g as the best choice. The reason of the mass ratio change was due to the fact that CMC tends to generate cracks after the drying phase, while SBR

possesses higher flexibility, stronger binding force, and higher heat resistance[19], and increasing its content may improve the structure of the final electrode avoiding internal ruptures. During the slurry preparation, it was noted that the solvent volume requested in order to have an homogeneous slurry was higher, perhaps due to a correlation with the higher surface area of this AC.

The procedure for the slurry based on MnO_2 was the same as the reference one. In that case, the mass ratio of MnO_2:CB:binder selected was 80:15:5, with the binder ratio of 1:1. The volume per solid content chosen was 3.9 mL/g. In this case increasing the SBR content was unnecessary, as the electrode structure was stable enough during the drying step.

For the case of battery-like electrode, carbon black (CB) was the active material. In proportion to the binder CMC/SBR, the mass ratio selected was 90:10, where the latter ratio was 1:1. The volume per solid content chosen was 19 mL/g. Increasing the SBR fraction turned out to be counterproductive, since the main consequence was an increase of the contact angle of the slurry which didn't allow adhesion between the latter and the current collector foil.

3.1.2 Electrode coating and cutting

The coating process made in laboratory was made by preparing a aluminum foil into a clean and flat glass surface. The surfaces have been cleaned with acetone, where the latter was also used as a means of adhesion between glass and aluminium foil. The slurry has been spread on the tip of the sheet with a silicone spatula. The coating step has been performed with a DrBlade® coater with adjustable gap between surface and blade. The gap has been regulated in order to include the thickness of the aluminum foil (15 μm). The coating speed wasn't recorded, as it was made manually. After the coating, the electrode was left to dry for 1 hour at room temperature (20-23°C). The thickness was measured using a thickness gauge with a resolution of 1 μm. The final electrode sheet was cut using MTI® corporation compact and precision pneumatic die cutter MSK-180S. The cutting dies used were the 8x 12mm diameter circles, used for the electrochemical characterization of the electrode, and the 8x 15mm diameter circles, used for the small device assembly (coin cell) and characterization.

The R2R coating was performed with MTI® corporation automatic roll to roll electrode coating system MSK-AFA-EI300. It is integrated with the functions of metallic foil roll unreeling, slurry feeder, coating blade, baking oven, and final electrode reeling together with touch screen operation for customer's utmost convenience. It provides also automatic alignment and the function of back and front coating synchronization through optical fibre. The type of coating is the reverse comma system, in which the slurry is spread into a coating roller, with a thickness controlled by a comma blade, and transferred completely into the current collector

foil hold by guide rollers. The gap between the coating roller and the one with the current collector was about 20 ± 1 μm. The gap of the comma blade was selected for the desired thickness of coating, without additional thickness of the current collector. The room temperature was kept between 20 and 25°C. The coating speed was 300 mm/min. The coating design was an alternating between 60 mm x 220 mm of coating area and 20 mm x 220 mm of no-coating zone. The integrated oven was set to a temperature of 80°C, in order to provide completely dry electrode at the end of the coating stepl. The thickness of it was measured using a thickness gauge with a resolution of 1 μm. From the coated roll, electrode strips were obtained with a little area of non-coated aluminum in the margins, and then electrodes for pouch cell were obtained by cutting these strips using MTI® corporation compact and precision pneumatic die cutter MSK-180S with die of 56mm (length) x 43mm (width), with a 9 mm (length) x 10mm (width) protrusion for contact welding.

3.1.3 Counter electrode preparation

Not correlated to the slurry topic but extremely necessary for the electrochemical investigation of the electrodes is the counter electrode formulation. The CE requested must not polarise itself during measurement, in order to not tampering the electrode characterization, so it should have an high superficial area. In this case it was made with Kuraray® YP-50F as active material but with a different formulation from the usual slurry investigated before. The counter electrodes, denoted in this thesis also with the pseudonym of Oversized Carbon Electrode (OCE), were made by a total of 3 grams of AC Kuraray® YP-50F (85% - 2.55 g), carbon black Timical SUPER C65 from MTI® corporation (10% - 0.30 g), and polytetrafluoroethylene PTFE (5% - 0.15 g). All the components were mixed in 60 mL of ethanol at 60°C for 3 hours, until the solvent was completely evaporated and the mixture has taken on a malleable solid consistency. This compound has been folded in on itself until it became firmer and less wet, then it has been thinned using a kitchen dough sheeter at a thickness of 400 μm and cutted with a 12 mm diameter hole punch. At the end the 12mm disc of CE have been dried first in oven at 60°C for at least 1 hour and then at 120°C in vacuum for 4 hours. The finals BFE had a thickness of 0.8 - 1.1 mm and a mass from 30 to 45 mg.

3.2 MnO_2 synthesis

The synthesis of MnO_2 has been made by combining $MnSO_4 \cdot H_2O$ and $KMnO_4$ in water solution. The chemical reaction follows the equation 3.1[20]:

$$2\,KMnO_4 + 3\,MnSO_4 + 2\,H_2O \longrightarrow 5\,MnO_2 + K_2SO_4 + 2\,H_2SO_4 \qquad (3.1)$$

Two solution of 0.05 M has been prepared for the reaction; 1.58034 g of $KMnO_4$ was diluted in 200 mL of DI water, whose solution took on a purple colouring, and 2.5353 g of $MnSO_4$ in 300 mL, in which the solution became transparent after complete dissolution. The two solution were stirred together at 35-40°C for at least 1 hour, in which a brown colouring began to appear, meaning that the precipitated MnO_2 was formed. The application of a slightly heat improve the reaction and partially prevents adhesion to side surfaces of the becker. The overall solution was filtered with a vacuum flask using as filter Whatman® glass microfiber filters, binder free, Grade GF/C. After complete filtration, the powder was cleaned with DI water rinses until the wastewater was clean and clear. The required volume of water was evaluated in order to reproduce the synthesis in successive stages. The rinsing operation was repeated successively until the conductivity of the waste water was less than 4-5 $\mu S \cdot cm$. The cleaned MnO_2 has been dried firstly in oven at 60°C for 24 hours, in order to separate the powder from the filter, and then dried at 80°C in vacuum for 2 hours and finally dried at 200°C in air for 2 hours.

3.3 Rheology investigation

Rheology investigation of slurries was performed with Anton Paar® MCR 302 SN81180769. Three different measurements were made: viscosity dependence on shear rate and temperature variation, relaxation time after high shear rate and oscillatory shear mode. The investigated slurry was spread between two plates of 20 mm of diameter with a gap of 200 μm until complete coverage without spills on the sides. The slurry has been brought up to temperature before each test at five different temperature, i.e. 15, 20, 25, 30 and 35°C. The shear rate dependency was performed in the range between 0.1 and 1000 s^{-1}, with logarithmic incremental step. Immediately after this measure, the shear rate has been fixed to 0.5 s^{-1} and kept in this condition for 200 s, so as to measure the relaxation time. The oscillatory shear mode has been performed at a fixed temperature of 25°C, changing the angular speed from 0.1 to 1000 rad/s, and extrapolating the storage and loss moduli. The plate was cleaned with acetone before and after each measurement.

3.4 Calendering investigation

Calendering step has been made with MTI® corporation MSK-HRP-01. The user can operate with it by changing the temperature of the two rollers, the rolling speed and the gap between them, using two analog dial gauge. Calendering was performed with rolls at a temperature of 40°C, speed roll of 6 mm/s and a gap set to 60 - 90 % of the initial thickness (electrode + current collector foil). The

process was repeated 20 times, alternating forward and backward rolls direction. The thickness was measured using a thickness gauge with a resolution of 1 μm.

3.5 FESEM investigation

Electron microscopy characterization was carried out on MnO_2 electrode with a Field-Emission Scanning Electron Microscope (FESEM Supra 40, manufactured by Zeiss). Measurements were carried out on the surfaces. PANalytical X'Pert MRD Pro powder diffractometer equipped using the 1D PIXcel detector has been used for the X-ray diffraction analysis (Malvern PANalytical, the United Kingdom). The diffractograms were collected in Bragg-Brentano reflection mode by using a Cu Kα1/2 radiation, at an operating voltage of 40 kV and a tube current of 40 mA. The instrumental broadening was computed by Caglioti-equation based on the reflections of a standard LaB6 powder NIST660a. The measurements were carried out in continuous mode with a step size of 2 $\theta = 0.0131°$ and a data time per step of 1500 s. QualX equipped with COD database was employed for the qualitative phase determination and MAUD-free software for the quantitative analysis and refinement. Micro-Raman spectroscopy was performed by using a Renishaw InVia Qontor Raman microscope. A laser diode source (λ=532 nm) was used with 5 mW power, and sample inspection occurred through a microscope objective (50X), with a backscattering light collection setup. The Raman spectrum analysis was carried out with Fityk software. Lorentzian functions were used as fitting functions. All the data are reported with baseline correction.

3.6 XPS investigation

XPS measurements were carried out by means of a PHI 5000 Versaprobe spectrometer (Physical Electronics, USA), equipped with a monochromatic Al k-alpha source (1486.6 eV), together with a dual beam neutralizer system, composed by an electron beam and an Ar ion source, used to compensate surface charging phenomena. Survey and High-Resolution (HR) scans have been exploited to get information related to surface relative chemical composition and element oxidation states. Data analysis has been performed thanks to Multipak 9.7 version dedicated software, provided by PHI.

3.7 Electrochemical investigation

Electrochemical measurements were performed in a S4R® PFA Swagelok-type cells 1/2" (Figure 3.1), in which the Working Electrode (WE) was the electrode

under investigation, the Counter Electrode (CE) was the active carbon-base BFE, and the reference was Ag pseudo. All the parts of the cell were cleaned before each measurements with ethanol, for removing residual electrolyte, cleaned in DI water with ultrasonic sonicator for 30 minutes and dried in oven at 60°C for 1 hour. The cell was assembled into a Glove Box, filled with nitrogen with internal contamination of H_2O (1.5 - 2.5 ppm) and O_2 (20 - 50 ppm). The separator used for the measurements was Whatman® glass microfiber filters, binder free, Grade GF/D, with a thickness of 675 μm and diameter of 12mm, previously heated at 120°C for at least 4 hours before putting it in the glove box. The volume used to soak the separator was 400 μL. The electrolytes used used had the same salt, in this case KPF_6, but a different solvent according to the type of electrode. The considered electrolytes were 1 M KPF_6 in PC (Propylene Carbonate) and 0.8 M KPF_6 in EC:DEC 1:1 (Ethylene Carbonate and Diethyl Carbonate in volume ratio 1:1). All the electrochemical characterization were performed by BioLogic® VMP3 Multichannel Potentiostat.

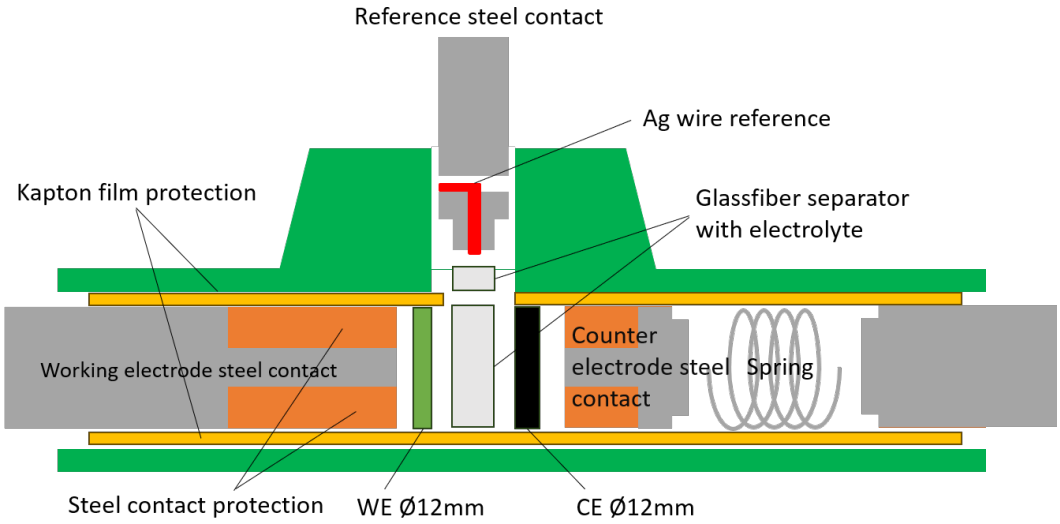

Figure 3.1: Example of assembled Swagelok-type cells for electrochemical investigation of working electrode.

3.8 Device investigation

Devices were assembled in coin cell 2016 inside a Glove Box filled with nitrogen following the schematic illustrated in Figure 3.2a. The choice of a smaller case is due to the small thickness of electrodes and separator. The coin cell was crimped using MTI® MSK-160E Digital Pressure Controlled Electric Crimper for CR20XX

Coin Cells. For the bigger device, mono-layer pouch cells were assembled inside a Glove Box filled with argon with internal contamination of H_2O (< 0.5 ppm) and O_2 (10 - 13 ppm). The choice of a mono-layer was due to the lack of large quantities of the separator. The device was packed into a self-made package made with plastic-coated aluminium. Contacts of the electrodes were welded with aluminum/nickel extension, according to the current collector in consideration, with the machine MTI® MSK-800W Desk-Top 800W Ultrasonic Metal Welder with Touch Screen Digital Controller. Final package was sealed inside the Golve Box with the machine MTI® MSK-115A-S Compact Vacuum Sealer with Integrated Sealing Temperature and Pressure Control. The devices were firstly investigated and activated with BioLogic® VMP3 Multichannel Potentiostat, and finally were investigated using Arbin Instruments® BT2000.

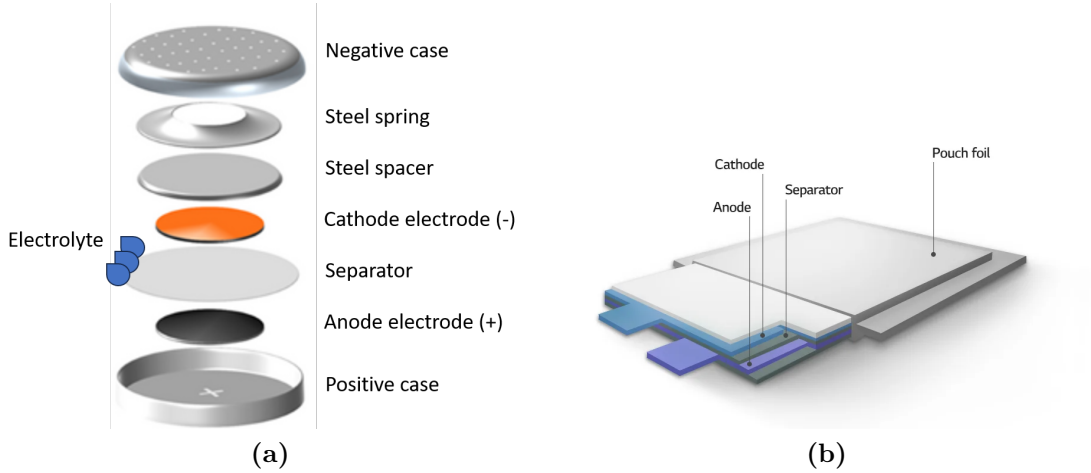

Figure 3.2: Example of assembled device for electrochemical test. *a*: coin cell. *b*: pouch cell.

Chapter 4

Rheology

4.1 Reference slurry

As a landmark, rheology investigation of the reference slurry made with AC YP-50F was made. Taking its results, it's possible to define which is the expected behaviour useful in the R2R coating. The critical issue found with preliminary tests was temperature, as it can change drastically the mixing procedure, so as the final viscosity, thereby coating quality. Figure 4.1 shows the results of the investigation.

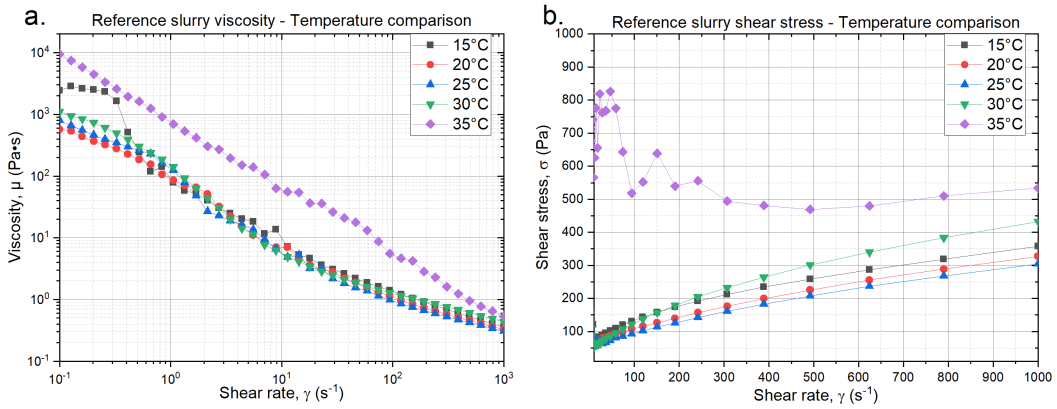

Figure 4.1: Reference slurry made with AC YP50F tested in different temperature values. In order: (a) variation of viscosity w.r.t. shear rate; (b) variation of shear stress w.r.t. shear rate. It's comparable to the expected non-Newtonian behaviour. The @35°C case is not comparable with the others, since the slurry paste seems to have dried during measurement.

As expected by theory and literature[14], the fluid acts as like a non-Newtonian liquid, since there's a decrease in viscosity in shear rate, meaning that the internal

particles orientation is changed in order to follow the imposed one. Also the logarithmic increase of the shear stress it's the one expected. A particular discussion of the temperature variations must be done, since the hoped behaviour was a decrease in viscosity, so in shear stress, with an increase in temperature. This condition has been confirmed with the three temperature, @15°C, @20°C and @25°C, however at @30°C it's noted a reversal of direction, as viscosity and shear stress as slightly higher than the @25°C case. A cause of this could be the drying process of the slurry paste during the measurement, in which the solvent content is reduced and the internal structure changed. This assumption is confirmed with the @35°C, as the viscosity is one order of magnitude higher than the others and the stress is far away of the non-Newtonian characteristic. A factor that must be highlighted is the tendency of reaching a boundary level at higher shear rate, even at different temperature, meaning that with higher applied force the slurry behave almost the same in different condition. From that results the optimal range for R2R can be between 15°C and 30°C, with greater care in the two boundaries, and the order of magnitude for viscosity is between 10^3 and 10^4.

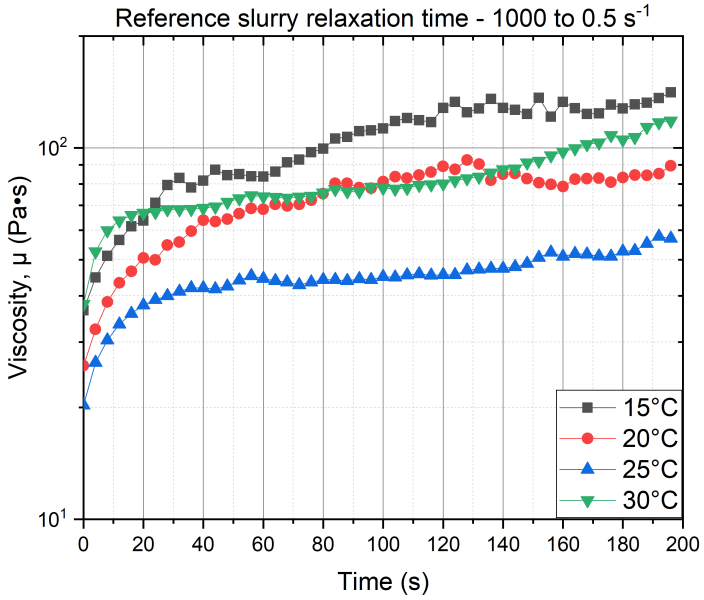

Figure 4.2: Relaxation time of viscosity from shear rate 1000 s^{-1} to 0.5 s^{-1}.

In addition, time relaxation of slurry viscosity is reported in Figure 4.2. For the first tens of seconds, the viscosity significantly increases near to a stable value until it reaches a more slight linear increment. It can be assumed that the time relaxation follows a logarithmic scale. From that plot, an initial information that

can be extract is the decrease of time relaxation with higher temperature, as the values, found approximately looking at the plots, in which the plot decreases its growth are 80, 40, 30 and 20 seconds respectively. High temperature means also particles with high energy, so reorganisation of internal structure occurs in less time. The @35°C case isn't reported, since it can't be correlated with the others cases, due to a too fast drying.

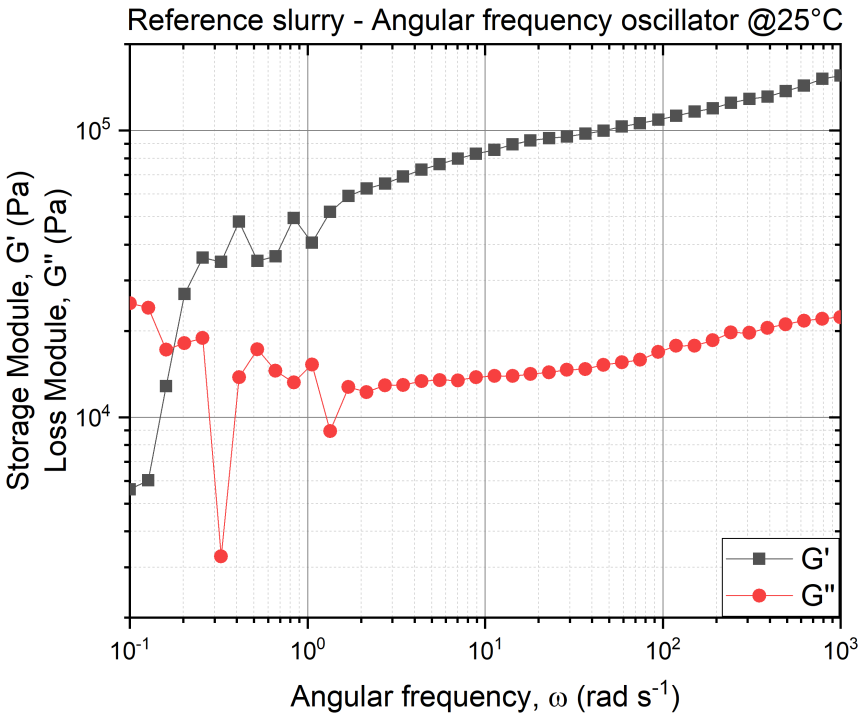

Figure 4.3: Angular frequency oscillator of reference slurry.

Finally, viscoelasticity properties were investigated, as shows Figure 4.3. In the range of low shear rate the two moduli don't follow a constant trend, as the slurry may not be affected by so low angular frequency oscillation, so defining what behaviour it's engaging in can't be defined definitely, even if the distinction of the two moduli is evident. On the contrary, for frequency higher than 1 rad/s the trend is more evident, with an higher distinction in terms of order of magnitude between them. According to literature, the slurry is behaving like a viscoelastic solid, meaning that links inside the material, i.e. chemical bonds or physical-chemical interactions, are strong, which it's a feature needed for a good quality coating.

4.2 AC slurry

Considering all these results as a comparison component in further analysis, it has been shifted to the AC YP80F investigation. Since no slurry recipe was studied for this material, starting from the original recipe an empirical assessment of how much solvent was needed was carried out, because the larger surface area in this case resulted in an increase in the amount of water. From that assumption, using the reference recipe as starting point, three different slurries were made and investigated. Among the three, one was visually too liquid, another had the minimum amount of solvent for the liquid to be homogeneous and still be a slurry, and the last one was in the middle between the two one. All the main information are reported in table 4.1.

Table 4.1: Table of slurries investigated w.r.t. the reference one. Here are reported the volume of solvent per total of mass and the density of binder CMC in the recipe formulation.

Code	**AC**	**Volume per grams**	$\rho_{\mathbf{CMC}}$	**Comments**
C5R	YP-50F	3.7 mL/g	6.76 mg/mL	Reference slurry
C8.1	YP-80F	4.7 mL/g	4.25 mg/mL	Too liquid slurry
C8.2	YP-80F	4.5 mL/g	4.44 mg/mL	Middle slurry
C8.3	YP-80F	4.3 mL/g	4.65 mg/mL	Min. solvent slurry

In analysis, the sample C8.1 (Figure 4.4) had characteristic similar to the reference one in terms of viscosity response of a shear rate. As before, it's possible to note a increase of viscosity/shear stress at @35°C, leading again to a drying process of the slurry for these temperatures, but not the case of @30°C, which follows the same trends of the others. A reason of this can be the higher volume fraction of solvent, which requires higher temperature in order to dry it. Instead, it's must be highlight a decrease of an order of magnitude for the viscosity, which is reasonable because of the too liquid nature of the fluid. In this case particles are freer to move into the fluid, since the amount of solvent is higher, so the time relaxation is lower for the lowest temperature. In addiction, there's no significant variation in the overall time requested according to the trends, meaning that temperature doesn't affect viscosity relax of slurries with high solvent volume. Despite the excess of DI water, the slurry still behaves like a viscoelastic solid, so the internal bonds are still a predominant property and resistant against external forces.

However, the order of magnitude of the two moduli is decreased by three orders and the difference between them is lower, which means that, actually, bonds are

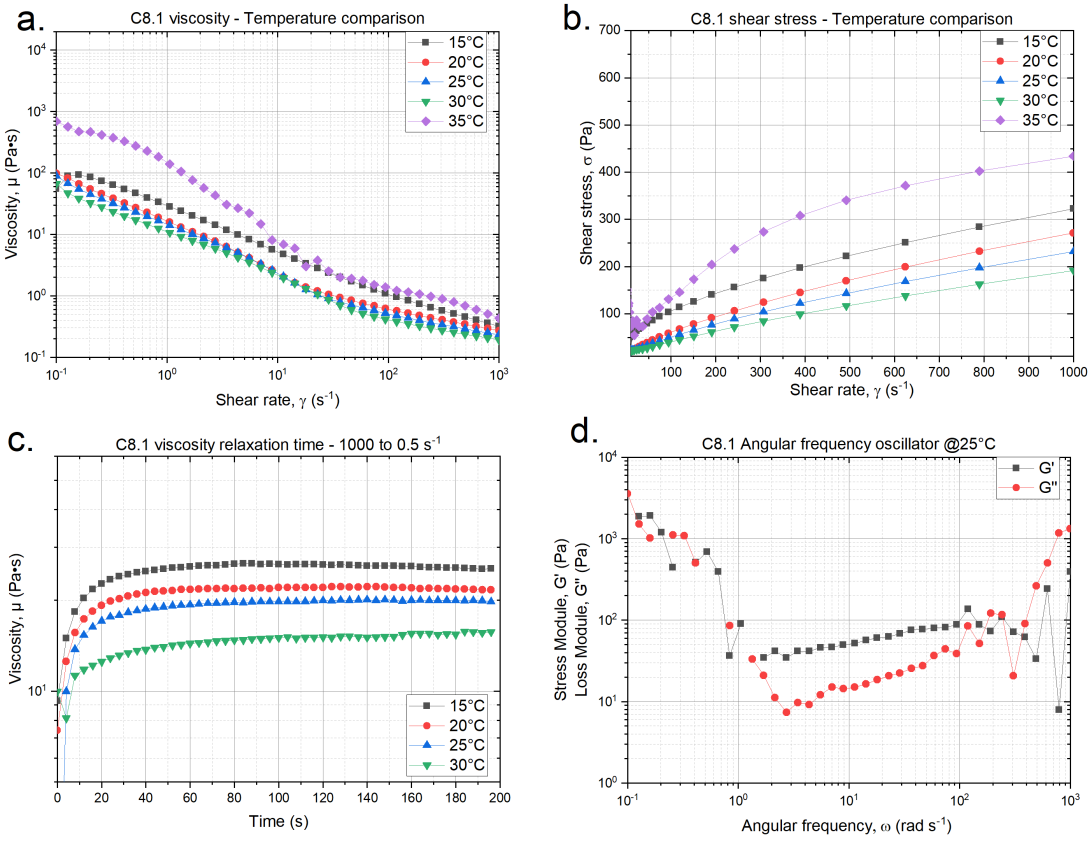

Figure 4.4: Rheology results of the sample C8.1. In order: (*a*) Viscosity VS shear rate and temperature; (*b*) Shear stress VS shear rate and temperature; (*c*) Relaxation time of viscosity VS temperature; (*d*) Angular frequency oscillation at @25°C.

weaker than before, as one can see for the highest angular frequency, in which the loss moduli overcomes the storage one.

Quite similar situation is the one showed by the sample C8.2, in Figure 4.5. As it happens for the reference slurry, the drying step starts at @30°C, mainly due to a lower volume of solvent fraction, but the viscosity is still comparable with the other cases. In relationship with the C8.1 sample, also here the relaxation time isn't affected by the temperature, since the variation isn't significant between each other. The characteristic of solid viscoelastic here is more evident w.r.t. the previous sample, even if the order of magnitude is still lower than the reference one and the difference between the two moduli is not so marked, leading to the statement that bonds between particles are less strong.

Finally. results of C8.3 sample are plotted in Figure 4.6. Considering the fact that the quantity of solvent is the minimum that allows to obtain an homogeneous

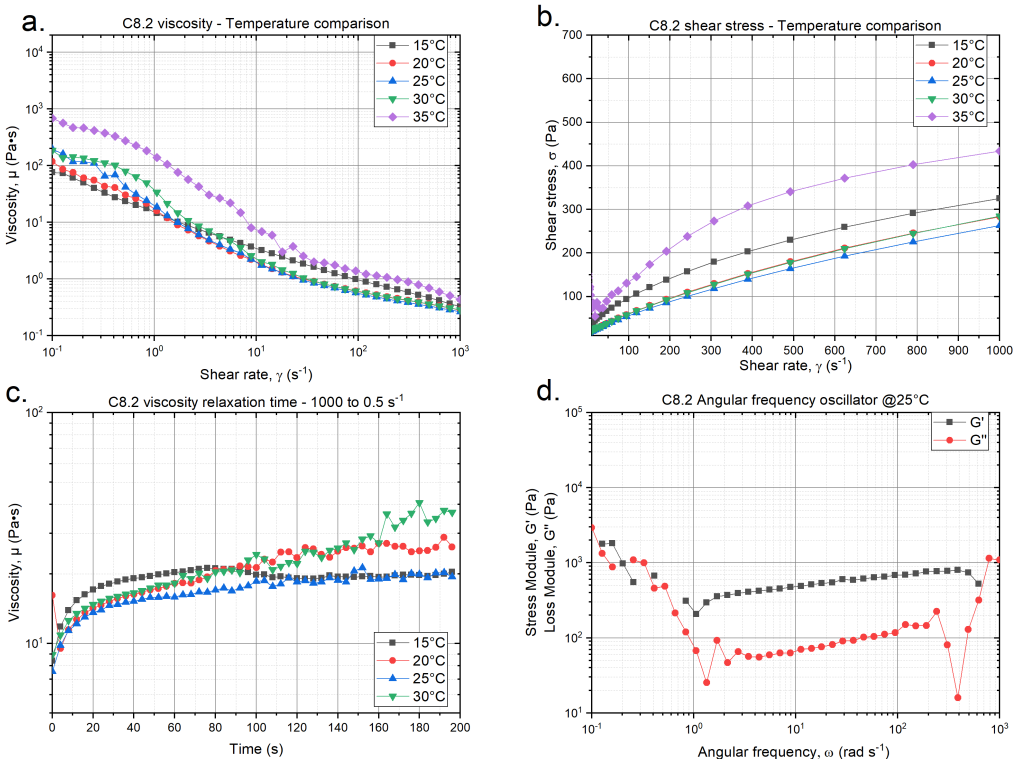

Figure 4.5: Rheology results of the sample C8.2. In order: (*a*) Viscosity VS shear rate and temperature; (*b*) Shear stress VS shear rate and temperature; (*c*) Relaxation time of viscosity VS temperature; (*d*) Angular frequency oscillation at @25°C.

liquid slurry, the viscosity has an order of magnitude higher than the previous sample, and values that are comparable with the reference one. However, the increase in viscosity starts at @20°C, meaning that the drying process is brought forward to lower temperatures. Premature drying could affect the uniformity of the coating, creating local gradients, but also prevents the slurry from slipping on the current collector foil and preventing unevenness on the coating area. In contrast with the so far obtained results, relaxation time in this case shows a opposite trend, as the time required is higher for higher temperature. A explanation of this behaviour can be due to the reduction of DI water in the slurry solution, moving the point of view from a liquid to a paste. This property can be an advantage since the coating can have more time to self-leveling the surface area without additional step. Correlated to the reference case, the viscoelastic properties of this sample are relative to a solid viscous, in which the internal bonds are resilient to external forces as the two moduli are an one order of magnitude apart.

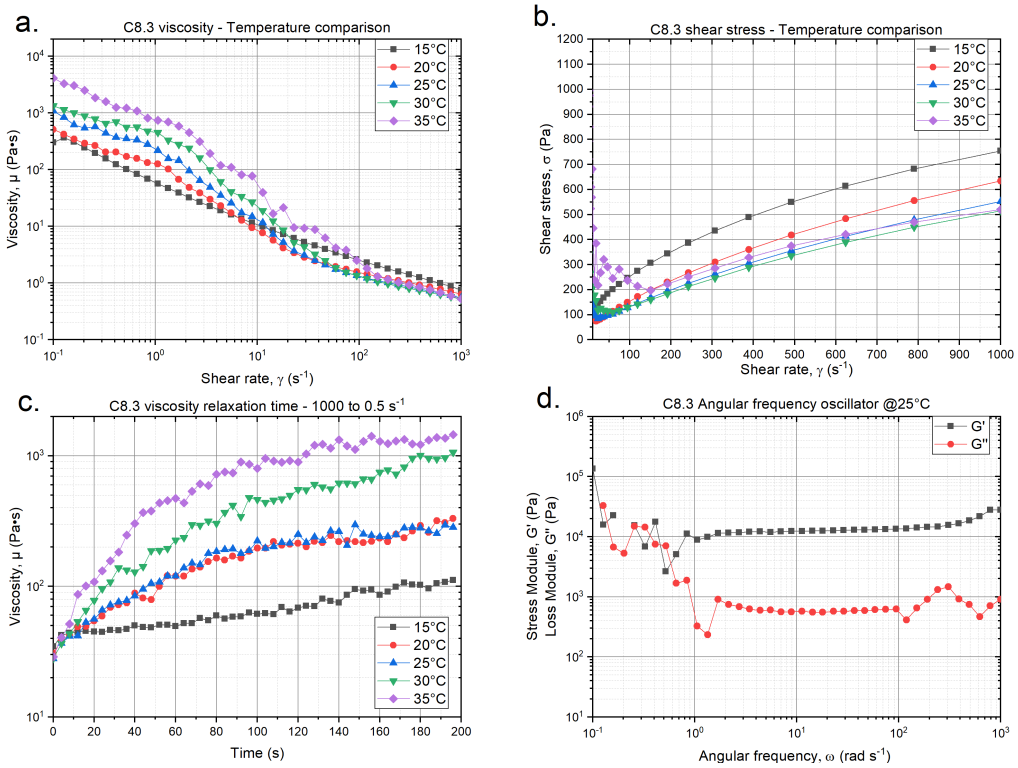

Figure 4.6: Rheology results of the sample C8.3. In order: (*a*) Viscosity VS shear rate and temperature; (*b*) Shear stress VS shear rate and temperature; (*c*) Relaxation time of viscosity VS temperature; (*d*) Angular frequency oscillation at @25°C.

In a system where the temperature is controllable precisely, the C8.3 one is the best, as it shows characteristics similar to the reference one and has good features than are easily exploitable in a R2R coating system. However, in a system where temperature fluctuates in a wide range without control, C8.2 is better, as it's less sensible to environment temperature. In general, increasing the solvent fraction in a slurry can decrease the dependency on temperature in a R2R system. Figure 4.7 is reported for the comparison between each samples at room temperature set at 25°C.

4.3 MnO_2 and Super C65 slurries

Continuing this thread, a further analysis was made for the other two material: MnO_2 and Super C65 carbon-black. In these case, the samples chosen were the one that has the minimum solvent fraction for a liquid slurry.

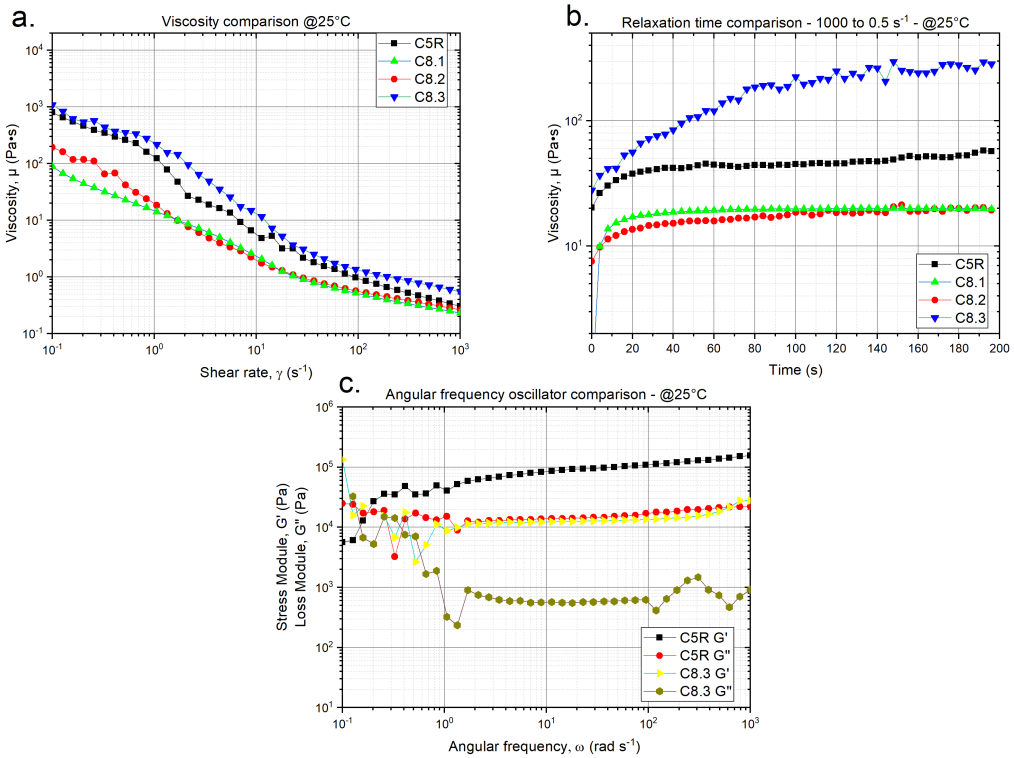

Figure 4.7: Rheology results of AC results in comparison with the reference one @25°C. In order: (*a*) Viscosity VS shear rate, comparison of the order of magnitude; (*b*) Relaxation time of viscosity, time required in comparison; (*c*) Angular frequency oscillation at @25°C, only ref. and C8.3 reported.

Table 4.2: Table of slurries investigated in this thesis. Here are reported the volume of solvent per total of mass and the density of binder CMC in the recipe formulation.

Code	**AC**	**Volume per grams**	$\rho_{\mathbf{CMC}}$	**Comments**
50R	YP-50F	3.7 mL/g	6.76 mg/mL	Reference slurry
80	YP-80F	4.3 mL/g	4.65 mg/mL	AC slurry
MnO	MnO_2	3.9 mL/g	6.41 mg/mL	MnO_2 slurry
C65	Super C65	19 mL/g	2.63 mg/mL	Carbon black slurry

Table 4.2 reports all the main information for all the slurries investigated during the thesis. A particular case was the carbon black, as for small quantities of material the requested solvent in order to get an homogeneous liquid was much

higher than the other cases.

Despite a similar situation of C8.3 sample, in which the solvent fraction is kept to the minimum level, the viscosity of sample MnO_2 didn't show a markable dependency on temperature, ans also there's no dry effect at higher temperature. Must be take into account that the active material used is different w.r.t. the activated-carbon, so properties can be different also in terms of rheology. Even if in the range 15 - 25 °C the viscosity follows the trend of an internal evaporation for solvent, it seems that higher temperature affects structure of particles weakening their bonds, leading to a decrease in viscosity. However, there's correlation for the time relaxation and angular oscillation measurements between this sample and the others. Heating the slurry decrease its relaxation time from several tens of seconds to a couple of tens. Oscillation mode test confirms the elastic solid nature of the sample.

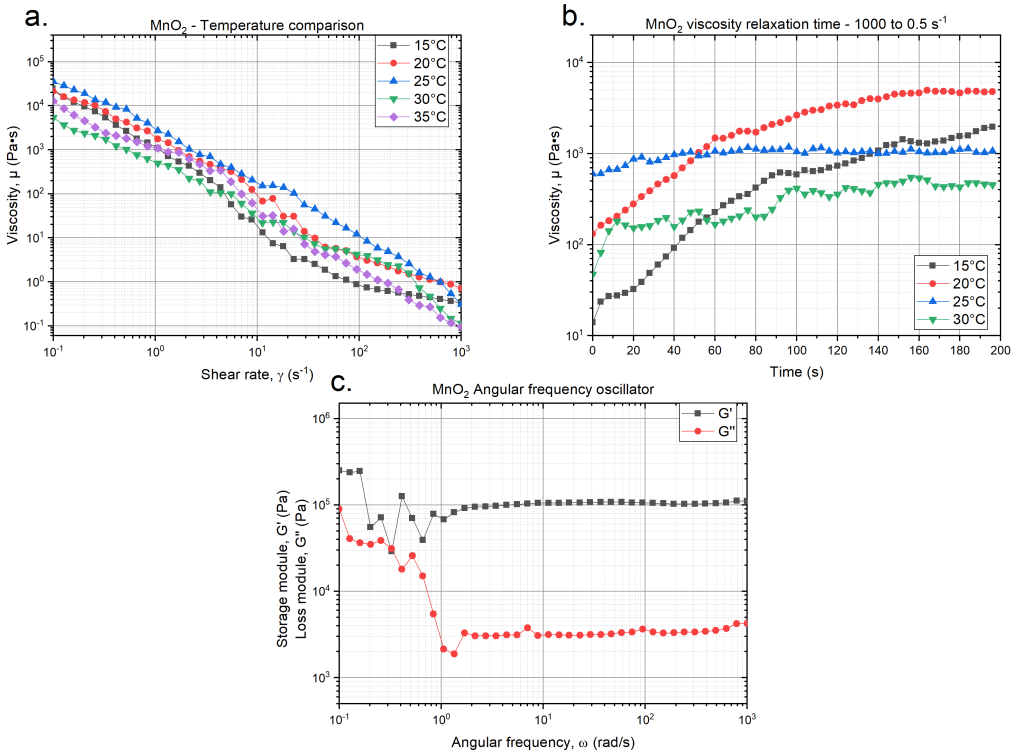

Figure 4.8: Rheology results of MnO_2 sample. In order: (*a*) Viscosity VS shear rate and temperature; (*b*) Relaxation time of viscosity VS temperature; (*c*) Angular frequency oscillation at @25°C.

Similar situation was found in the carbon black sample (Figure 4.9). Here the effect of temperature is correlated to the evaporation of solvent, since the viscosity

is slightly increasing to higher value. The difference isn't so significative, as the magnitude is kept at the same order. A note must be said about the range of values, which is comparable with the other samples, as it wasn't expected, since the amount of solvent added to reach an homogeneous slurry was much higher than the other sample in comparison with the active material mass. Relaxation time is correlated to the one found for MnO_2 slurry, where the temperature drastically affects its value. Again, the slurry behave like a elastic solid, in which the strength of the bonds is marked by the one order of magnitude of difference between the two moduli.

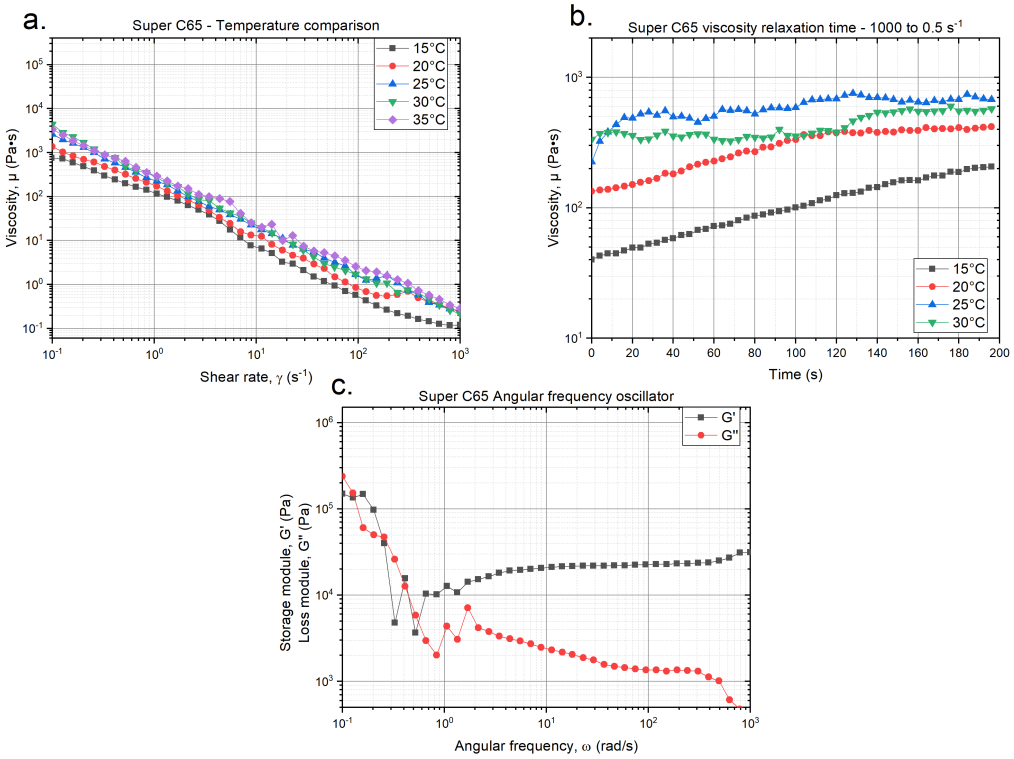

Figure 4.9: Rheology results of Super C65 sample. In order: (*a*) Viscosity VS shear rate and temperature; (*b*) Relaxation time of viscosity VS temperature; (*c*) Angular frequency oscillation at @25°C.

In conclusion, a good choice for electrodes manufacture with slurry coating is to use the minimum solvent fraction required to achieve an homogeneous liquid, in which the internal bonds are resilient to external forces, relaxation time is high enough to provide self-levelling of the surface without encountering the problem of slurry slippage and dependency on temperature doesn't affect the structure of the final coating. However, in case where temperature dependency is so high

that accelerates the drying step even when the coating process isn't completed, from the original recipe it must be added a little quantity of solvent in order to compensate that effect. The additional solvent must not overcome the 5% of the starting volume.

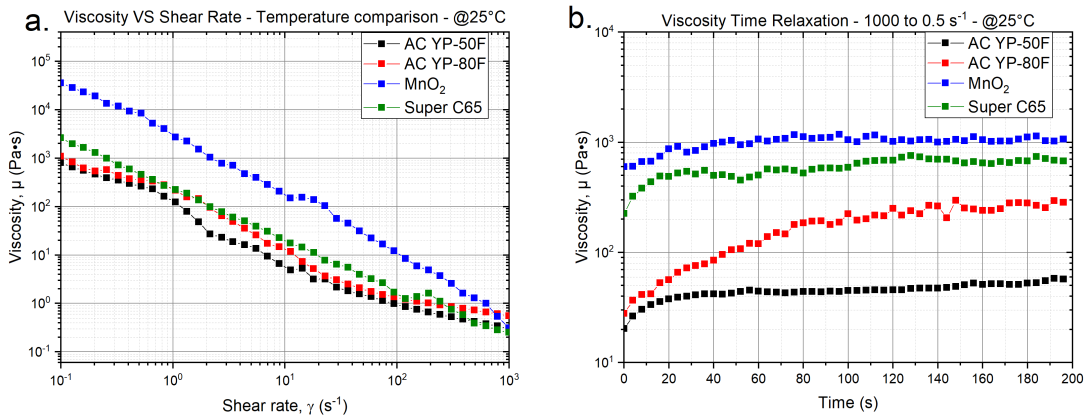

Figure 4.10: All rheological investigation made with samples with different active material. The comparison is set at room temperature (@25°C). In order: (*a*) Viscosity VS shear rate; (*b*) Relaxation time of viscosity

Chapter 5

Electrodes manufacture

5.1 Coating process

When coating topic is treated, arguments like electrode quality and resistance to external forces, such as bending and shear deformation, take the first place. An empirical way to demonstrate the robustness of the coating surface is to apply by hand typical deformations that might happen during assembling the device and see the response of such forces. There are machine that are designed for these operations, but they weren't considered during the development of the thesis. Instead, more recent topics related on manufacturing are reproducibility and scalability of the electrode coating. In an industrial environment, the fact that the process can be repeated achieving the same result, tolerances aside, is necessary in order to provide the same product without further changes in progress.

Assuming the ratio of the component fixed and the slurry well mixed without presence of lumps, the variables that affect the final result are the gap between the substrate and the blade (coating thickness), the solvent fraction of slurries and the active material used. From the coating foil it can be evaluated its thickness, without the contribution of current collector, and the mass of the cut electrode, from which can be extracted parameters as mass loading (mg/cm^2) and density (g/cm^3) of the electrode, evaluated as:

$$M_C = \frac{m_{el}}{A_{el}} \qquad (5.1) \qquad\qquad \rho_{el} = \frac{M_C}{t_{el}} \qquad (5.2)$$

where M_C is the mass loading, m_{el} the electrode mass, A_{el} its surface, ρ_{el} its density and t_{el} its thickness. Different coating were performed taking as slurry samples the one considered during rheology. All the thickness and mass loading are reported in Table 5.1, while each trend against coating thickness is plotted in Figure 5.1. For reference of sample name and ratio volume/mass see Table 4.1.

Table 5.1: Table of thickness and mass loading for each coating test.

Active material	Coating thickness (μm)	Final thickness (μm)	Mass loading (mg/cm^2)	Density (g/cm^3)
AC C8.1				
	150	40.14 ± 2.98	1.61 ± 0.38	0.40
	250	77.20 ± 4.61	3.02 ± 0.39	0.39
	350	97.62 ± 6.23	3.98 ± 0.41	0.41
AC C8.2				
	100	41.25 ± 2.81	1.59 ± 0.39	0.38
	150	65.47 ± 3.32	2.73 ± 0.42	0.42
	200	78.06 ± 4.79	3.51 ± 0.45	0.45
	300	95.59 ± 5.30	4.09 ± 0.43	0.43
AC C8.3				
	60	55.11 ± 2.98	2.17 ± 0.23	0.39
	100	76.00 ± 3.63	2.73 ± 0.33	0.36
	150	84.79 ± 3.74	3.22 ± 0.40	0.38
	200	90.79 ± 6.91	3.72 ± 0.43	0.41
MnO2				
	100	27.10 ± 2.17	2.14 ± 0.30	0.79
	150	35.74 ± 3.63	2.89 ± 0.33	0.81
	200	43.87 ± 3.45	3.42 ± 0.34	0.78
Super C65				
	100	35.00 ± 1.69	0.53 ± 0.06	0.15

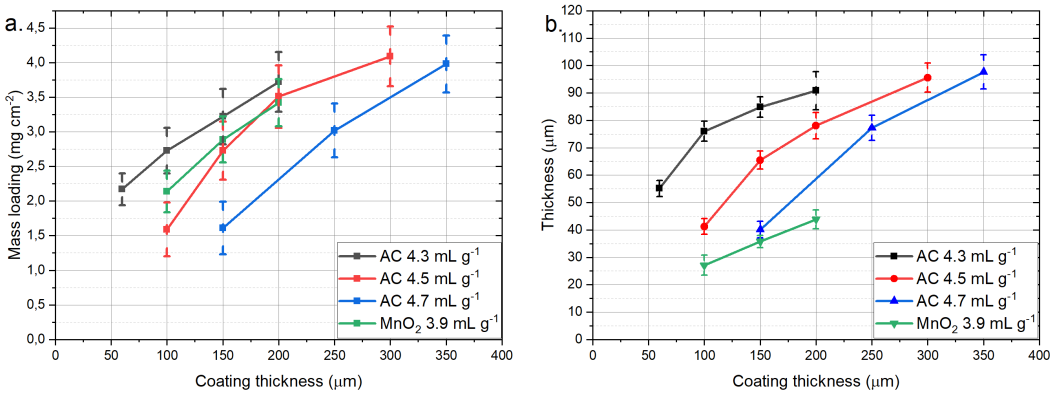

Figure 5.1: (*a*) Variation of mass loading and (*b*) final thickness changing the coating thickness and the type of slurry.

As expected by literature[21], the final thickness grows w.r.t. coating gap in a logarithmic trend. For small gap the increase trend is approximately linear, while for higher gap the slope of the trend starts to decrease. When the gap between the coating blade and the surface is small, the slurry may experience higher levels of shear stress, decreasing the viscosity and leading to follow better the variation of coating gap due to more efficient spreading of the material. As the gap increases, the shear stress decreases, and the coating thickness may increase more slowly due to reduced spreading efficiency. Slurry poured over the tip of the current collector foil showed a maximum height which can be dependent on the contact angle between liquid and foil and surface tension, so this was a limitation in reaching high coating thickness, since the blade couldn't reach the slurry. Particles size of the materials affects the minimum thickness reachable, and this is represented by the difference between the lowest thickness for AC, whose particle size are in the range 3 - 7 μm [22], and the one of MnO_2, in which the size is lower than 1 μm (see Section 6.2). However the lowest value reachable during coating is also dependent on the solvent fraction, which indicates how many particles are contained in a certain volume. In view of a R2R coating system, in which the surface presents slopes, the choice of a more liquid slurry, like in the C8.1 case, may not be a good decision since slips can happen easily, leading to uneven and unlevelled electrode coating.

Through non-linear curve fit, it was possible to define an approximate equation that links coating gap and final thickness and quantify the logarithmic trends, in the form of:

$$y = a + b \cdot ln(x + c) \tag{5.3}$$

where y is the final thickness, x is the coating gap and a, b and c are constant parameters. It must be noted that these equation are valid mainly in the range considered, and going outside that region may leads to imprecise evaluation. The equations evaluated are reported as following:

$$C8.1: \quad t_{el} = -451.66 - 91.14 \cdot ln(t_{coat.} + 77.10)\mu m \tag{5.4}$$

$$C8.2: \quad t_{el} = -77.77 + 31.49 \cdot ln(t_{coat.} - 56.17)\mu m \tag{5.5}$$

$$C8.3: \quad t_{el} = 24.09 + 13.21 \cdot ln(t_{coat.} - 49.54)\mu m \tag{5.6}$$

$$MnO_2: \quad t_{el} = -136.97 + 32.70 \cdot ln(t_{coat.} + 51.32)\mu m \tag{5.7}$$

Mass loading trends is comparable to the one of electrode thickness, as the increments are almost the same. Since the evaluated density for each coating gap and different sample of the same active material is kept to the same value, is

reasonable that the correlation between mass loading and thickness is valid in the acceptable range of tolerance. The mass loading of the MnO_2 is also comparable with the C8.3 one, in which the solvent fraction is kept at its minimum, but instead the thickness of the first is more than half of the second, due to the lower particle size. According to the trends, they're reaching a maximum boundary of 4.2 mg/cm^2, which is comparable with the one found in literature[23]. Same as done with the coating thickness, logarithmic trends of mass loading were estimated using the fit curve in Equation 5.3, where y is the mass loading and x is still the coating gap.

$$C8.1: \quad M_C = -18.60 + 3.73 \cdot ln(t_{coat.} + 73.43) mg/cm^2 \tag{5.8}$$

$$C8.2: \quad M_C = -2.77 + 1.27 \cdot ln(t_{coat.} - 69.06) mg/cm^2 \tag{5.9}$$

$$C8.3: \quad M_C = -13.05 + 2.87 \cdot ln(t_{coat.} + 139.33) mg/cm^2 \tag{5.10}$$

$$MnO_2: \quad M_C = -10.43 + 2.51 \cdot ln(t_{coat.} + 49.76) mg/cm^2 \tag{5.11}$$

In Table 5.1 is reported only one results of Super C65 coating process, as its electrochemical characterizations were still under investigation.

5.2 Calendering process

Calendering step was performed firstly with lower depth of penetration, since the response behaviour of the electrode wasn't known in advance. The choice of the rolls gap was made by looking at the average thickness of the coating and the standard variation of it. Of course the surface isn't completely flat and some zone may not be affected by the calendering step. Figure 5.2 shows the variation of deformation, plastic and elastic, and the springback effect from the initial coating thickness. For ultra-thin coating, the behaviour is mainly elastic, as expected, since the particle distribution has reached minimum porosity already after the coating procedure and further compression can only damage the structure. The ineffectiveness of calendaring in this region is also explained by the SB, whose value is the highest. Increasing the depth of penetration leads only to show more the elastic nature of the electrode, since the high pressure applied will be all transferred to the machine rolls, as it's possible to see in Figure 5.2. Going further to higher thickness the probability to have more porous structure is higher, so compression in that region shows a slightly plastic nature of the electrode, which increases at higher thickness. From the two trends. it seems that high depth of penetration is less effective than the low one. However, must be said that higher depth doesn't mean higher pressure, since its intensity isn't controllable for the machine used and

it's constant. This statement is confirmed by the higher value of SB for the same thickness value, meaning that from the majority of the penetration depth, mostly is elastic.

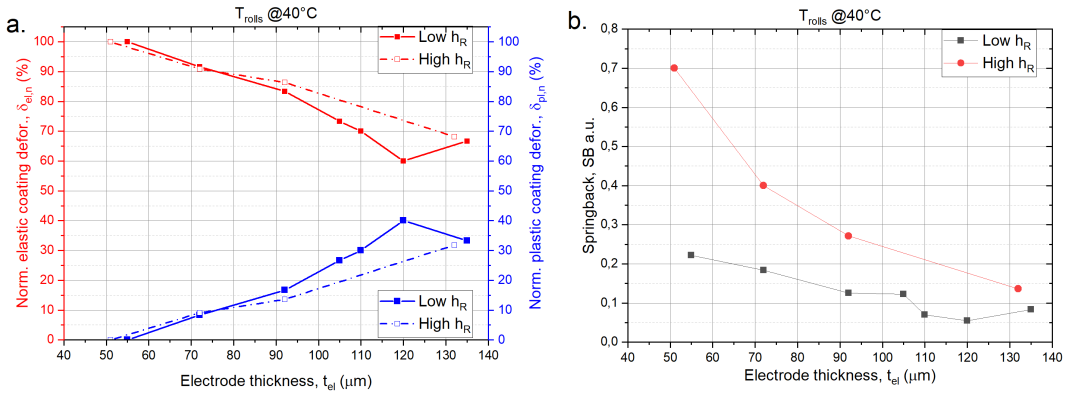

Figure 5.2: Variation of (a) normalized plastic and elastic deformation and (b) springback effect versus the electrode thickness. Differences are reported between low and high depth of penetration.

Electrodes with and without calendering step were investigated through impedance spectroscopy, in order to evaluated the effect for that process. As different thickness provided different results in terms of elastic and plastic deformation, EIS made with low and high mass loading were distinguished. Both in the two cases (Figures 5.3 and 5.4) no major differences were found.

Table 5.2: Evaluated values of ESR and IR for the low and high mass loading sample, with and without calendering step

	$\mathbf{ESR}_{no\ cal.}$ (Ω)	$\mathbf{IR}_{no\ cal.}$ (Ω)	$\mathbf{C}_{no\ cal.}$ (F/g)	$\mathbf{ESR}_{cal.}$ (Ω)	$\mathbf{IR}_{cal.}$ (Ω)	$\mathbf{C}_{cal.}$ (F/g)
Low M_C	4.70	18.58	63.56	4.42	15.74	64.78
High M_C	5.06	16.45	61.67	4.55	15.31	62.35

In the low mass loading, a decrease in ESR and IR are noted (Table 5.2), and an attenuation of high frequency semicircle is reported, not, however, a complete disappearance, meaning that interfacial impedance occurring at the current collector/active material interface is still present. Specific capacitance evaluated with Equation 2.13 shows also no significant variation between calendering and not, which is also expected since the porosity of the structure didn't changed. For the same case, a little circle in the transition from interfacial impedance to Warburg diffusion is reported, which lead to a first decrease in real part. This behaviour may

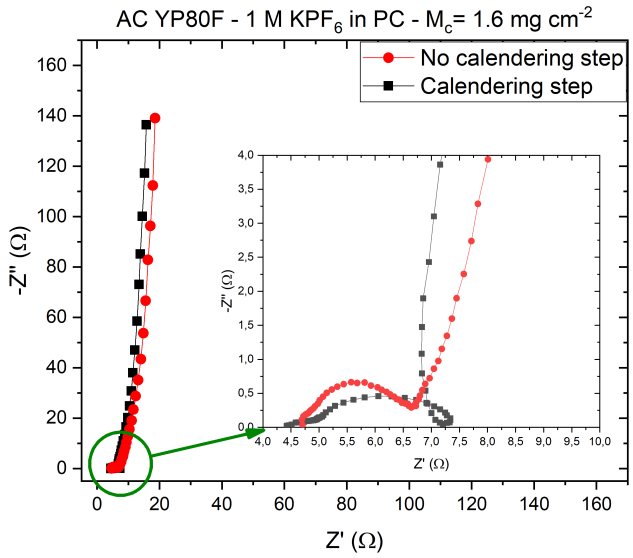

Figure 5.3: EIS of two electrode samples, with and without calendering step, at low mass loading.

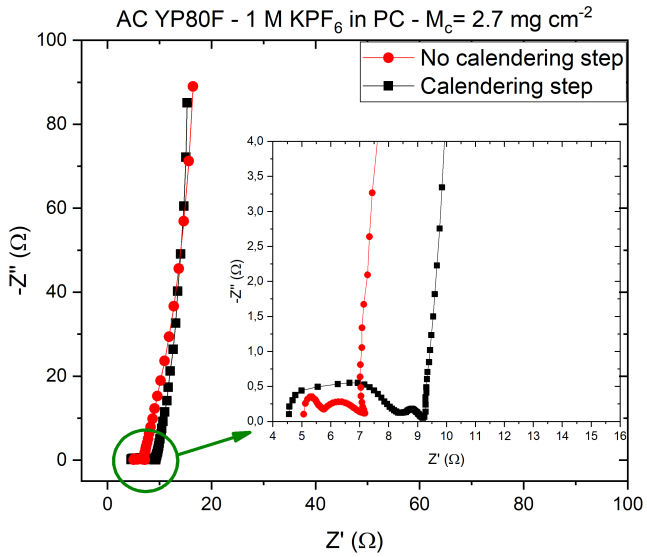

Figure 5.4: EIS of two electrode samples, with and without calendering step, at high mass loading.

be related to a inductance contribution due to bad contact between swagelok steel contact and WE/CE. Similar situation is reported in the high mass loading, but instead of attenuating the high frequency semicircle, it has been amplified. It was noted during calendering operation that the probability to generate cracks into the structure was much higher when high mass loading coating surfaces were considered, and this can be a reason of the increase of interfacial impedance contribution.

In conclusion, for how the coating procedure was designed for this thesis, calendering step isn't needed, since its contribution in improving the performance can be considered negligible, and the drawbacks found in the electrode characterization can be fixed adjusting the slurry and coating design.

5.3 Roll-to-roll electrodes

R2R coating was made by preparing a higher quantity of slurry (10 g of active material) using the same recipe studied before. In addition, the complete slurry was additionally stirred with MTI® corporation MSK-SFM-16 Compact Dual-Shaft Planetary Vacuum Mixer for almost an 1 hour, in order to provide uniformity before coating.

Investigation of R2R coating system started with the reference slurry and the most liquid sample of AC. The blade gap was set to 150 μm as a matter of comparison w.r.t the one made in laboratory and the current collector roll used was aluminum. The reference slurry behaved as planned, the coated zone were almost equals between each other and irregularities in the expected shape were still acceptable. However, as expected, the procedure with the most liquid one didn't provide an homogeneous and perfect coated surface (Figure 5.5), since during the high descent/climb of the coating and carrying roller the slurry started to slip on the aluminum foil. This leads to top zone where slurry didn't stick and bottom one where the deposited slurry was comparable to the setted gap and led to spills on the edges.

Confirmed the inability of this system to perform coating with liquid slurry, the sample with the minimum fraction of solvent was considered, in the same condition made before. Despite the good quality found during rheology investigation, also this test didn't went as planned, as slippage and poor adhesion to the aluminium foil also occurred in this test. The reason of this failure must be searched in temperature. Despite the controlled environment temperature of the room, the main issue found was the not-controlled plate and the rollers temperature, since their materials, mainly aluminum alloy, conduct heat very well, thus altering the local slurry temperature and changing its properties.

A way found to overcome these issues was to preheat with an external heat source the zone that are directly in contact with the slurry and change the sample

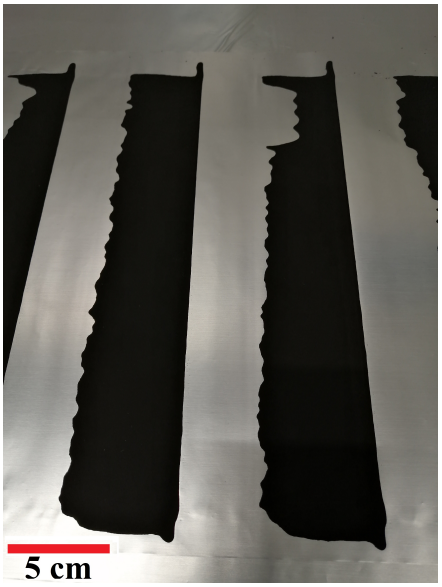

Figure 5.5: A R2R coating made with the most liquid slurry. As shown, the coating didn't go well, due to slurry slipping on the bottom.

with less dependency on temperature variation and less solvent fraction (sample C8.2). Notwithstanding the fact that the heating action is not automatic and cannot be controlled directly by suitable instrumentation inside the machine, the coating test performed with 100 μm of coating gap went as planned, as Figure 5.6 shows.

The average thickness and mass loading measured with different samples were respectively 57.57 $\pm$ 3.17 μm and 2.13 $\pm$ 0.40 mg/cm^2, which are higher w.r.t. the one evaluated in laboratory at the same condition. A possible reason of these differences is due to a non negligible evaporation of solvent when bulk slurries are prepared. This drawback must be take into account during the coating step or directly corrected by preparing the slurry into a hermetically closed system, which wasn't within reach during the course of the thesis.

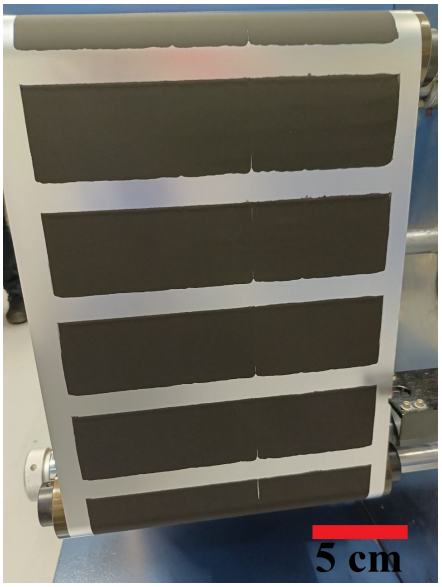

Figure 5.6: R2R coating where pre-heat of the surface was done before. The almost rectangular shape is the one expected. A little non-coated line zone is present, mainly due to the presence of a loose lump.

Chapter 6

MnO_2 synthesis

6.1 XPS

The XPS investigation was performed by considering two different samples of MnO_2 powder, whose main difference concerns the cleaning process after filtering it. The first one was cleaned only with the determine volume of DI water, while the second one was further cleaned by analysing the waste water conductibility until it reaches values near 4-5 $\mu S \cdot cm$. From the wide energy scan (Figure 6.1) the main peaks of the elements considered for the powder measurement in question are indexed.

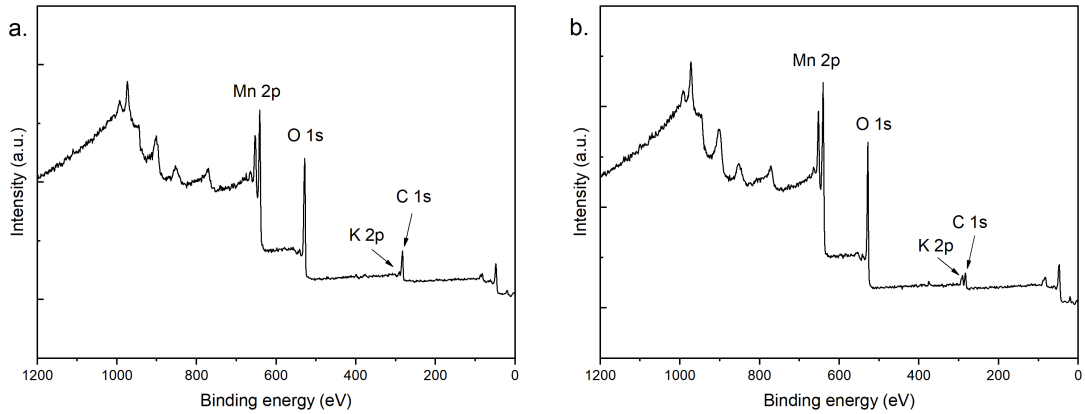

Figure 6.1: Wide energy scan of the two sample. In order: (a) first sample with no additional clean step, (b) second sample with additional clean step.

The noticeable differences are minimal, as the peaks have comparable intensities between the two graphs, so for further investigation of the quantity of them, the Table 6.1 is shown. In the cleaner sample, percentages of Mn and O are slightly higher than the other one, which can be related to a lower contamination of other element, so a more pure MnO_2

Table 6.1: Atomic percentage of all the considered element during wide energy scan of the two sample.

	C (at. %)	**O (at. %)**	**Mn (at. %)**	**K (at. %)**
1^{st} sample	27.04 ± 0.756	47.61 ± 0.672	24.91 ± 0.619	0.44 ± 0.124
2^{nd} sample	13.49 ± 0.681	52.66 ± 0.638	31.82 ± 0.583	2.04 ± 0.17

For further details of each peaks, high resolution (HR) measurements were made. The binding energy position is tabulated, however it must always be referred to a calibration peak, which in our case it was the C-C peak of Carbon at 284.8 eV. The peaks under investigation were:

- C1s + K2p: since they are closer to each other, they're acquired together. C1s peak is needed for measurement calibration, since usally is referred to environmental contamination of the powder;
- O1s;
- Mn2p + Mn3s: due to the multiple oxidation state that Mn has, the evaluation of the actual state is based on position and distance between the two peaks.

HR measurements of C1s + K2p are reported in Figure 6.2. C1s spectrum is the one related to environmental contamination, even if the intensity of this pollutant is lower in the second sample, as expected. Concerning K2p analysis, the $K2p_{1/2}$ peak has half the area of the $K2p_{3/2}$ one, its position at about 292.5 eV and the distance between the two doublets ($\Delta = 2.77$ eV) confirms the K-O bond[24]. According to reaction 3.1, the nature of the bond might be traces of K_2SO_4, but since S presence isn't evident, it could be contamination of $KMnO_4$ or K_2MnO_4. Table 6.2 reports the binding energy of bonds and their intensity.

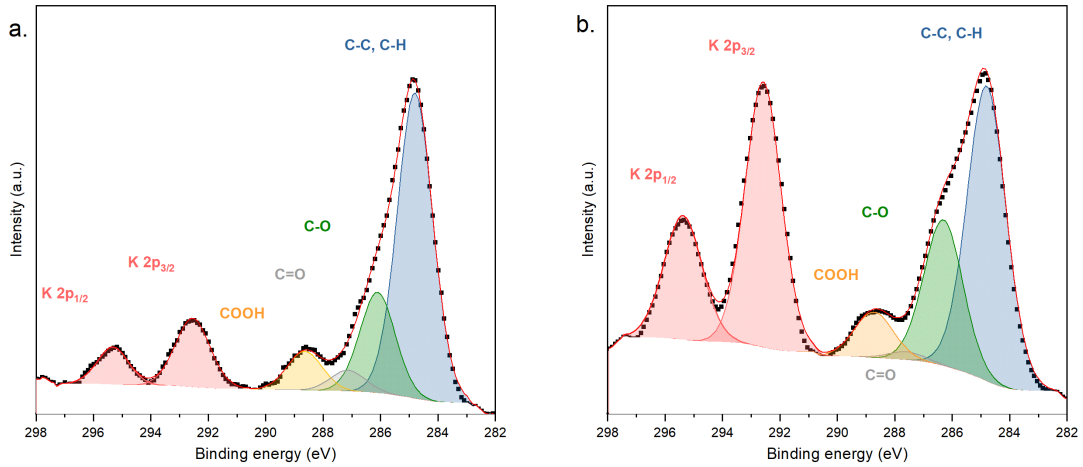

Figure 6.2: High resolution peaks analysis of the couple C1s and K2p. In order: (*a*) first sample with no additional clean step, (*b*) second sample with additional clean step.

Table 6.2: Binding energy and their intensity in percentage of the bonds considered in HR of C1s / K2p.

	C-C		**C-O**	
1^{st} sample	284.8 eV	65.41 %	286.1 eV	21.63 %
2^{nd} sample	284.6 eV	59.48 %	286.3eV	29.49 %
	C=O		**COOH**	
1^{st} sample	287.13 eV	4.56 %	288.64 eV	8.40 %
2^{nd} sample	287.6 eV	1.7 %	288.72 eV	9.33 %

HR analysis of peak O 1s is reported in Figure 6.3. Inside it, the 3 components of Mn oxide (latex oxide, defective oxide/hydroxide, water adsorption)[25], the contributions of contaminant C bonded with O (organic C) and K_2MnO_4 must be found. Decomposed peaks and their intensity are reported in Table 6.3.

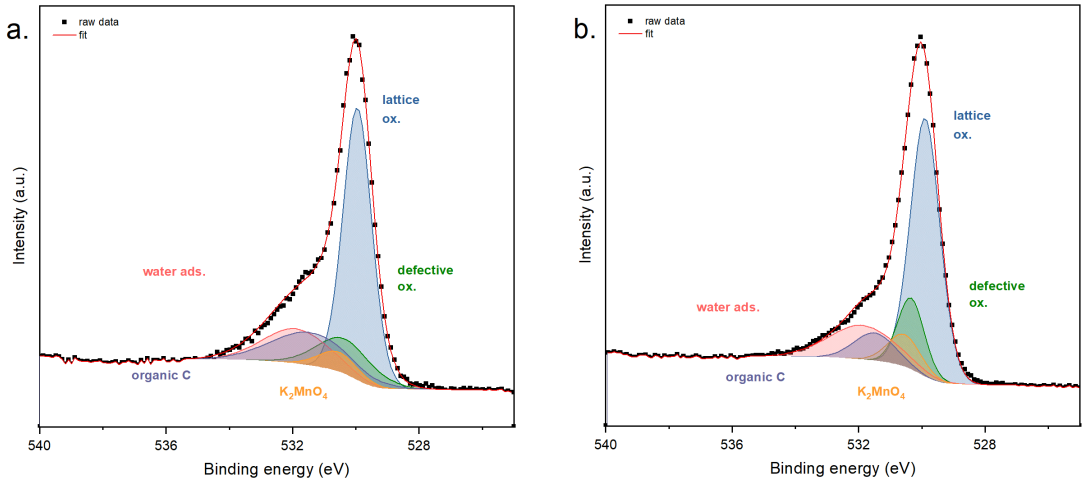

Figure 6.3: HR peaks analysis of O 1s. In order: (a) first sample analysis, (b) second sample analysis.

Table 6.3: Decomposition peaks and their intensity of O 1s.

	O 1s – lattice ox		**O 1s - defective ox.**		**O 1s – water ads.**	
1^{st} sample	529.94 eV	50.43 %	530.34 eV	12.61 %	531.89 eV	15.12 %
2^{nd} sample	529.89 eV	54.33 %	530.34 eV	13.58 %	531.89 eV	16.29 %
	O 1s – organic C		**O 1s – K_2MnO_4**			
1^{st} sample	531.44 eV	16.71 %	530.55 eV	5.12 %		
2^{nd} sample	531.5 eV	8.17 %	530.55 eV	7.62 %		

Going further with the investigation, Figure 6.4 reports the HR analysis of Mn2p and Mn3s. It can be noticed that the two samples are almost superimposable, barring a slight shift in energies, leading to the assertion that the synthesis is reproducible. By looking at the shape and the peaks difference of Mn3s, and comparing this evaluation with the Mn2p peak shape, it's possible to determine oxidation state of Mn. According to the evaluated shift, reported in Table 6.4, and comparing these values with reference values[25], it has been confirmed that the powder under analysis is effectively MnO_2.

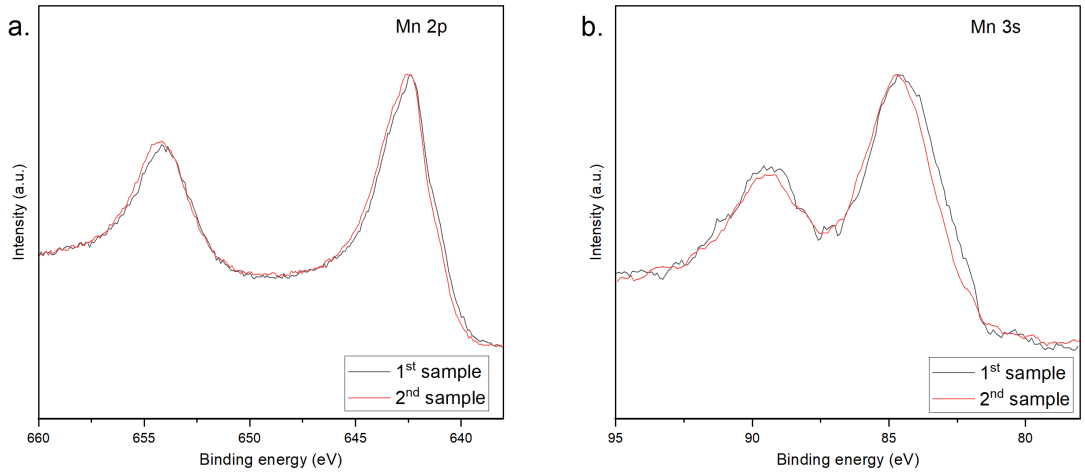

Figure 6.4: HR peaks analysis of both Mn2p and Mn3s. In order: (*a*) Mn2p analysis, (*b*) Mn3s analysis.

Table 6.4: HR peaks and Δ evaluation of Mn2p and Mn3s for both the samples.

1^{st} sample	**Peak**	**Δ**	**2^{nd} sample**	**Peak**	**Δ**
Mn 2p	642.38 eV	11.5 eV	Mn 2p	642.33 eV	11.8 eV
Mn 3s	84.40 eV	4.9 eV	Mn 3s	84.60 eV	4.7 eV

$Mn2p_{3/2}$ peak can be deconvolved into tabulated peaks (without physical sense) to confirm what you get from analysing the Mn3s peak. In total, there are 6 peaks of MnO_2, mainly with mathematics' meaning, and only one of the salt K_2MnO_4. The magnitude and decomposition of these peaks are reported in Table 6.5

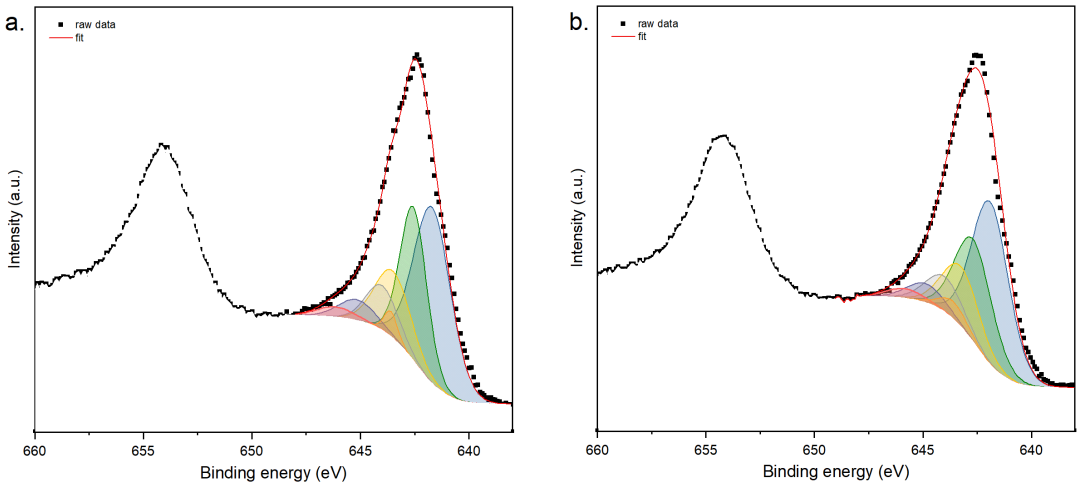

Figure 6.5: HR decomposed peaks of Mn 2p. In order: (a) first sample analysis, (b) second sample analysis.

Table 6.5: Decomposition peaks and their intensity of Mn 2p.

	Mn 2p(1)		**Mn 2p(2)**		**Mn 2p(3)**	
1^{st} sample	641.7 eV	40.82 %	642.56 eV	25.71 %	643.50 eV	15.10 %
2^{nd} sample	641.9 eV	40.42 %	642.67 eV	25.46 %	643.26 eV	14.95 %
	Mn 2p(4)		**Mn 2p(5)**		**Mn 2p(6)**	
1^{st} sample	644.01 eV	8.89 %	645.16 eV	4.77 %	646.16 eV	2.41 %
2^{nd} sample	644.01 eV	8.81 %	644.88 eV	4.73 %	645.56 eV	2.38 %
	K_2MnO_4					
1^{st} sample	643.6 eV	2.30 %				
2^{nd} sample	643.6 eV	3.24 %				

6.2 FESEM

To investigate the surface morphology of the MnO_2 electrode, FESEM was characterized, as it shows Figure 6.6. According to the obtained images, particles distribution is almost uniformly distributed in all the area, despite the presence of empty zone in which only carbon black is present. With further magnification, MnO_2 product seems to assume a spherical shape of roughly 300 nm of diameter combined with additional little spheres with just over 100 nm in diameter.

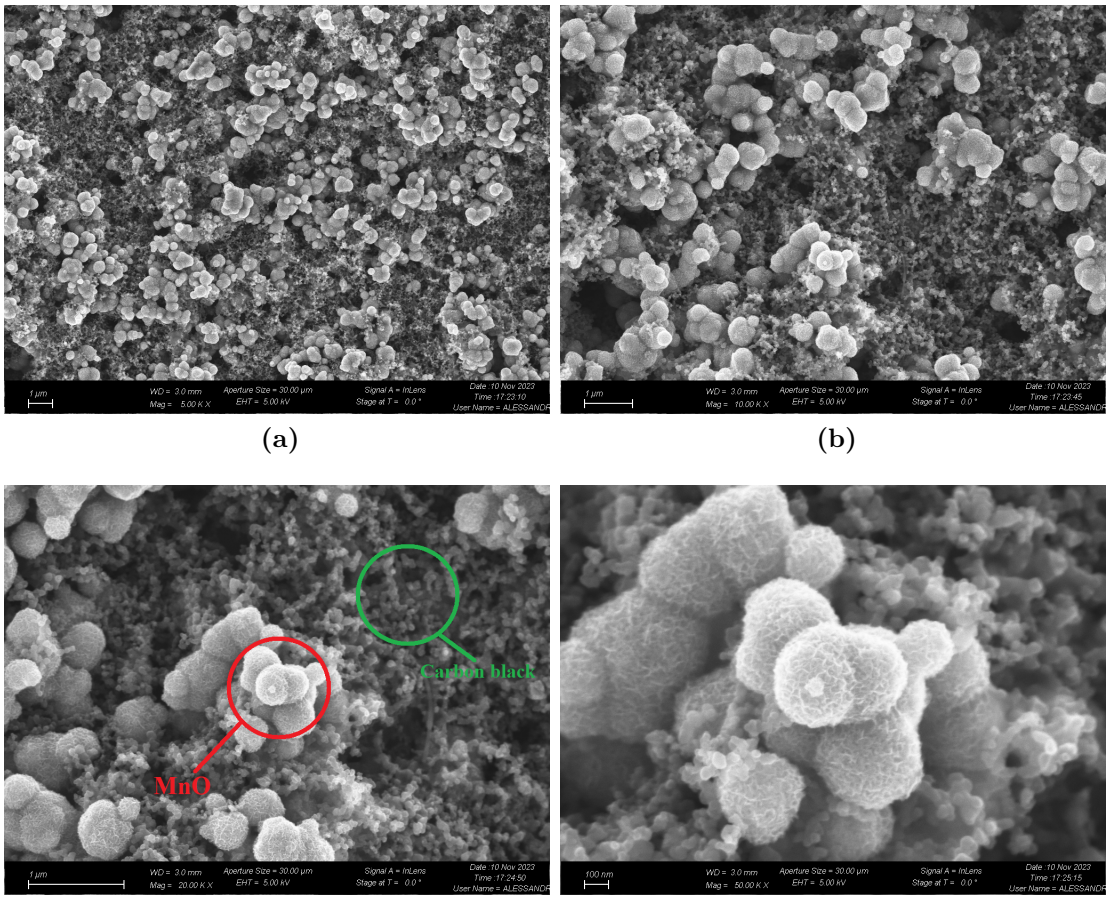

(a) **(b)**

(c) **(d)**

Figure 6.6: FESEM images of a MnO_2 electrode sample under a magnification of: (a) 5000, (b) 10000, (c) 20000 and (d) 50000.

The same type of electrode was again investigated after CV characterization in 0.8 M KPF_6 in EC:DEC, both in anodic and cathodic ESW (Figure 6.7). FESEM images for the anodic case show the presence of few crystalline structures,

attributable to electrolyte salt deposition on the surface, and some long filaments with are glass fiber contamination of the sample, as for avoiding alteration it wasn't cleaned before FESEM. However, the thing that stands out the most is the complete absence of the spherical particles. A reason of this may be due to the over potential applied to the electrode that allowed MnO_2 particles to be soluble into the electrolyte, and this can explain also the complete degradation of the electrode at potential higher than the ESW. For the cathodic case, FESEM images showed a surface completely covered by crystalline structures, mainly electrolyte salt deposition. Also in this case, the almost complete absence of MnO_2 particles may led to assume the solubility of it into the electrolyte.

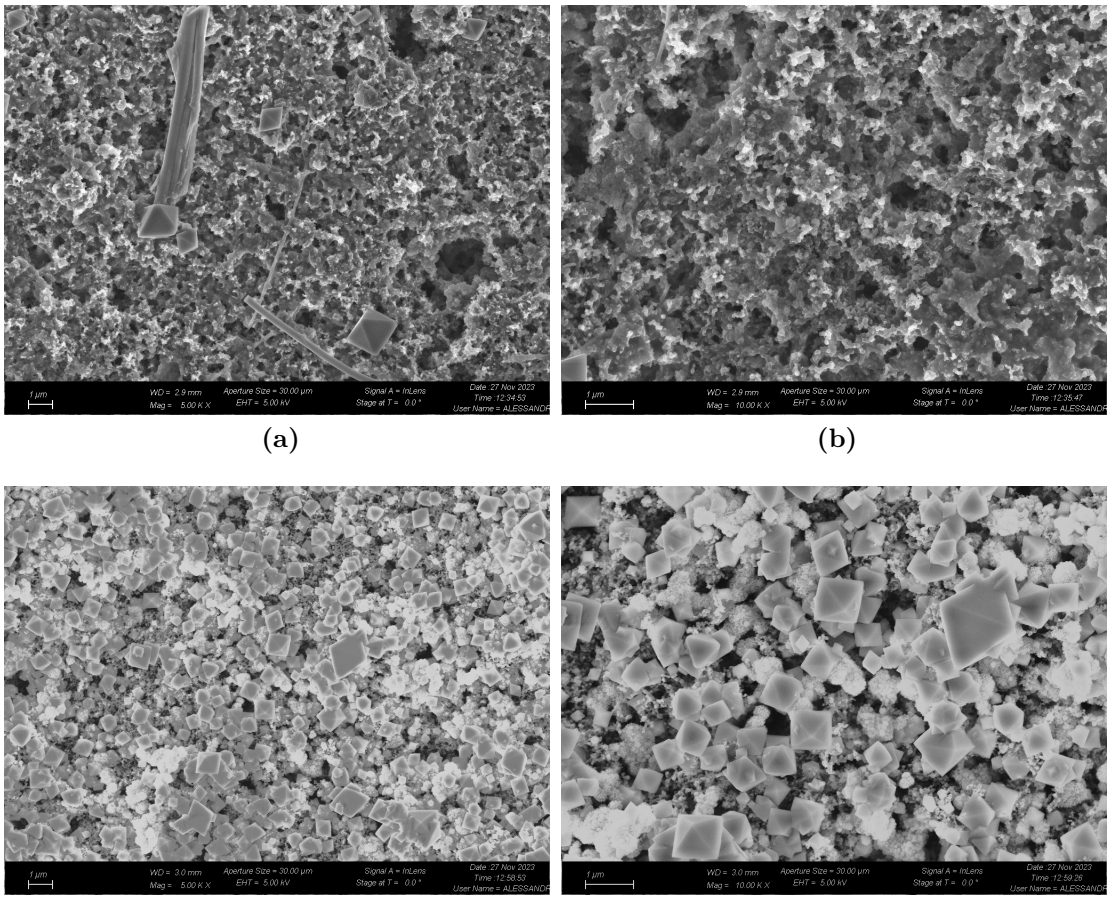

(a) **(b)**

(c) **(d)**

Figure 6.7: FESEM images of a MnO_2 electrode sample after CV characterization in 0.8 M KPF_6 in EC:DEC. In order: anodic potential under a magnification of (*a*) 5000, (*b*) 10000; cathodic potential under a magnification of (*c*) 5000 and (*d*) 10000.

Chapter 7

Electrodes characterization

7.1 AC electrode characterization

In order to define the ESW, separated measurements were performed both in anodic and cathodic window. The scan rate was set to 5 mV/s, which was a good compromise between reliability of results and time required for the complete test. Since is known from literature[21][9] that SCs based on AC electrodes can reach up to 2 V with organic electrolyte, the initial potential window was 0.5 V versus open circuit potential (OCP), and the variation was set to 0.1 V until the condition of coulombic efficiency higher than 99% was no more respected. For each applied potential, were made 50 cycles, as the former can be cycles of adjustment.

7.1.1 1 M KPF_6 in PC

In first analysis, it was considered the electrolyte 1 M KPF_6 in PC, and the results are showed in Figure 7.1 and 7.2. The two boundaries found were respectively 1.2 V and -1.5 V. In the anodic case, coulombic efficiency was always higher than 99%, while the energetic one higher than 90%, except the first cycles in the highest potential. Specific capacitance shows a gradual increase for higher potentials until it settles at a value of 83.93 F/g. Similar behaviour was found for the cathodic one, with the exception that none of the applied potential reached coulombic efficiency higher than 99%, but settled at a value higher than 98%. Taking into account that several measurements reported the same behaviour, it was considered acceptable, despite the original restriction (>99%), and it has been moved to the energetic efficiency, keeping its value higher than 80%. The final specific capacitance was 89.31 F/g, which is still comparable with the anodic one, slightly higher.

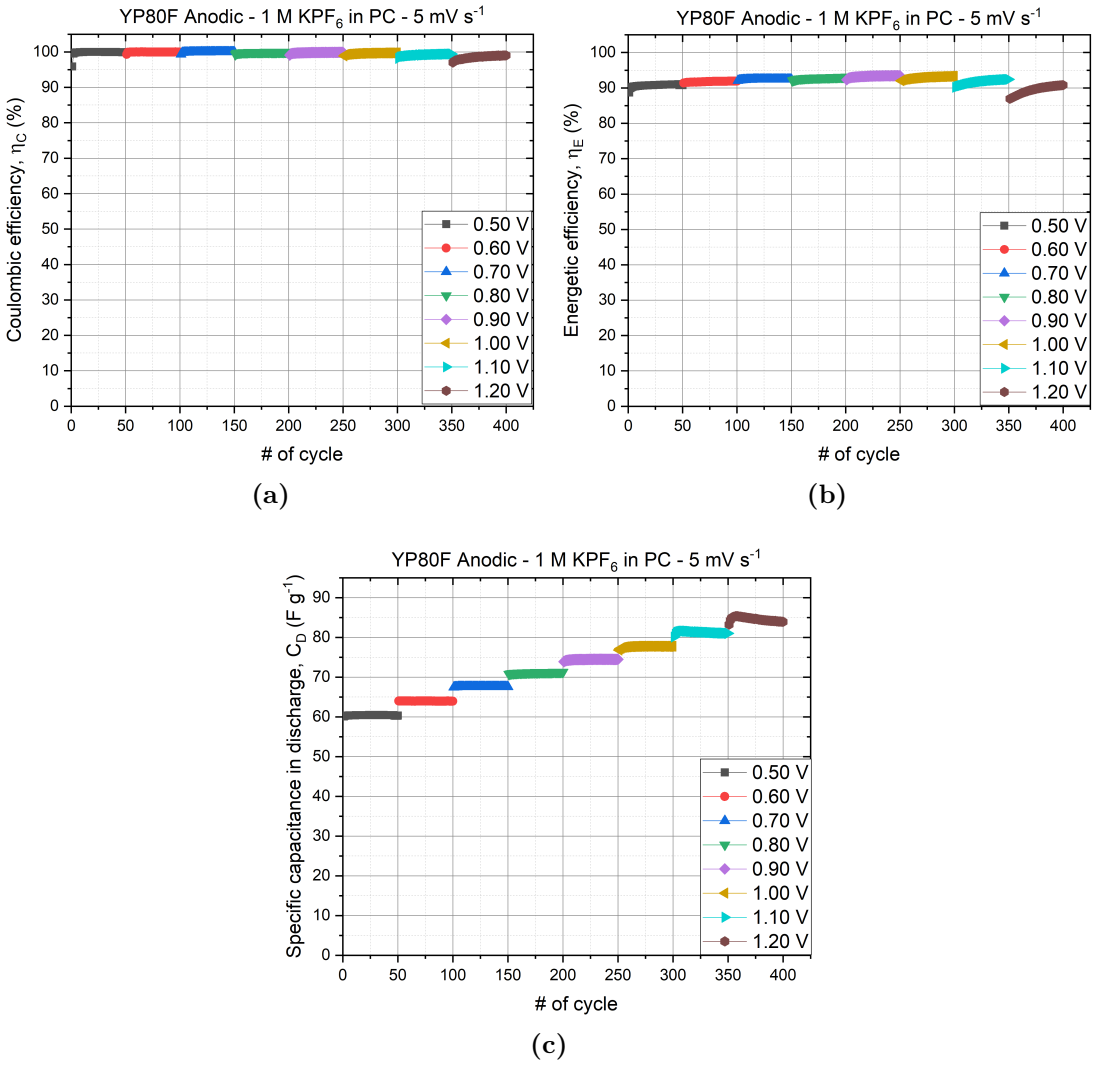

Figure 7.1: AC electrode characterization in anodic potential window in 1 M KPF_6 in PC, separated by each applied potential. For each, there were made 50 cycles. In order: (*a*) Coulombic efficiency; (*b*) Energetic efficiency; (*c*) Specific capacitance in discharge.

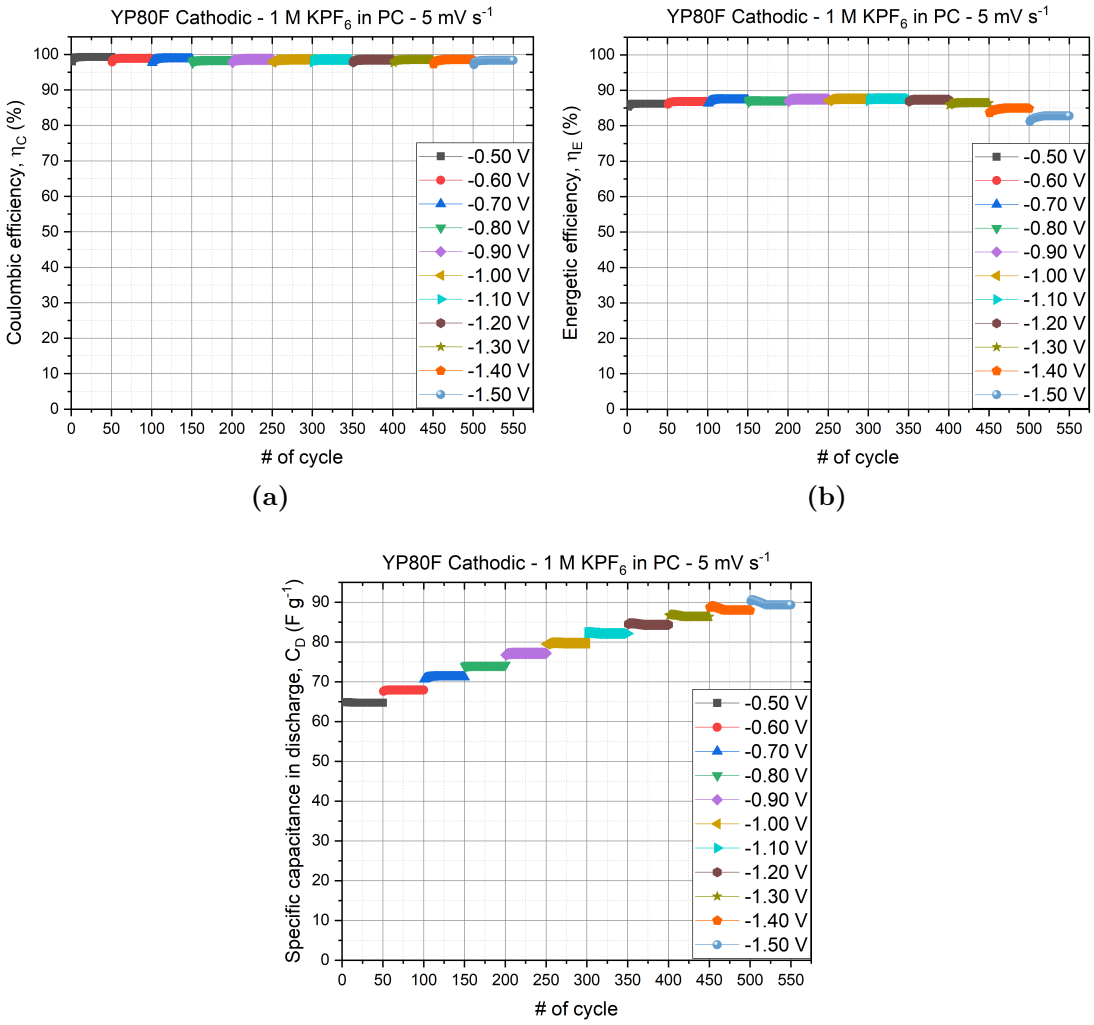

Figure 7.2: AC electrode characterization in cathodic potential window in 1 M KPF_6 in PC, separated by each applied potential. For each, there were made 50 cycles. In order: (*a*) Coulombic efficiency; (*b*) Energetic efficiency; (*c*) Specific capacitance in discharge.

Table 7.1: Evaluated parameters of specific capacitance and efficiencies w.r.t. potential VS OCP of AC electrode, in anodic characterization 1 M KPF_6 in PC.

ΔV VS OCP (V)	**C_D (F/g)**	**η_C (%)**	**η_E (%)**
0.5	60.28	99.92	90.77
0.6	63.96	99.96	91.94
0.7	67.56	99.98	92.42
0.8	71.29	99.97	93.10
0.9	74.47	99.90	93.44
1.0	77.76	99.73	93.30
1.1	81.02	99.41	92.41
1.2	83.93	99.02	90.80

Table 7.2: Evaluated parameters of specific capacitance and efficiencies w.r.t. potential VS OCP of AC electrode, in cathodic characterization 1 M KPF_6 in PC.

ΔV VS OCP (V)	**C_D (F/g)**	**η_C (%)**	**η_E (%)**
-0.5	64.70	99.28	86.23
-0.6	67.93	98.91	86.27
-0.7	71.17	98.70	87.24
-0.8	74.21	98.67	87.37
-0.9	77.15	98.64	87.54
-1.0	79.71	98.61	87.61
-1.1	82.12	98.58	87.65
-1.2	84.32	98.56	87.34
-1.3	86.34	98.50	86.44
-1.4	87.92	98.50	84.87
-1.5	89.31	98.34	82.77

According to the CVs shape (Figure 7.3), current per active material of both the ESW are comparable between each other. Despite the more rectangular shape of anodic ESW, since the energetic efficiency is higher, both CVs have a current peak on the highest potential. However, it is considerably safe to work in that region due to the high coulombic efficiency and the absence of other current peaks, whose causes are mainly related to internal irreversible redox and/or overcharge.

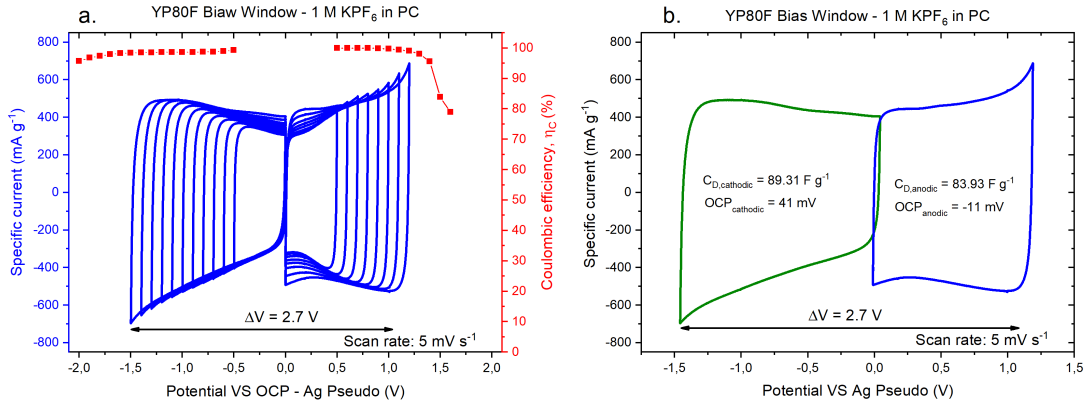

Figure 7.3: AC electrode in 1 M KPF_6 in PC. (*a*) Coupled anodic and cathodic ESW versus OCP w.r.t coulombic efficiency and (*b*) complete ESW including OCP comparison.

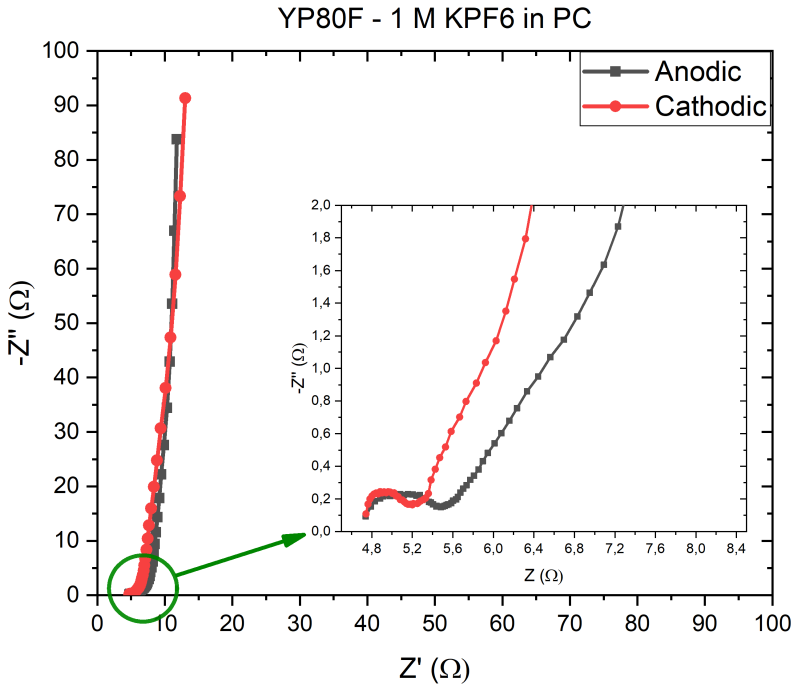

Figure 7.4: Electrochemical impedance spectroscopy of the AC electrode in electrolyte 1 M KPF_6 in PC.

The order of magnitude of OCP in both the cases is comparable, the reason of having positive or negative value can be due to fluctuation of that value during measurements or misalignments in cell assembly. Electrochemical impedance spectroscopy shows the classical EDLC capacitive behaviour (figure 7.4). Both the EIS shows the same Nyquist plot, with a slightly difference in the diffusion region and about lowest frequency imaginary part, which is due to different mass electrode. W.r.t. other impedance spectroscopy[9], the ESR is high. A possible reason of this can be the electrolyte chosen, since usually for AC electrode the common one used is 1 M tetraethylammonium tetrafluoroborate (Et_4NBF_4) in acetonitrile (ACN)[9]. Despite the high resistance value, the energetic efficiency is quite high in all the potential window considered.

Defined the two boundaries, the electrode was tested in the complete ESW with CV measurement, in order to evaluate the stability over an high number of charge/discharge (C/D), which in this test the number chosen was 200. The scan rate was set to 1 mV/s. The coulombic efficiency (Figure 7.5b on left) has settled down to an average value of 98%, which is reasonable since the cathodic efficiency limited the C/D efficiency. Energetic efficiency after an increase to values higher than 80% began to decrease until it reached 70%, which is still high. Specific capacitance (Figure 7.5b on right) showed the biggest increase, since from 86.12 F/g reached 131.78 F/g, which is comparable with the one found in literature[21]. The CV shape still has the two peaks at the boundaries, as expected from individual measures anodic and cathodic, however there was a little current peak at 0.7 V, which can be related to oxygen contamination of the electrolyte.

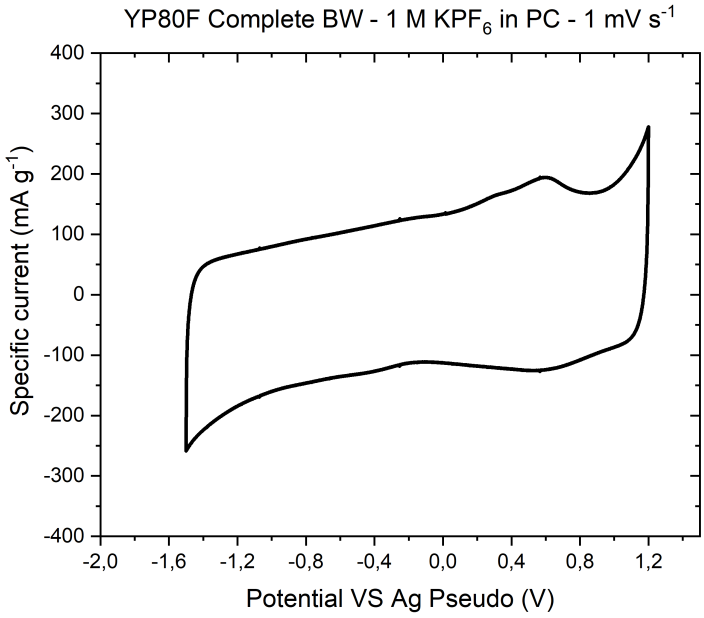

(a)

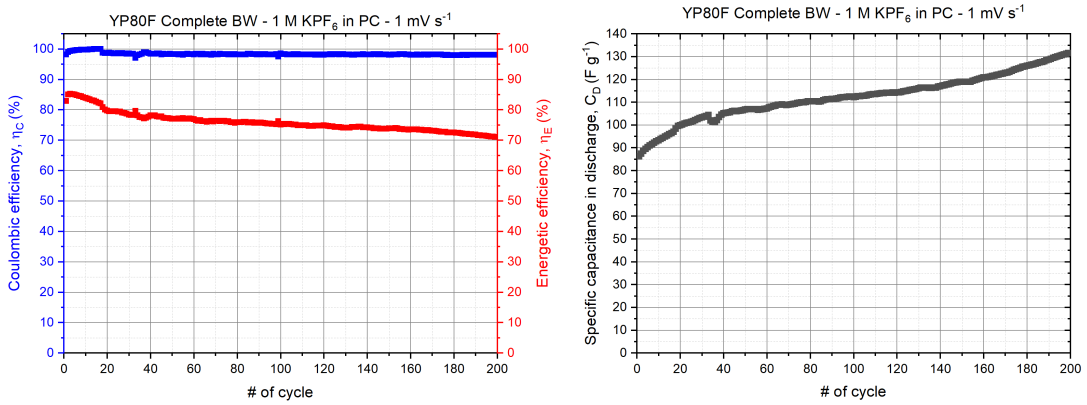

(b)

Figure 7.5: Complete ESW of AC electrode in 1 M KPF_6 in PC. it is reported the cyclic voltammetry (*a*) and the variation of coulombic and energetic efficiency (*b* - **Left**), and specific capacitance in discharge (*b* - **Right**) versus cycle of C/D.

Another measurement made for this electrode was evaluating the CV with different scan rate. The setted rate were 1, 2, 5, 10, 20, 50, 100, 200 and 500 mV/s, in order to have a logarithmic evaluation of the current response. All the CVs, subdivided by the magnitude of the scan rate applied, are showed in Figure 7.7. For the low scan rate the CV shape is unchanged, and the current growth follows a linear trend. When medium scan rate is applied, the influences of parasitic resistance are more evident, since the shape is moving away from that rectangular. With high scan rate, all the charge is mainly lost due to resistance effect, as it is possible to see the oval shape.

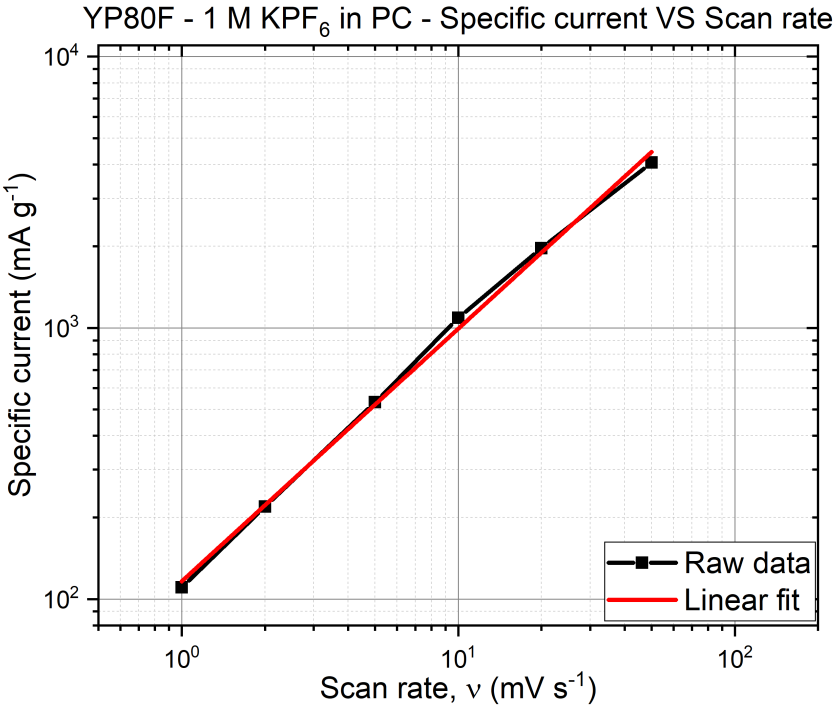

Figure 7.6: Logarithmic plot of the current per active material versus scan rate. Raw data and linear fit are compared.

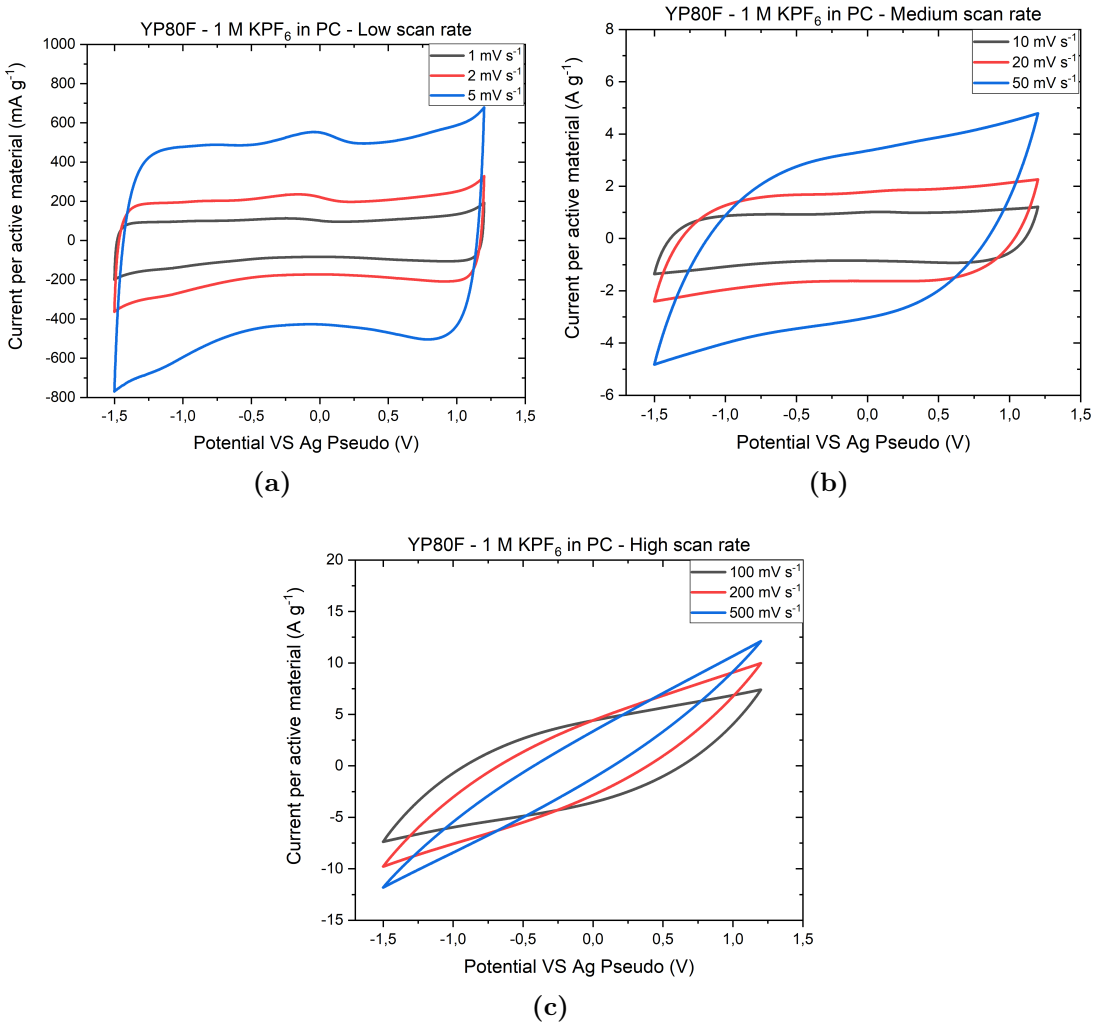

Figure 7.7: CV of AC electrode at different scan rate. The division was made for comparing the magnitude of the current according to the magnitude of the scan rate: (a) Low, (b) Medium and (c) High.

Keeping the analysis of current only for low and medium scan rate, it is possible to evaluate the a and b parameters than define the growth of the current w.r.t the scan rate, using Equation 2.2. This approximation is valid only if the scan rate is kept to that range, while outside that range it is no more valid. The parameter values of a and b are respectively 116.2465 mA/g and 0.93181 a.u.. According to theory, the b obtained is related to a EDLC electrode, which is the one expected. The raw data and the linear approximation is plotted in Figure 7.6.

The specific capacitance found at the lowest scan rate is lower than the one found with the complete ESW analysis. This is due to the lower number of cycle

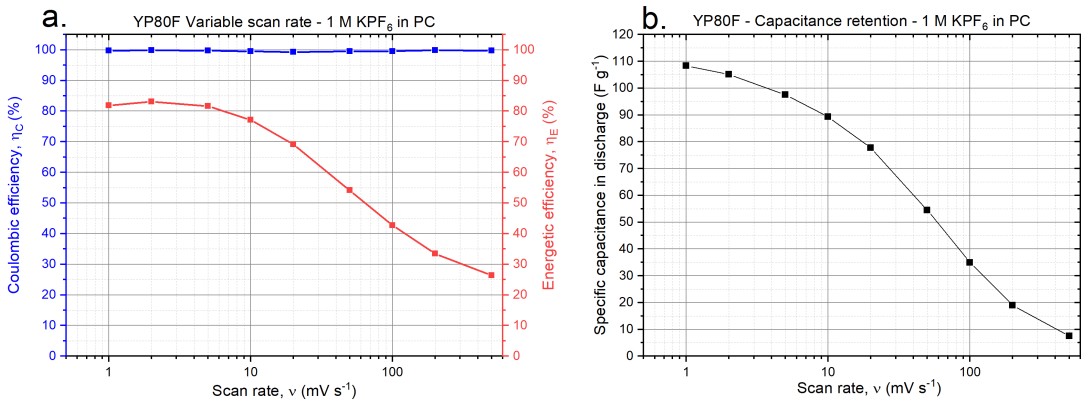

Figure 7.8: (*a*) Capacitance retention, (*b*) coulombic and energetic efficiencies w.r.t. the scan rate.

made in this test w.r.t. the 200 made before. The energetic efficiency shows a drastic decrease starting in the middle scan rate range, which is comparable to the CV shapes evaluated before.

7.1.2 0.8 M KPF_6 in EC:DEC

For the sake of completeness, another electrolyte was investigated, with the same salt but different solvent (ED:DEC). The molar concentration chosen was 0.8 M, which was the maximum reachable for the complete dissolution inside that solvent without precipitation. The choice of that electrolyte was to align with studies already carried out on hybrid k-ion supercapacitor and for a future perspective of combining EDLC electrodes with pseudocapacitive or battery-type ones. Anodic and cathodic measurements are reported in Figures 7.9 and 7.10. With respect to the previous electrolyte, in order to keep coulombic efficiency higher than 99%, the anodic limit was set to 1.1 V, since at 1.2 V the efficiency evaluated was 96%. Again, in cathodic the coulombic efficiency was in the range between 98% and 99%, so for defining the highest potential boundary the limiting parameter chosen was the energetic efficiency. The specific capacitance values at the highest potential window for anodic and cathodic were respectively 88.18 and 80.76 F/g, which are comparable with the previous case.

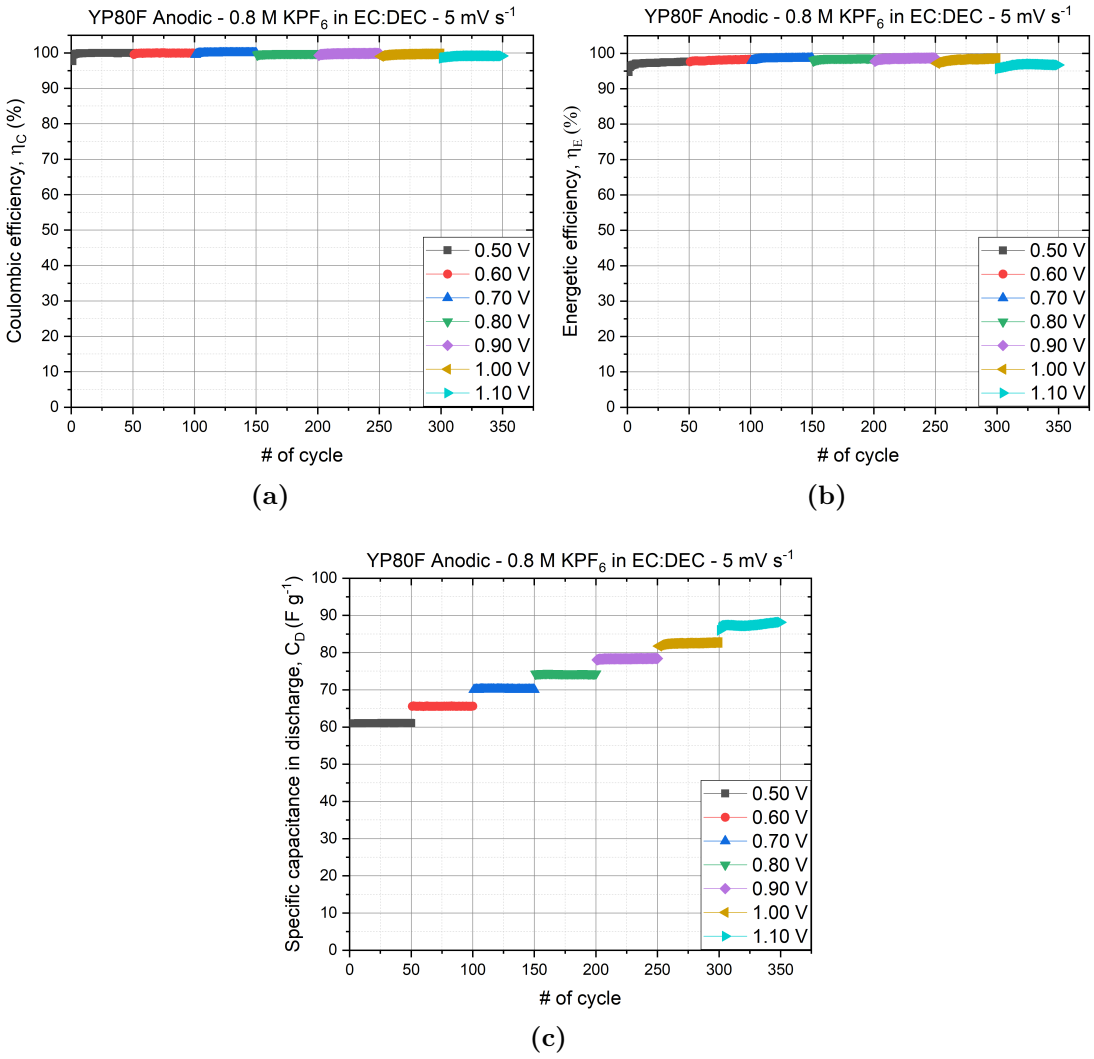

Figure 7.9: AC electrode characterization in anodic potential window in 0.8 M KPF_6 in EC:DEC, separated by each applied potential. For each, there were made 50 cycles. In order: (*a*) Coulombic efficiency; (*b*) Energetic efficiency; (*c*) Specific capacitance in discharge.

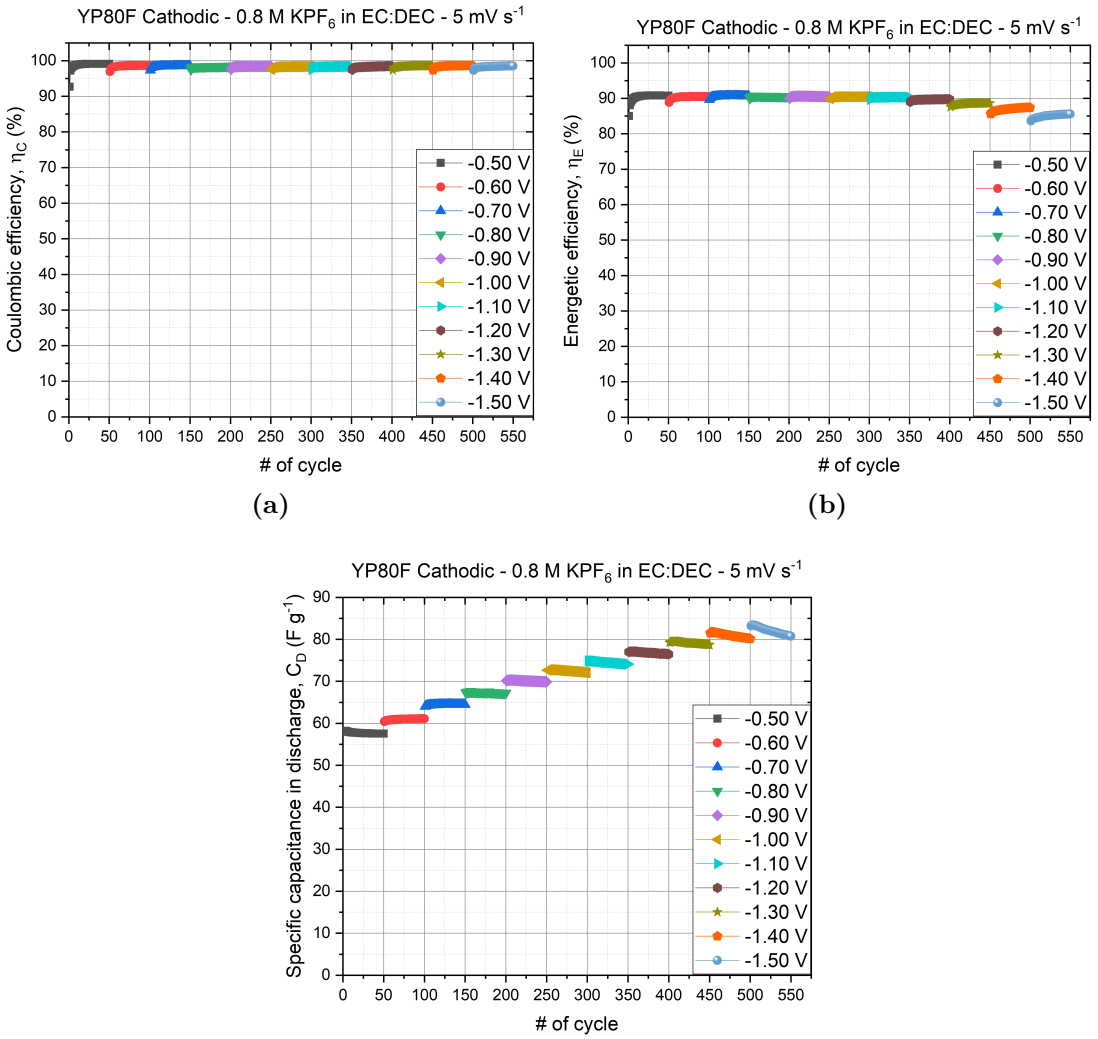

Figure 7.10: AC electrode characterization in cathodic potential window in 0.8 M KPF_6 in EC:DEC, separated by each applied potential. For each, there were made 50 cycles. In order: (*a*) Coulombic efficiency; (*b*) Energetic efficiency; (*c*) Specific capacitance in discharge.

Table 7.3: Evaluated parameters of specific capacitance and efficiencies w.r.t. potential VS OCP of AC electrode, in anodic characterization 0.8 M KPF_6 in EC:DEC.

ΔV VS OCP (V)	**C_D (F/g)**	η_C (%)	η_E (%)
0.5	61.06	99.96	97.70
0.6	65.59	99.90	98.31
0.7	70.03	99.99	98.06
0.8	74.33	99.96	98.67
0.9	78.40	99.88	98.65
1.0	82.71	99.74	98.54
1.1	88.18	99.15	96.70

Table 7.4: Evaluated parameters of specific capacitance and efficiencies w.r.t. potential VS OCP of AC electrode, in cathodic characterization 0.8 M KPF_6 in EC:DEC.

ΔV VS OCP (V)	**C_D (F/g)**	η_C (%)	η_E (%)
-0.5	57.53	99.09	90.76
-0.6	61.08	98.64	90.50
-0.7	64.45	98.52	90.61
-0.8	67.21	98.50	90.55
-0.9	69.90	98.43	90.48
-1.0	72.05	98.39	90.47
-1.1	74.11	98.40	90.34
-1.2	76.44	98.49	86.76
-1.3	78.69	98.55	88.66
-1.4	80.14	98.59	87.40
-1.5	80.76	98.54	85.57

The less rectangular shape of CVs can be explained by an higher ESR and IR of the electrode in this electrolyte, as Figure 7.12 shows. W.r.t. the previous characterization, the resistance are almost the double, and this impedance contribution may be due to a less conductivity of K-ion into the considered solvent. Despite this drawback, current density are comparable with the one evaluated before, and the OCP values are reproducible, with the same consideration made in advance.

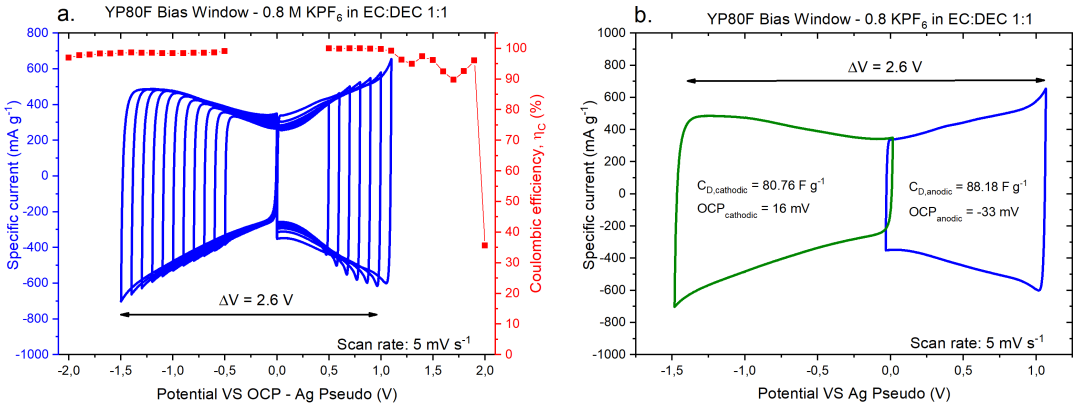

Figure 7.11: AC electrode in 0.8 M KPF_6 in EC:DEC. (*a*) Coupled anodic and cathodic ESW versus OCP w.r.t coulombic efficiency and (*b*) complete ESW including OCP comparison.

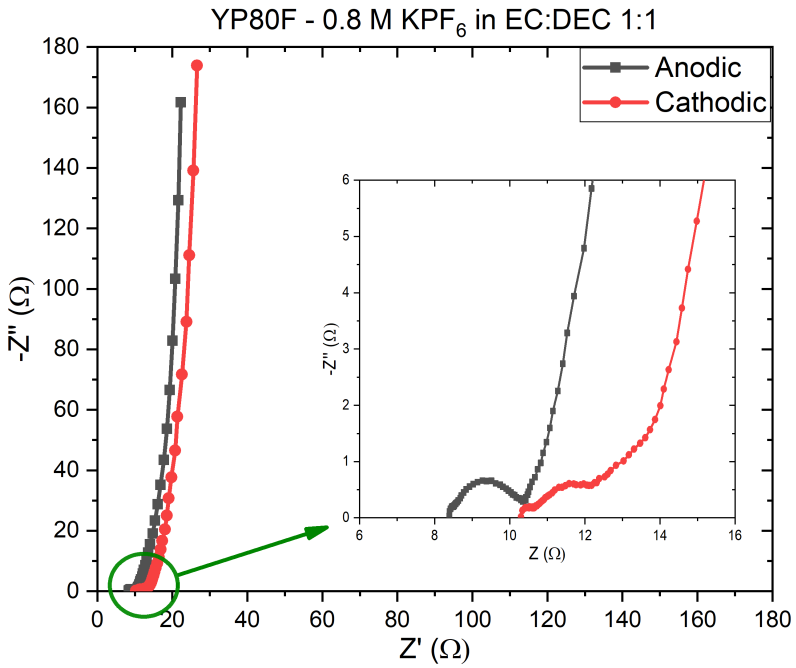

Figure 7.12: Electrochemical impedance spectroscopy of the AC electrode in electrolyte 0.8 M KPF_6 in EC:DEC 1:1

7.2 MnO_2 electrode characterization

Characterization of MnO_2 electrode was made the same as the one done for activated-carbon. According to literature[26], predicted ESW considered stable is in the range between 0 and 1 V versus Ag/AgCl reference electrode[26], so the best suitable configuration for its use is the anodic one, completely disregarding potential negatives. However, to fully typify the hand-made MnO_2 powder, also cathodic measurements were made.

7.2.1 1 M KPF_6 in PC

Despite the initial choice of the use of electrolyte with as solvent the combined EC:DEC, characterization with PC as solvent was also made, in a future matter of comparison. In fact, firstly, tests were performed with the latter electrolyte, since they were made simultaneously with AC characterization. The settings were the same as the one used for the AC electrode, except in the number of cycles, which were lowered to 20 just to provide rapid information. An initial consideration is related to the OCP, which wasn't stable between different measurements of the same electrode, and higher one order of magnitude w.r.t. the one found in Section 7.1 (from 400 mV to nearly 800 mV). A probable pairing with an AC electrode could not be suitable, since the overall OCP of the device isn't stable. In anodic test (Figure 7.13) the maximum potential found was 1.3 V, which is higher than carbon-based electrode, however the coulombic efficiency never reached values higher than 95%, which is the main drawback found during all the measurements made with that electrolyte. In fact, the one at the maximum potential is equal to 92.6%. Despite the good energetic efficiency, the specific capacitance is far away from the values evaluated in carbon-based electrode, 25.25 F/g. For the cathodic one, the highest potential found was -0.5 V, even if the applied potential VS OCP was high, and this was due to the higher value of OCP. In this case coulombic efficiency was higher than 98%, and that result wasn't expected since from theory[27] it should have been destroyed as soon as the potential dropped to negative potentials. However, strange behaviour of energetic efficiency is reported, as it dropped significantly to 40% and started to slightly increase at higher potential.

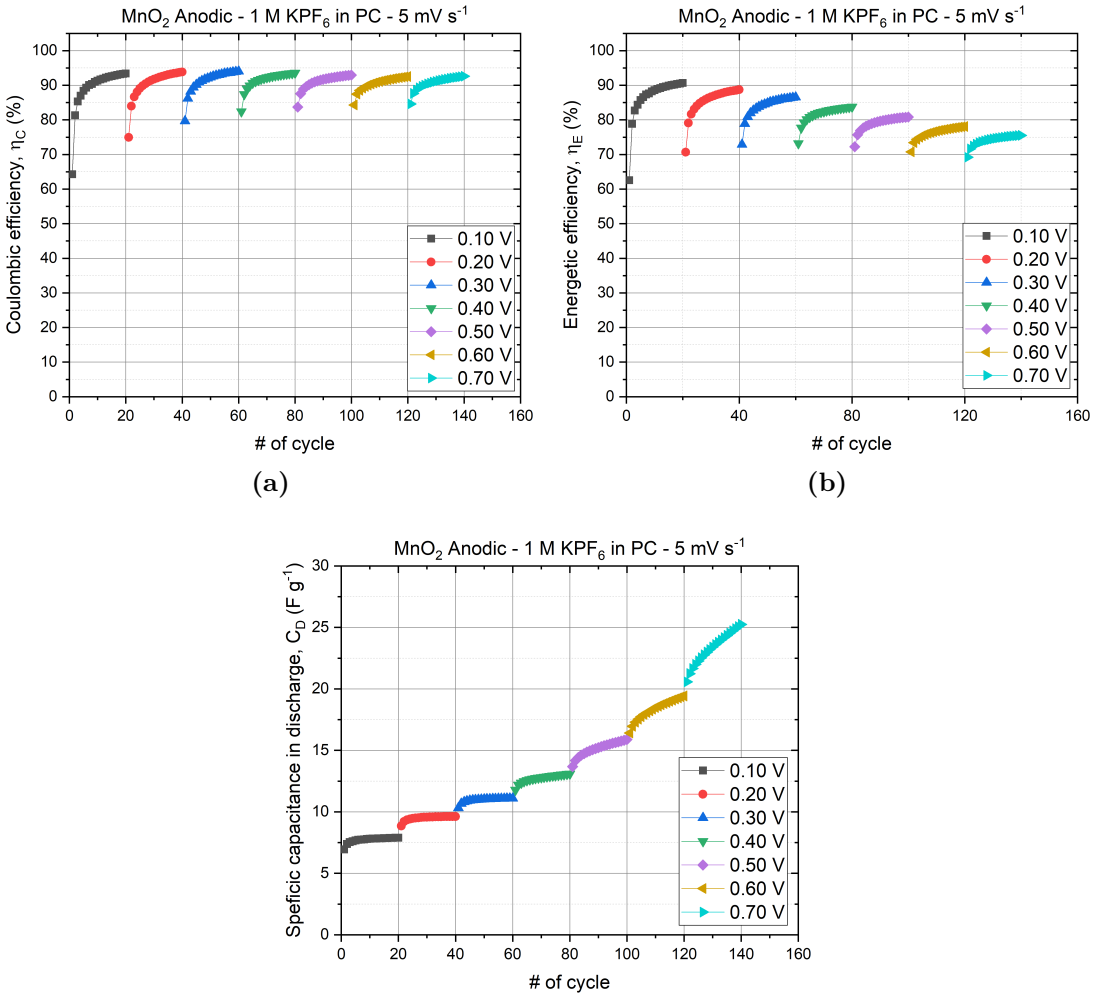

Figure 7.13: MnO_2 electrode characterization in anodic potential window in 1 M KPF_6 in PC, separated by each applied potential. For each, there were made 50 cycles. In order: (*a*) Coulombic efficiency; (*b*) Energetic efficiency; (*c*) Specific capacitance in discharge.

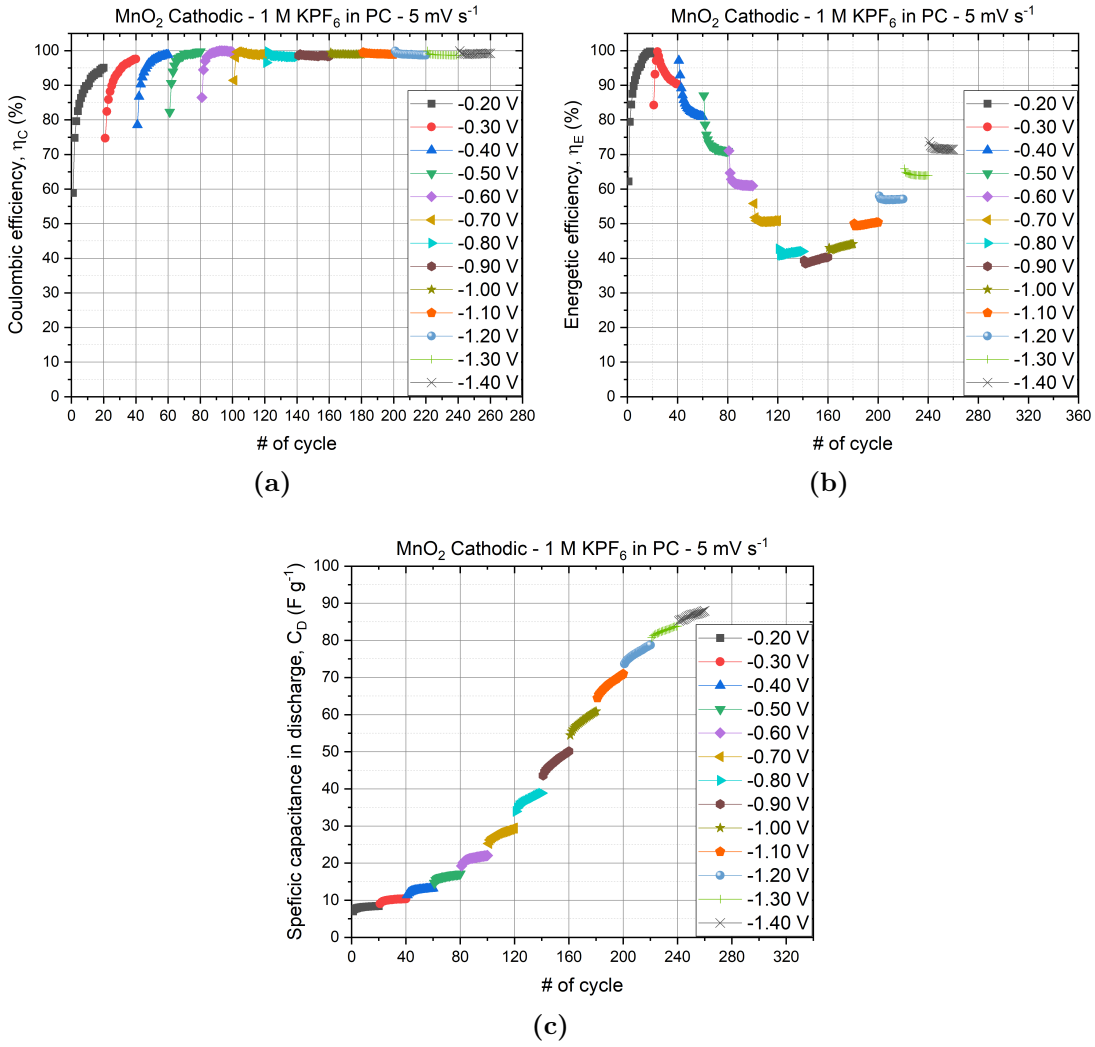

Figure 7.14: MnO_2 electrode characterization in cathodic potential window in 1 M KPF_6 in PC, separated by each applied potential. For each, there were made 50 cycles. In order: (*a*) Coulombic efficiency; (*b*) Energetic efficiency; (*c*) Specific capacitance in discharge.

Table 7.5: Evaluated parameters of specific capacitance and efficiencies w.r.t. potential VS OCP of MnO_2 electrode, in anodic characterization 1 M KPF_6 in PC.

ΔV VS OCP (V)	**C_D (F/g)**	**η_C (%)**	**η_E (%)**
0.1	7.89	93.41	90.64
0.2	9.62	93.84	88.71
0.3	11.10	94.02	86.54
0.4	13.09	93.56	83.74
0.5	15.88	92.56	80.83
0.6	19.42	92.52	78.09
0.7	25.25	92.60	75.52

Table 7.6: Evaluated parameters of specific capacitance and efficiencies w.r.t. potential VS OCP of MnO_2 electrode, in cathodic characterization 1 M KPF_6 in PC.

ΔV VS OCP (V)	**C_D (F/g)**	**η_C (%)**	**η_E (%)**
-0.2	8.42	95.07	99.14
-0.3	10.39	97.61	90.32
-0.4	13.21	98.89	80.90
-0.5	17.13	99.74	70.97
-0.6	22.07	99.65	60.98
-0.7	29.41	98.78	50.92
-0.8	38.85	98.18	42.02
-0.9	50.14	98.37	40.31
-1.0	60.93	98.90	44.16
-1.1	71.00	98.89	50.38
-1.2	78.76	98.69	57.10
-1.3	83.86	98.71	63.96

That behaviour can be explained looking at the CVs in Figure 7.15, where, during discharge, current still kept negative values for a wide range of potential. A possible interpretation of it can be a succession of internal reactions inside the electrode that are sign of future degradation of electrode.

Specific capacitance followed a non-linear increase in intensity up to 83.86 F/g. The reason of that non-linearity is due to the choice of the cycles number, which was too low to provide good settlement.

Electrochemical impedance showed classical pseudocapacitive behaviour. The tilted diffusion line demonstrated the presence of internal redox that happen at lower frequency, which is usual in a pseudocapacitive electrode. Also, the intensity

in terms of real and imaginary parts of the high frequency semicircle can be attributed to the intensity of internal charge transfer.

Since from the anodic/cathodic characterizations results were beyond expectations, a complete ESW with the boundaries found before was tested. Again, scan rate was scaled down to 1 mV/s to avoid resistance contribution, which in this case was also higher than the AC case. Figure 7.17 reports the results of this measurement. Despite a little increase in specific capacitance, after few cycles the electrode started a rapid degradation until complete destruction. From the first cycles it was possible to predict the electrode malfunction in this ESW just evaluating the coulombic and energetic efficiencies. Even reducing the potential window, while keeping it in the range of negative values, didn't provide stability over tens of cycles. This confirmed the instability of this particular electrode for negative potential, so further consideration in the complete ESW were made only in the positive range of potential.

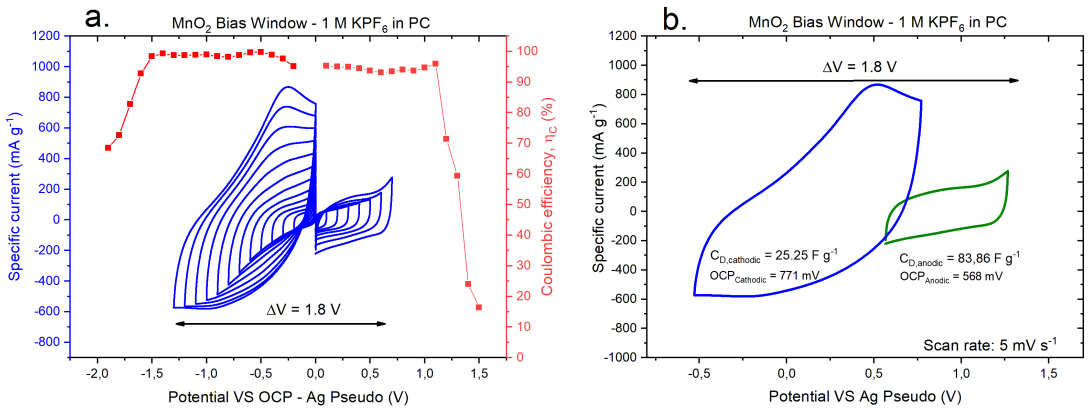

Figure 7.15: MnO_2 electrode in 1 M KPF_6 in PC. (*a*) Coupled anodic and cathodic ESW versus OCP w.r.t coulombic efficiency and (*b*) complete ESW including OCP comparison (**Right**). The OCPs reported are the one for the measurement made, but its value was unstable between different tests made.

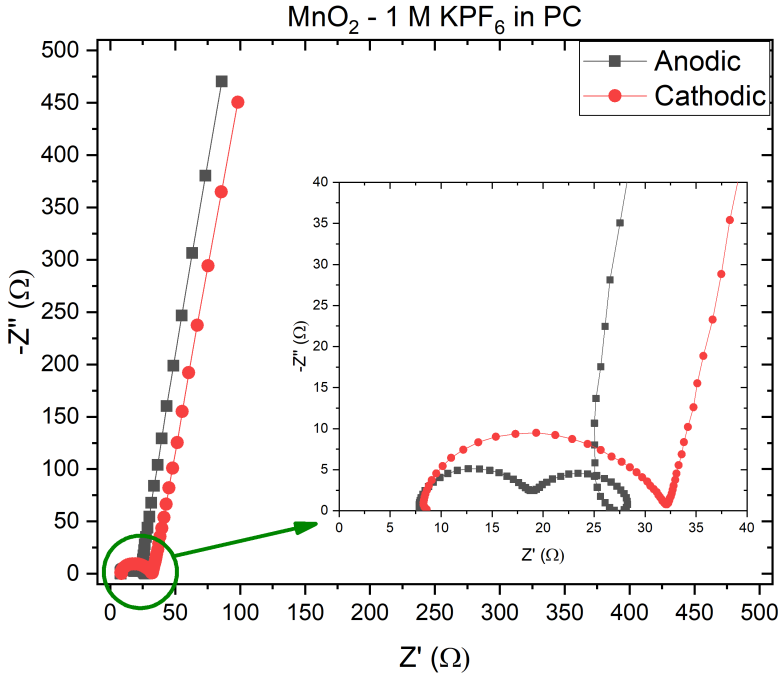

Figure 7.16: Electrochemical impedance spectroscopy of the electrode in electrolyte 1 M KPF_6 in PC.

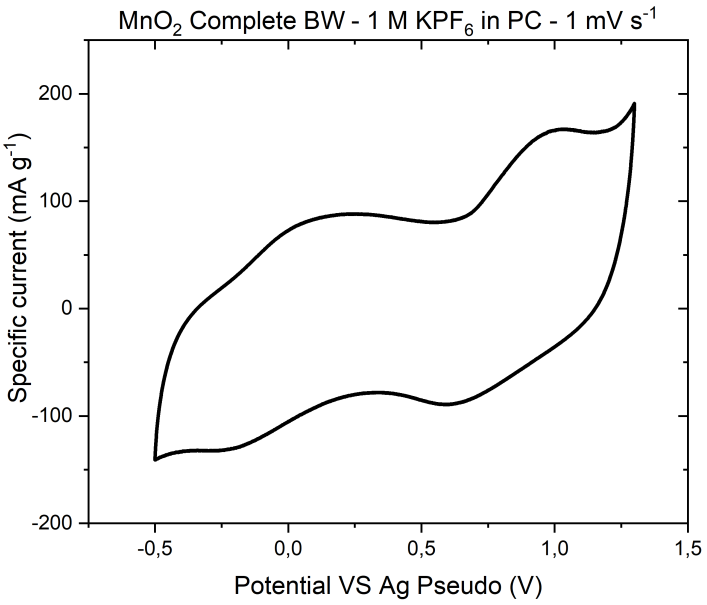

(a)

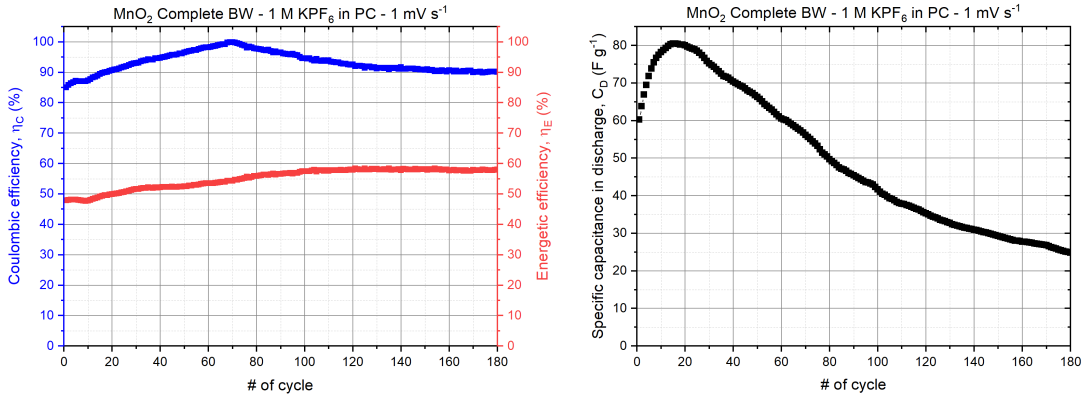

(b)

Figure 7.17: Complete ESW of MnO_2 electrode in 1 M KPF_6 in PC. it is reported the best cyclic voltammetry (*a*) and the variation of coulombic and energetic efficiency (*b* - **Left**), and specific capacitance in discharge (*b* - **Right**) versus cycle of C/D.

7.2.2 0.8 M KPF_6 in EC:DEC

Moving forward to the analysis, MnO_2-based electrode was tested in the electrolyte with EC:DEC as solvent. Since from previous measurements low cycles number didn't provide a stable value of most of the parameters, its quantity was again increased to 50. W.r.t. the previous electrolyte, the OCP found was stable to values near to 400 mV and repetitive among different measurements, which are good factors even if a possible coupling with a AC electrode still provide hundreds of mV of OCP. In all the anodic potential till the maximum found, whose value found was again 1.3 V, the coulombic efficiency never reached completely values higher than 99% but was kept to a range higher than 95%, which for this electrode was the lower limit, despite the initial condition imposed. Similar behaviour was found for all the cathodic potential investigated, where its maximum value found was reduced to -0.3 V. Specific capacitance in anodic increased to a maximum of 44.49 F/g, almost the double of the previous electrolyte, while in cathodic decreased up to 55.09 F/g. The reason of convergence found in their values must be found in the quasi-symmetric potential applied w.r.t the OCP, since in the previous electrolyte the cathodic window was favoured by a wider range of potential. A note of merit must be said about the stability over the cycles, which, due to the increased number of cycles, is confirmed. The unusual trend of energetic efficiency was found again, in less intensity, and the reasons for this are again to be found in the shapes of the CVs, the non-regularity of which is due to the larger contributions of parasitic resistances, with an extra focus on the current peaks, which are not perfectly symmetrical with each other.

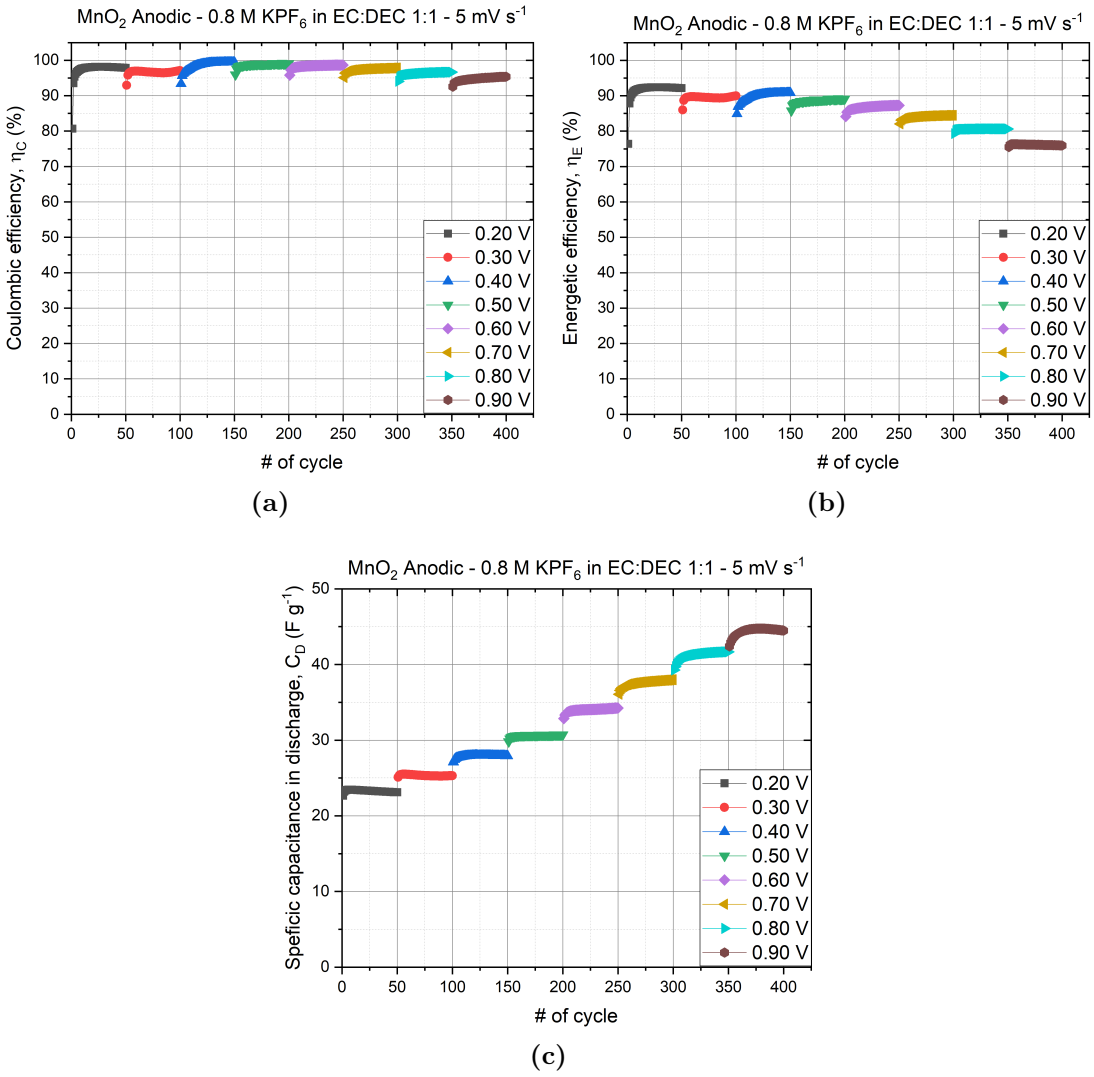

Figure 7.18: MnO_2 electrode characterization in anodic potential window in 0.8 M KPF_6 in EC:DEC, separated by each applied potential. For each, there were made 50 cycles. In order: (*a*) Coulombic efficiency; (*b*) Energetic efficiency; (*c*) Specific capacitance in discharge.

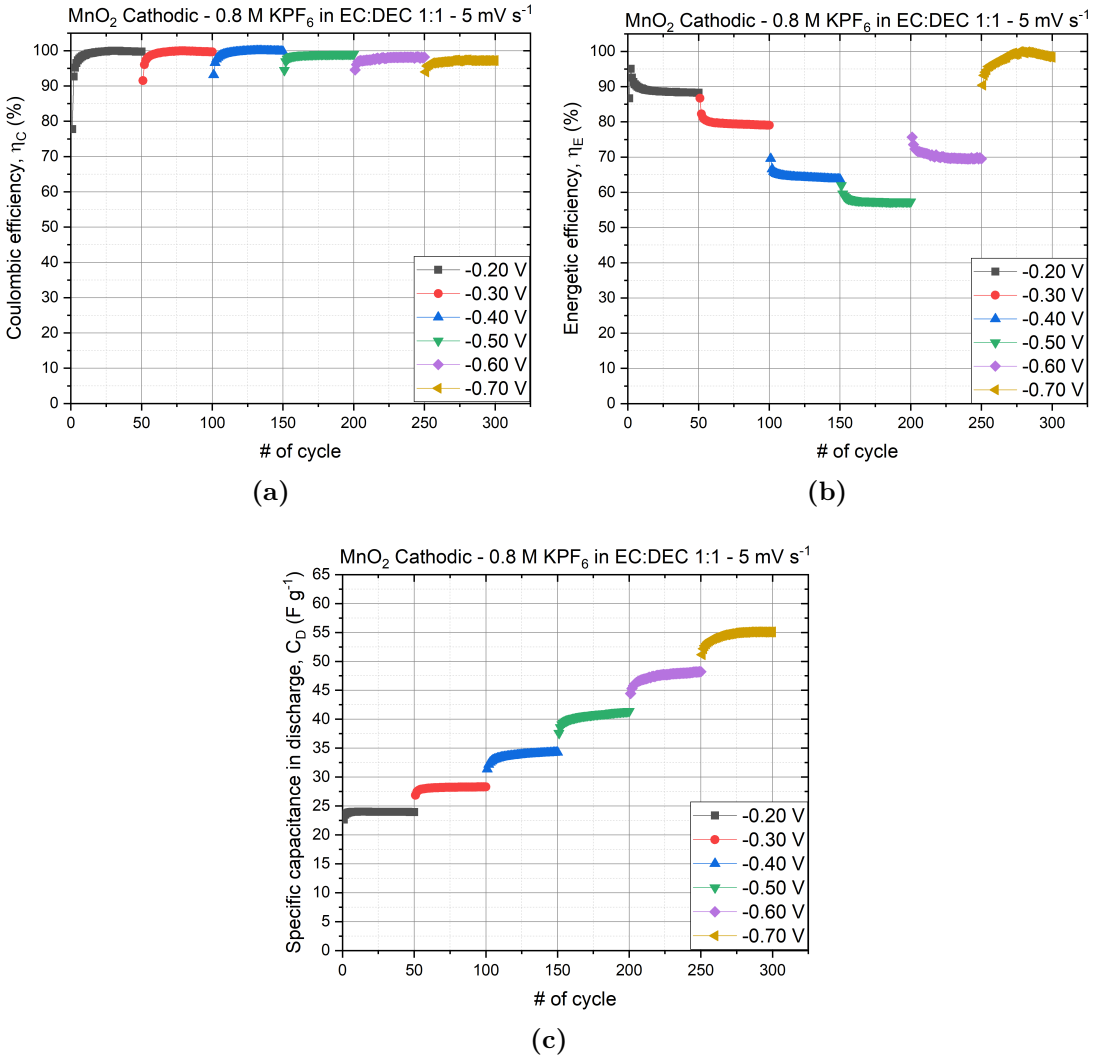

Figure 7.19: MnO_2 electrode characterization in cathodic potential window in 0.8 M KPF_6 in EC:DEC, separated by each applied potential. For each, there were made 50 cycles. In order: (*a*) Coulombic efficiency; (*b*) Energetic efficiency; (*c*) Specific capacitance in discharge.

Table 7.7: Evaluated parameters of specific capacitance and efficiencies w.r.t. potential VS OCP of MnO_2 electrode, in anodic characterization 0.8 M KPF_6 in EC:DEC.

ΔV VS OCP (V)	C_D (F/g)	η_C (%)	η_E (%)
0.2	23.10	97.84	92.14
0.3	25.31	97.11	89.97
0.4	27.93	99.48	90.84
0.5	30.74	990.80	89.11
0.6	34.24	98.66	87.30
0.7	37.99	97.83	84.47
0.8	41.66	96.64	80.61
0.9	44.49	95.36	75.94

Table 7.8: Evaluated parameters of specific capacitance and efficiencies w.r.t. potential VS OCP of MnO_2 electrode, in cathodic characterization 0.8 M KPF_6 in EC:DEC.

ΔV VS OCP (V)	C_D (F/g)	η_C (%)	η_E (%)
-0.2	23.95	99.75	88.27
-0.3	28.29	99.67	79.03
-0.4	34.29	99.82	63.74
-0.5	41.36	99.06	57.32
-0.6	48.21	98.20	69.52
-0.7	55.09	97.21	98.33

W.r.t the EIS made before, the ESR are comparable while the IR showed a reduction of almost 40% of its value. The high fluctuations found in ESR evaluation may be due to a non conform electrode sample, because the probability to get it when small sample are considered is higher. As before, titled diffusion line and more marked high frequency semicircle are characteristic of these Nyquist plots in that electrolyte.

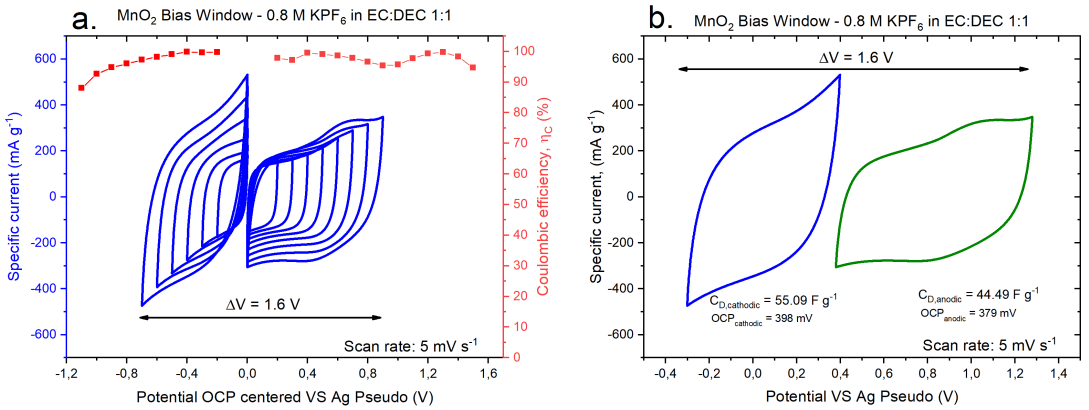

Figure 7.20: MnO_2 electrode in 0.8 M KPF_6 in EC:DEC. (*a*) Coupled anodic and cathodic ESW versus OCP w.r.t coulombic efficiency and (*b*) complete ESW including OCP comparison (**Right**).

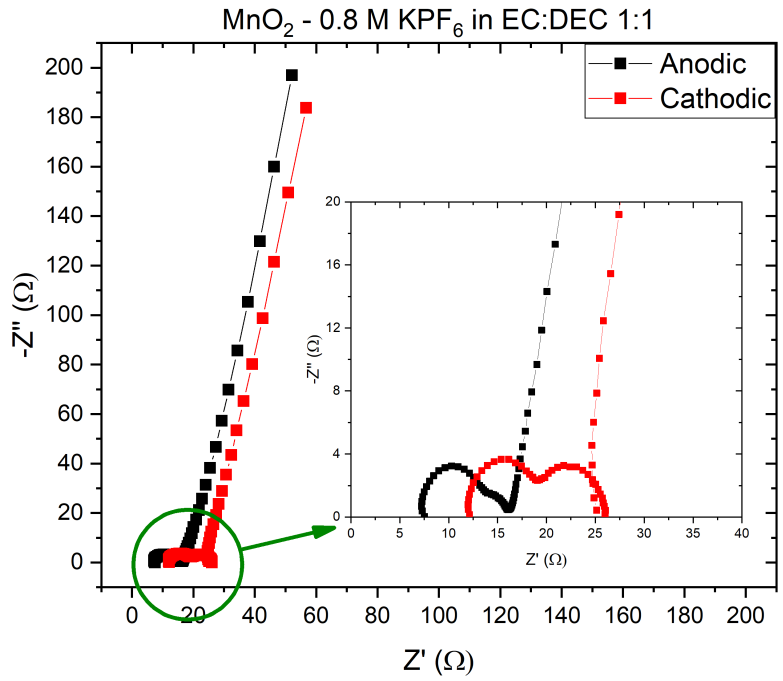

Figure 7.21: Electrochemical impedance spectroscopy of the electrode in electrolyte 1 M KPF_6 in EC:DEC 1:1.

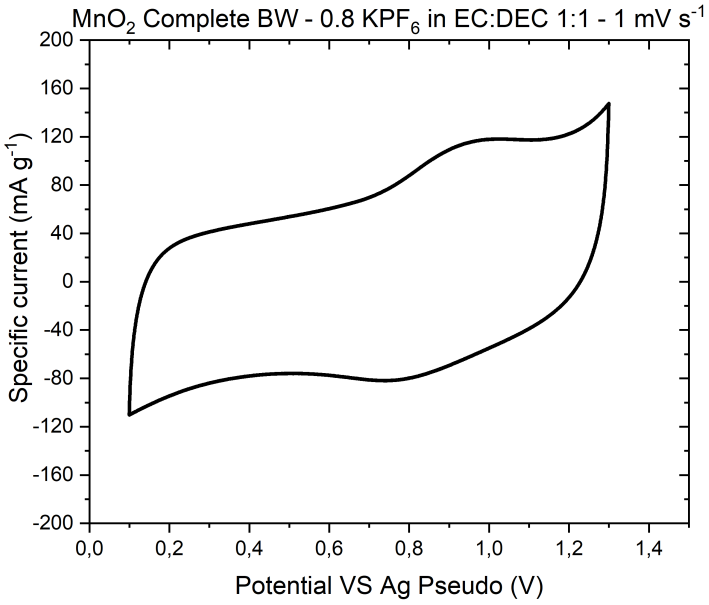

(a)

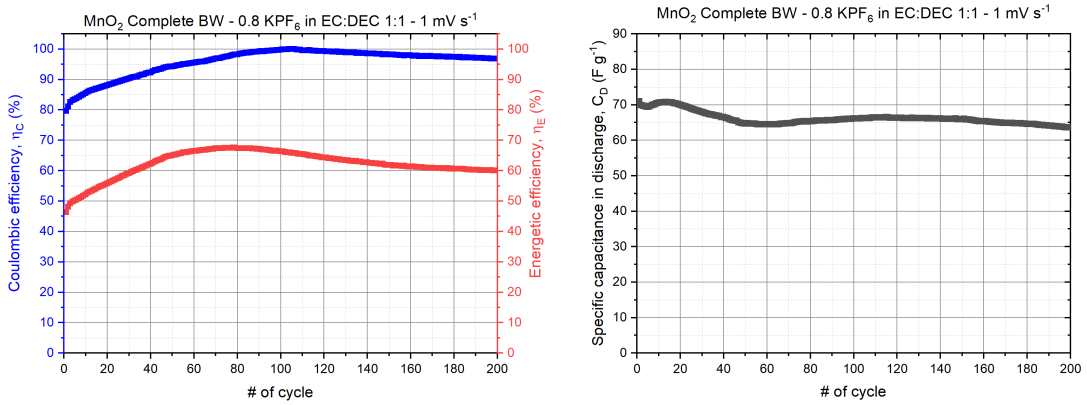

(b)

Figure 7.22: Complete ESW of MnO_2 electrode in 0.8 M KPF_6 in EC:DEC. it is reported the cyclic voltammetry (*a*) and the variation of coulombic and energetic efficiency (*b* - **Left**), and specific capacitance in discharge (*b* - **Right**) versus cycle of charge/discharge

Knowing from the last complete ESW test that widing the window to negative potential can lead to a degradation of the electrode, for that case the potential were limited only in the positive range. A cyclic stability measurement was made keeping the boundaries between the maximum found in anodic and 0.1 V, which,

according to the cathodic characterization, provided good coulombic and energetic efficiencies. The results plotted in Figure 7.22 show a nice stability over cycles, in which the capacitance retention was limited to 90%. The CV shape is mainly attributable to the anodic contribution, as expected, with a marked peak current at the lower limit.

Confirmed that the best electrolyte for this electrode is 0.8 M KPF_6 in EC:DEC, a possible asymmetric configuration with AC electrode is showed in Figure 7.23, in which the MnO_2 is fixed in anodic to a maximum of 1.3 V, while the AC one to a minimum of -1.5 V, so an overall voltage range of 2.8 V, slightly higher w.r.t. the symmetric AC/AC 2.7 V.

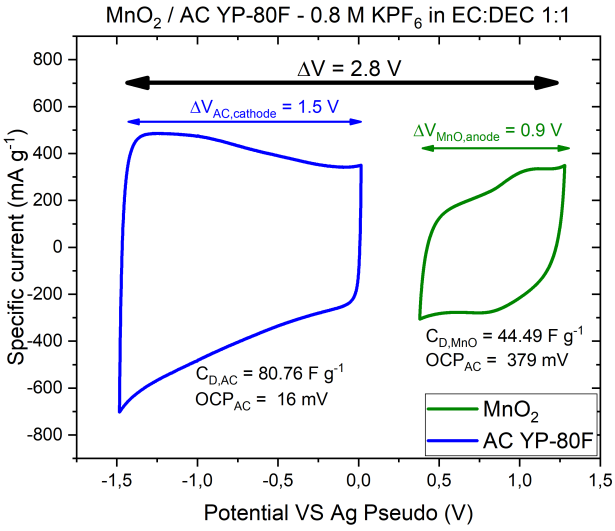

Figure 7.23: Asymmetric configuration between MnO_2 and AC electrodes, w.r.t. their OCP.

7.3 Carbon-black electrode characterization

The reason for choosing this material for the battery-type electrode is due to its simplicity in electrode production, its availability and possible scalability. According to recent studies[28], its properties in a potassium ion battery (PIB) system are promising, with the future prospect of their use in large-scale devices. One of the challenges that unites electrode employed in PIB is defining the kinetics of intercalation/deintercalation reactions of K-ion into the structure of the electrode, which usually cause huge volume expansion that destroys its integrity[28].

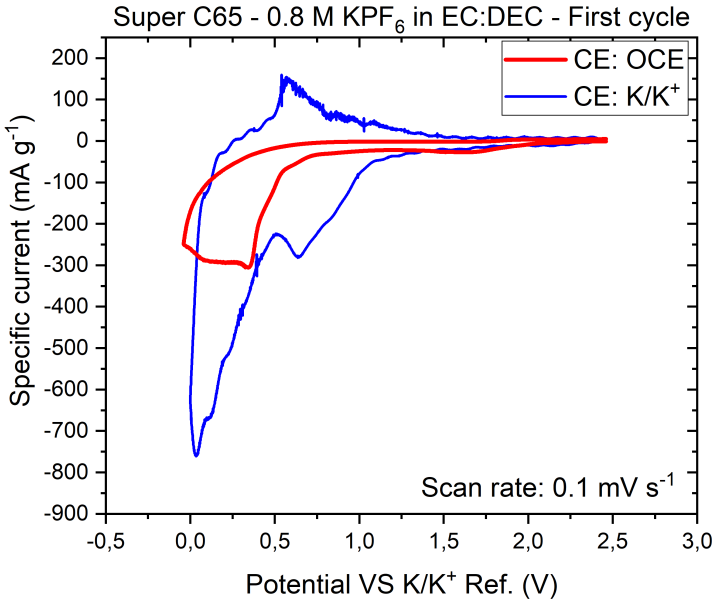

Figure 7.24: First CV cycle, in which in **Red** the CE used is OCE, mostly used in this thesis, while in **Blue** the CE used was a Potassium disc.

Since, from the previous characterization, this topic was never take into account, as it wasn't needed, a first try in characterize it was done using the same configuration made with the other electrodes. The CE used was always OCE and the reference was Ag Pseudo. The scan rate was set to the lowest value possible, in this case 0.1 mV/s, in order to enhance the intercalation process. Given the absence of a sacrificial potassium source, which usually is a potassium disc fixed as the CE, the first CV cycle provided a small intercalation sign when it reached 0 V VS K/K^+, but the deintercalation step has never been achieved. Due to the lack of the latter, the amount of K-ion inside the electrolyte reduced dramatically after the very first cycles of intercalation and the subsequent cycles provided always lower current and smaller CV shape. Also, the current intensity was mainly negative in

most of the potential range.

Convinced that this system would never work, the same measurement was repeated using a K source for both CE and Ref. Figure 7.25 reports the significant CV cycle of this test. In the first cycle it is noted a peak in current between 0.4 V to 1.0 V, mainly attributed to the formation of a solid electrolyte interphase (SEI)[28], while the highest peak reached between 0 V and 0.45 V is due to ion intercalation onto the substrate. The reduction of these two peaks can be attributed to the greater difficulty of intercalating other ions and a greater contribution of SEI. The current fluctuations in the various cycles can be attributed to contamination of the cell by the kerosene present in the potassium disc.

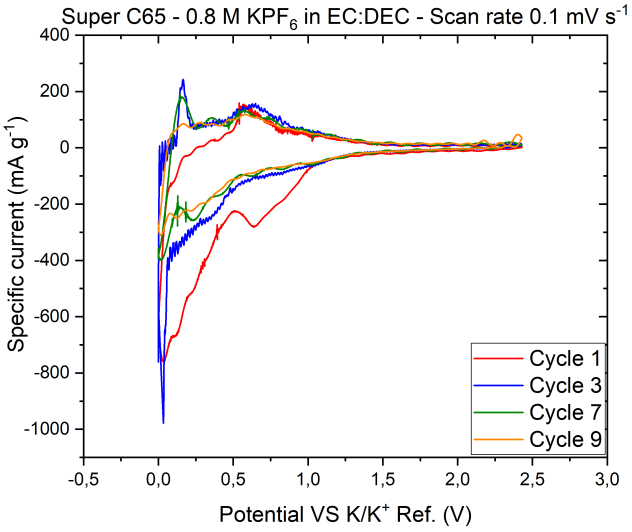

Figure 7.25: Significant CVs of the Super C65 electrode with K/K^+ as Ref. and CE.

Nyquist plots of both the system considered are reported in Figure 7.26. The not perfect straight diffusion line of the K/K^+ case is mostly related to contamination previously cited. In fact, the ESR found for the two cases and the estimated specific capacitance using the last imaginary part value were comparable between each other.

From the CV, it was possible to quantify the specific capacity, or the equivalent capacitance, for each cycle. Even if the mass loading provided by the electrode was the lowest w.r.t. the others (0.53 mg/cm^2), the obtained values were higher than the ones found for the AC and MnO_2 electrode. Despite the promising values, efficiencies still remain the main drawback, as for the coulombic efficiency values never reached 99 %.

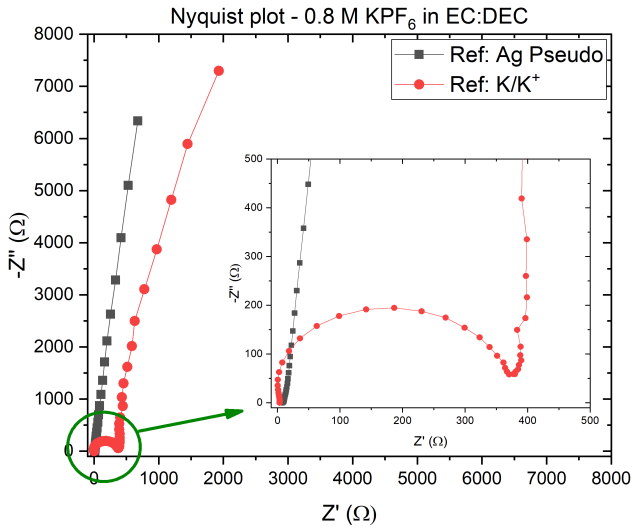

Figure 7.26: Nyquist plot of two cells, in which the reference used was different.

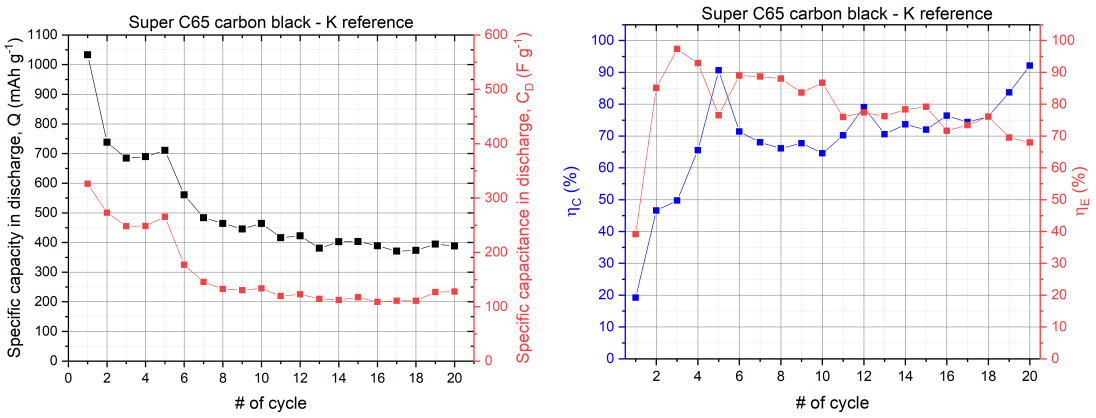

(a) **(b)**

Figure 7.27: Evaluation, related to Super C65 electrode, of characterization parameters. In order: (*a*) Specific capacity and capacitance in discharge w.r.t cycles of C/D; *b*) Coulombic and energetic efficiency w.r.t cycles of C/D.

Finally, it is reported the CV comparison between Super C65 and AC electrode in Figure 7.28. The EDLC region of CB, defined between 1.0 V and 2.5 V, is an order of magnitude much lower than that of the AC. In an hybrid configuration, the CB electrode is expected to accumulated an higher level of charge, increasing the energy density, while the AC one will provide that amount of charge quickly,

so provide an higher power density.

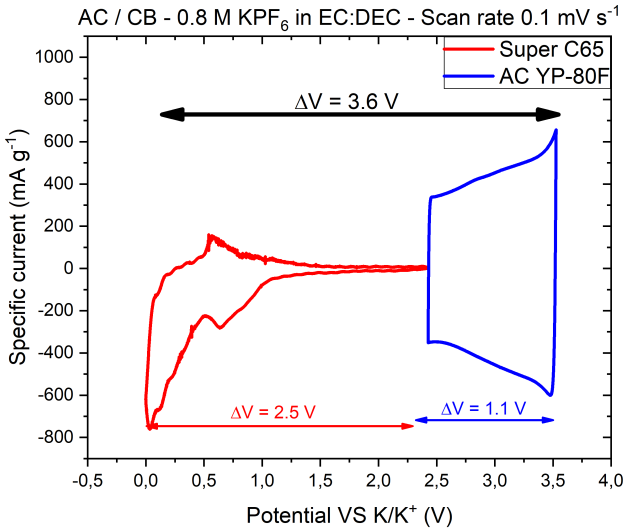

Figure 7.28: AC and Super C65 electrodes in comparison w.r.t. their OCP VS K/K^+.

Chapter 8

Device characterization

8.1 Separator

A crucial component for assembling the final device is the separator. They are characterised by different parameters such as thickness, porosity, density, and resistance to heat and stress. In this thesis were investigated two different type of separator from two different providers: Celgard® 3501 monolayer microporous membrane and NKK® TF40xx cellulose membrane. They differ in the type of material used, so as in the overall features they can provide. From the TF40xx series, were considered two separator, TF4030 and TF4050, whose main difference is the thickness. In Table 8.1 are reported the properties of these separator.

Table 8.1: Information about the separator used.

Separator	**Thickness μm**	**Density g/cm^3**	**Porosity %**	**Material type**
TF4030	30	0.40	73	Cellulose
TF4050	50	0.40	73	Cellulose
Celgard3501	25	/	55	Plastic

In order to evaluate the most suitable separator for the devices under study, were made 3 symmetric devices AC/AC for each separator and tested with variable scan rate cyclic voltammetry. The voltage range was set up to 2.0 V, while the scan rate was set in a logarithmic scale. For further analysis of the impedance, EIS measurement was also made. Only for this purpose, no charge balance was made, so the mass of both the electrodes were the same. Table 8.2 reports the correlation between code device and separator used.

Ragone plot with all the devices is reported in Figure 8.1. From the results obtained, the Celgard 3501 and TF4030 seem to be the best for this device, even if the TF4030 provided higher values of energy and power density, while the TF4050

Table 8.2: Correlation between code used for the devices and the separator used. The letter X indicates the number of the device.

Code	Separator
Y1X	TF4030
Y2X	TF4050
Y3X	Celgard 3501

case seems to have an higher resistance contribution, since the energy density drastically drops for higher power density. Also, repeatability is confirmed for the two first separator, even if the more stable among all the tests was the Celgard 3501 one.

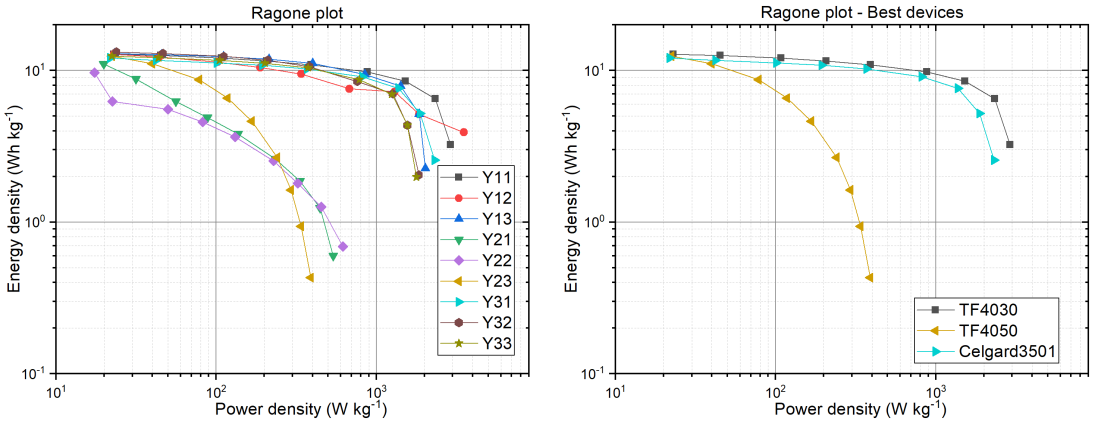

Figure 8.1: Ragone plot of all the devices (**Left**) and the best for each type (**Right**).

The choice of the most suitable one therefore falls on impedance spectroscopy, since by analysing the Nyquist plot it's possible to determine all the resistance contribution. Figure 8.2 shows the Nyquist plot of all the best devices. The diffusion line of the TF4050 case is the one with the highest titled angle w.r.t. the other cases, leading to an higher IR for the device, and this is also correlated to the reason of its bad performance among all the scan rate. Celgard 3501 case has the lowest resistance contribution w.r.t. the TF4030 one. However, the most pronounced high frequency semicircle can be a drawback in the overall performance of it.

Although the results seem to report the TF4030 as the best of all, the repetitiveness of the results among the various devices in the same category has led to a reassessment of the situation. Table 8.3 reports all the ESR and IR evaluated during EIS of all the devices. As it shows, Celgard 3501 was the one that provided

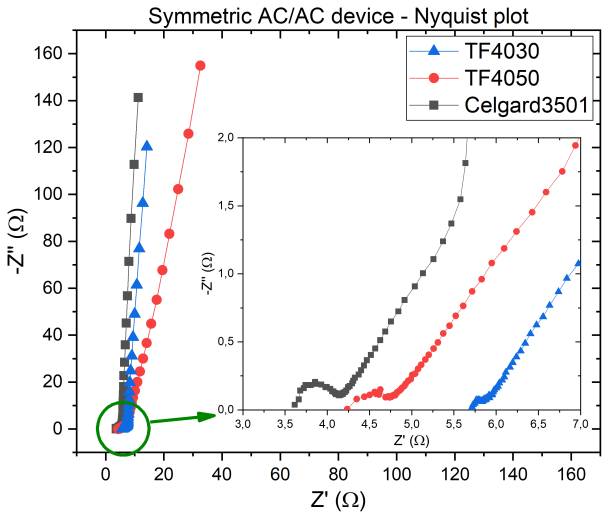

Figure 8.2: Nyquist plot of the best devices for each separator category.

similar values among the measurements, while for the cellulose case fluctuation of all the values was too high to be consider negligible. So, despite the better performance of a single device with TF4030, it was selected the Celgard 3501, since it provided repeatability among all the measurements.

Table 8.3: Evaluated ESR and IR of all the devices.

Code	ESR	IR
Y11	5.7	14.1
Y12	22.6	33.8
Y13	25.4	31.1
Y21	8.1	53.0
Y22	10.60	61.1
Y23	4.2	32.6
Y31	3.6	11.2
Y32	4.4	11.0
Y33	4.1	9.6

To conclude, Figure 8.3 reports the variation of energetic efficiency among the scan rate applied and capacitance retention of the device.

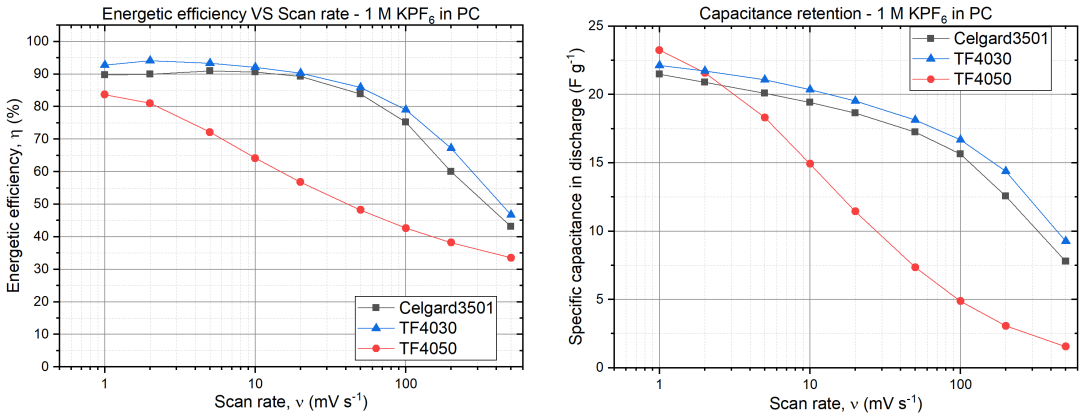

Figure 8.3: Variation of energetic efficiency (**Left**) w.r.t scan rate. Capacitance retention of the device (**Right**).

8.2 Symmetric AC/AC device

8.2.1 Setup

Before analysing the results, a note of merit must be said about the choice of the electrodes for the final device. Symmetric electrode with the same applied potential charge and discharge with the same quantity. However, to reach the maximum ESW with the same electrodes, an imbalance occurs in the accumulated charges in both, in which the one with the lower charge takes precedence. To overcome this disadvantage and exploit the entire ESW, a charge balancing must be carried out. In order to provide that balancing, the following equation must be valid:

$$Q_+ = Q_- \tag{8.1}$$

where Q_+ and Q_- are the charge of the anode and cathode electrodes. Knowing the relationship between charge and voltage in a ideal capacitor:

$$m_+ \cdot V_+ \cdot C_+ = m_- \cdot V_- \cdot C_- \tag{8.2}$$

in which the V contribution is the potential applied w.r.t. OCP, C is the specific capacitance and m is the corresponding active mass of the electrode. Wanting to respect equality, the ratio between the masses is calculated as:

$$\Pi_+ = \frac{m_+}{m_-} = \frac{V_- \cdot C_-}{V_+ \cdot C_+} \tag{8.3}$$

Since the specific capacitance and the maximum potential are known for electrode characterization, the ratio evaluated defines how many times the positive electrode

(anode) must be bigger/smaller w.r.t. the negative one (cathode).

For the symmetric device AC/AC with as electrolyte 1 M KPF_6 in PC, taking the values obtained during characterization, the mass ratio found was:

$$\Pi_+ = \frac{m_+}{m_-} = \frac{1.5V \cdot 89.31F/g}{1.2V \cdot 83.93F/g} = 1.33 \tag{8.4}$$

Keeping in mind the tolerance evaluated during the coating step, it's not necessary to do two different coating for getting two electrodes with that mass ratio. The overall specific capacitance is evaluated as the half of the parallel between the two values:

$$C_{device} = \frac{C_+ // C_-}{2} \tag{8.5}$$

which in this case provides final value of 21.63 F/g. In comparison with the one evaluated for symmetric device without charge balancing, it's comparable, leading to the statement that for these devices charge balancing is not so required. The final voltage applied to the device will be 2.7 V.

8.2.2 Small device

From the first characterization of the device, through activation cycles (Figure 8.4), the CV shape presents an higher current peak at the highest voltage applied. Its intensity drops after few cycles, as a matter of internal settlement of charge distribution, until it fixed up to 200 mA/g. Nyquist plot is comparable with the one found during the separator analysis, even if the ESR and IR are almost completely different, since the first showed a slightly lower value, while the IR almost double its intensity.

The device was then tested with GCD in different current rate. The range selected was 0.1, 0.2, 0.5, 1.0, 2.0 A/g. After all these current, the last rate applied was again 0.1 A/g in order to evaluate the capacitance retention of the device. Variation of GCD at different current rate is shown in figure 8.5.

The almost perfect triangular shapes are those expected, since the nature of the device is completely EDLC. The iR-drop in all the rate were respectively 14.03, 54.73, 140.82, 151.20 and 295.57 mV. Their variations seem not to follow a particular trend, as is the case with charge and discharge time. Coulombic efficiency reached a maximum of 96 % for the lowest current rate, which is still expected since it's limited by the cathodic ESW, but for the highest current rate the efficiency was stable to values higher than 99 %. For the specific capacitance, from the initial rate it reached 22.92 F/g, which is higher than the one expected, while going up with the current it drops to 18.63, with a capacitance retention of 81.3 %. Returning to

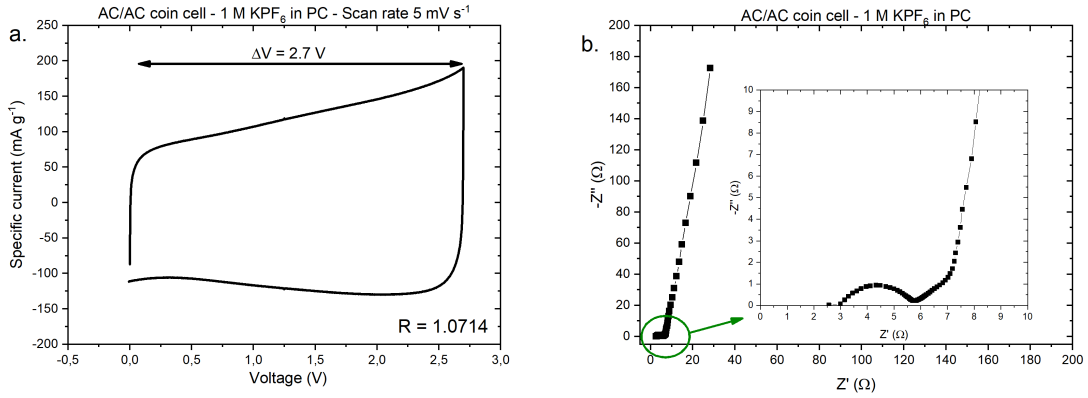

Figure 8.4: AC/AC coin cell device. (a) CV from activation cycles and (b) Nyquist plot.

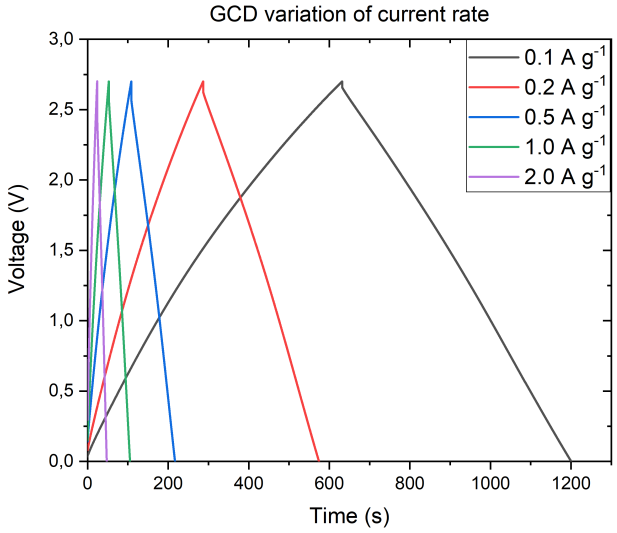

Figure 8.5: GCD of the AC/AC coin cell device at different current rate.

the lower current rate, the value stabilised at 22.55 F/g, with a final retention of 98.4 %, almost negligible.

According to the Ragone plot in Figure 8.7, energy density reached a maximum up to 25 Wh/kg with 138.7 W/kg as power density, while it drops to 16.75 Wh/kg increasing power up to 2.55 kW/kg. Those values are comparable with the one found in literature[29] regarding the symmetric AC/AC EDLC device. However, it wasn't found something similar to this device, so the comparison is just a matter of order of magnitude.

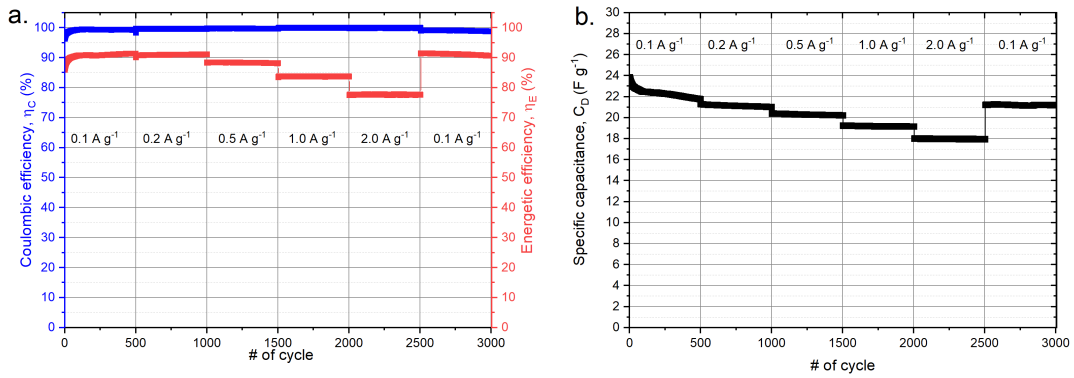

Figure 8.6: AC/AC coin cell device. (*a*) Variation of coulombic and energetic efficiencies w.r.t current rate and cycles. (*b*) Capacitance retention of the device with different current rate.

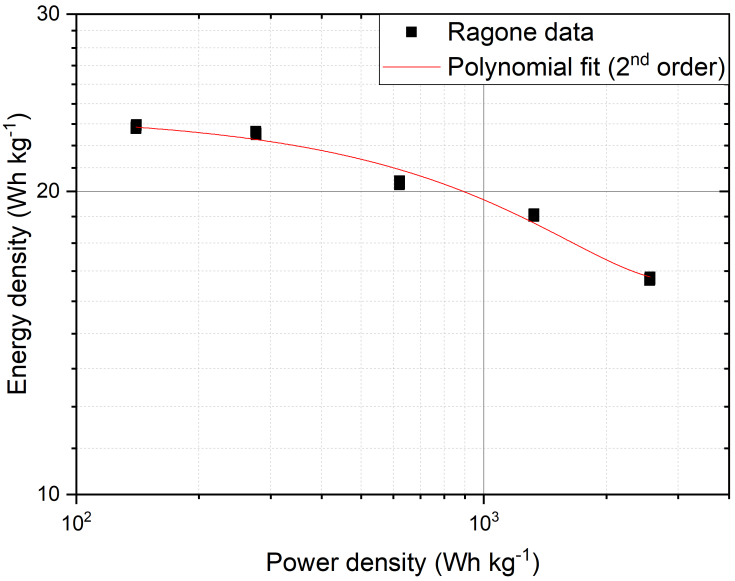

Figure 8.7: Ragone plot of the AC/AC coin cell device. The raw data were fitted with polynomial fit at 2^{nd} order, in order to roughly evaluate the trend.

The cyclic stability of the device at repetitive charge and discharge cycles was tested. The process is to evaluated the response of the device to an accelerated degradation. The number of cycles considered were 5000 at a fixed current rate of 0.5 A/g. Over time, as Figure 8.8 shows, the time of charge/discharge is reduced, with an overall increase in the iR-drop from an initial 96.46 mV to a final 261.45 mV, which is actually the reason of GCD time shortening. Despite the three times

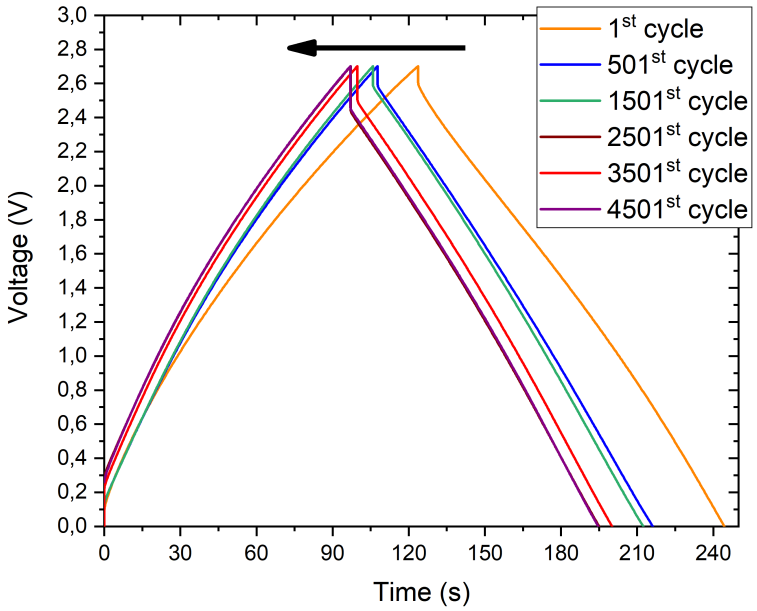

Figure 8.8: Variation of GCD during cyclic stability test of AC/AC coin cell device.

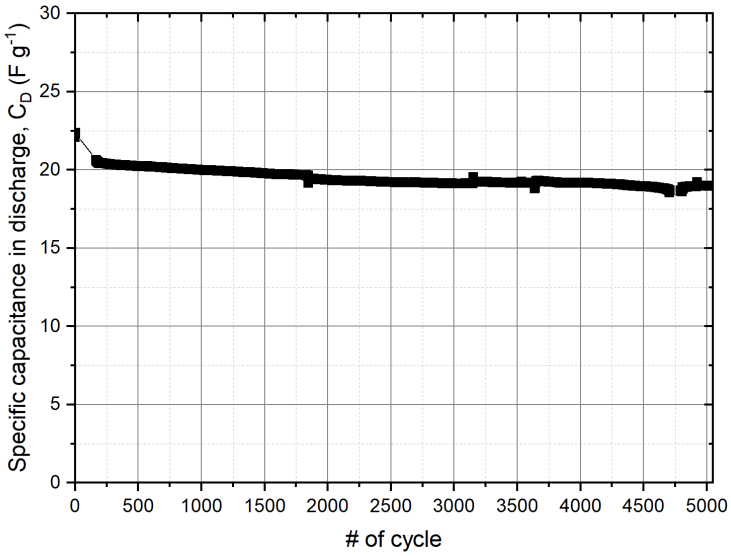

Figure 8.9: Capacitance retention of the AC/AC coin cell device among GCD cycles.

higher value obtained, the profile of the GCD is still rectangular, and the iR-drop is acceptable.

The overall capacitance was around 20 F/g, a little bit lower than the one found before, and the capacitance retention was kept over 90 %, which is good in comparison to the number of cycles.

To conclude the analysis of device response to accelerated degradation, since cyclic stability provided good results, float test (FT) was also performed. After 50 cycles of C/D, performed with constant current of 0.5 A/g, the device voltage was kept to its maximum for over 20 hours. The purpose of this test was to evaluate capacitance retention over time instead over number of cycles. GCD profiles during FT are plotted in Figure 8.10. As it happened before, the main consequences related to this test are GCD shortening of time and increase in the iR-drop, from 104.51 mV up to 213.46 mV.

The effect of float test in these case are major in terms of capacitance retention, since just after the first test, the retention evaluated was 89 %, while after 160 hours of FT the device can be considered no longer functional due to the 44 % of retention.

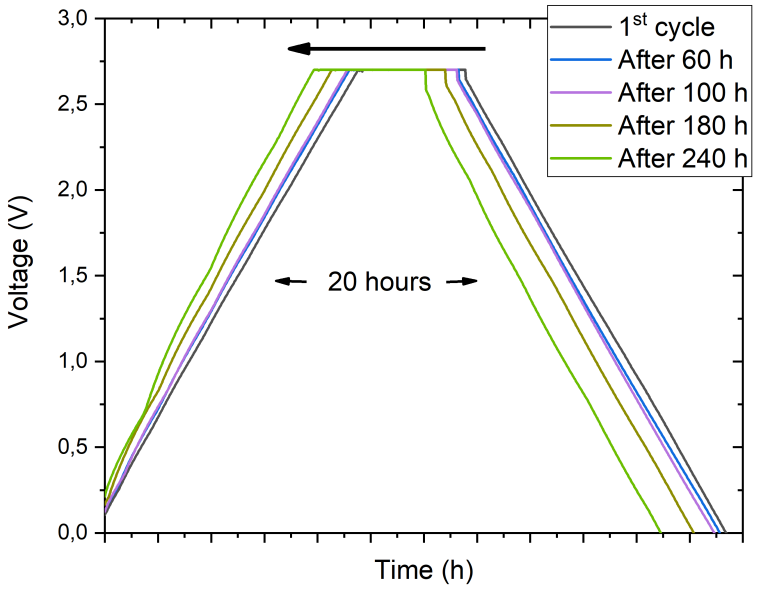

Figure 8.10: Variation of GCD during float test of AC/AC coin cell device.

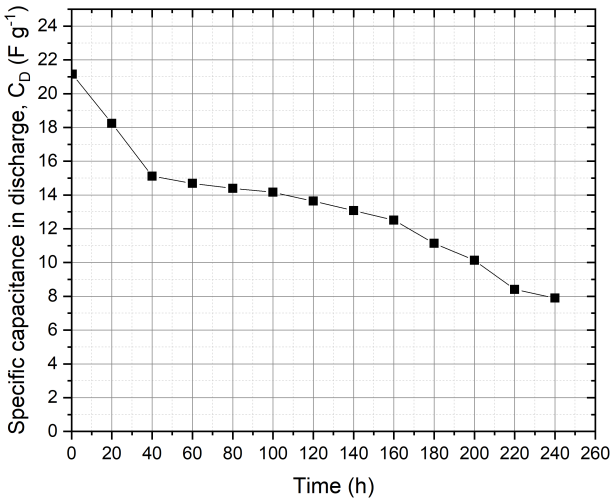

Figure 8.11: Capacitance retention of the AC/AC coin cell device over time.

8.2.3 Scaled device

Tests were performed also for the bigger device (pouch cell), to test the concept of scalability, even on a small scale. All the tests made for that case were the same as before. The CV shape shows a more resistive contribution, mainly related to IR since in this case there is not a fast drops to negative current during the first seconds of discharge. That statement is in part confirmed by the Nyquist plot, in which despite the low ESR of 0.24 Ω the diffusion line doesn't follow a straight line, increasing drastically the IR up to 3.26 Ω.

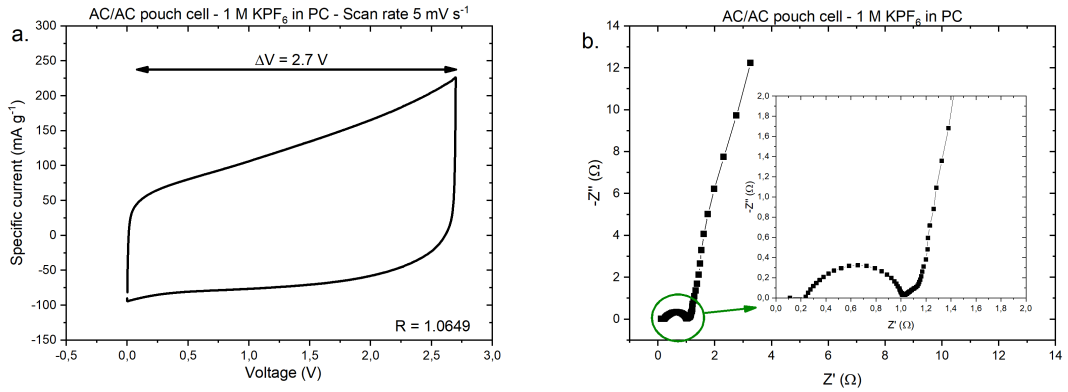

Figure 8.12: AC/AC pouch cell device. (*a*) CV from activation cycles and (*b*) Nyquist plot.

Figure 8.13 reports the profile for each current rate. Even if the triangular shape is confirmed, what immediately springs to mind is the higher iR-drop variation among the currents, whose values are 107.2, 228.0 and 626.3 mV for the first three, and 1.19 and 1.99 V for the two highest rate. These values are not remotely comparable with those obtained in coin cell, and seems that the highest current rate that the device can hold is only 0.2 A/g, comparing it with the coin cell results. All these drawback can be searched in the device assembly. After some tests, it was found that a mono-layer into the self-made coffee pocket was too sensible to vibrations, since the vacuum sealing wasn't able to provide enough contact pressure to these too-thin foils. For the coin cell, there was a spring whose rules was to provide this contact pressure between the electrodes and the separator, while for the pouch it was assumed that the pressure given by the vacuum was sufficient.

Also, efficiencies and specific capacitance confirms this trend, as Figure 8.14 shows. The first two rate are comparable with the two highest one evaluated in the coin cell system, even if the values of the capacitance are lower

The bad performance of this device is more evident in the Ragone plot (Figure 8.15). Whereas in the previous case there was a drop in energy towards power

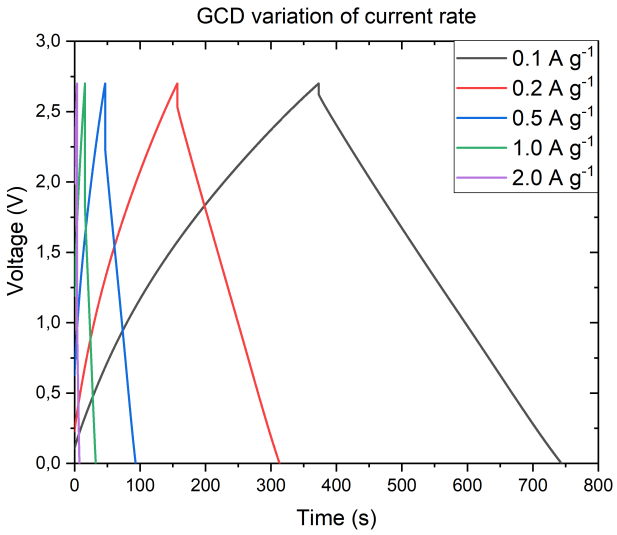

Figure 8.13: GCD of the AC/AC pouch cell device at different current rate.

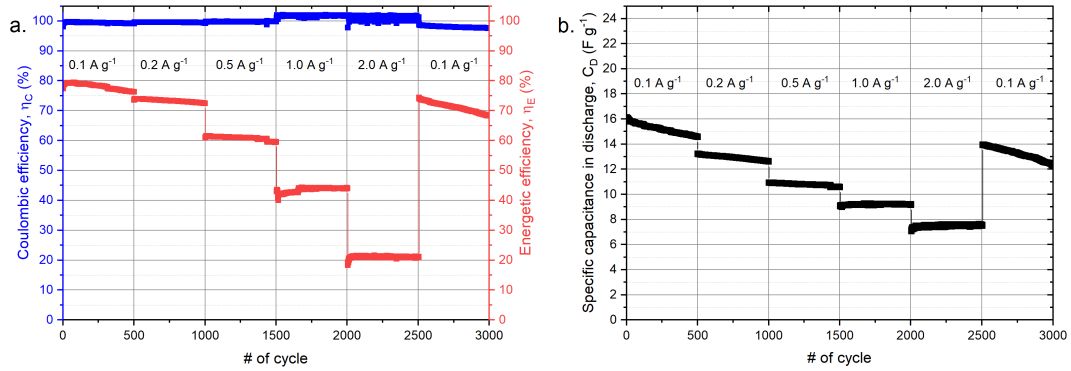

Figure 8.14: AC/AC pouch cell device. (*a*) Variation of coulombic and energetic efficiencies w.r.t current rate and cycles. (*b*) Capacitance retention of the device with different current rate.

densities greater than 70%, in this case the drop is an order of magnitude. Moreover, both energy and power are drastically decreased compared to those calculated for the coin cell system. These inefficiencies are the direct consequence of a significant increase in the device's internal resistance, which not only lowers performance but also reduces its life expectancy. These considerations must necessarily be taken into account when making the transition from small to large scale.

The cyclic stability of the pouch cell was tested under the same conditions used

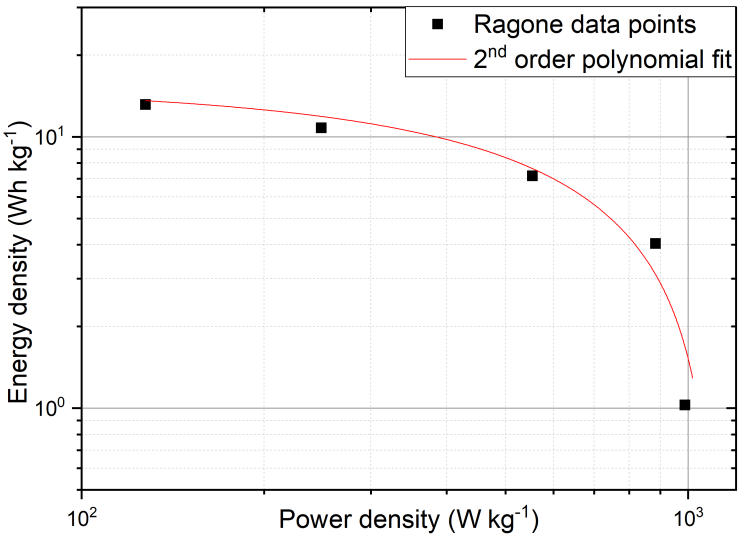

Figure 8.15: Ragone plot of the AC/AC pouch cell device. The raw data were fitted with polynomial fit at 2^{nd} order, in order to roughly evaluate the trend.

for the small device. As expected, the change in iR-drop is significant already after the first few hundred cycles. It went from an initial value of 202.5 mV to intermediate values of 371.7 mV and 454.4 mV and increased to 606.9 mV, comparable with that obtained in the previous test. The first consequence of this increase is a decrease in charge and discharge time, as well as a drastic drop in energetic efficiency. The low stability of the device to a considerable number of C/D processes can be deduced from these results.

Parallel situation was noted regarding capacitance retention. After a noticeable drop in the first few cycles, which could only be attributed to the activation of the device, after 5000 cycles the retention settled down to 80 %, which is slightly lower than that assessed in the case of the coin cell. It is to be assumed that although the device's capacitance depends on the internal electrode resistances, its decrease after countless C/D cycles leads to its stabilisation in any case. The intensity of this decrease is in any case to be attributed to the intensity of the device's parasitic resistances.

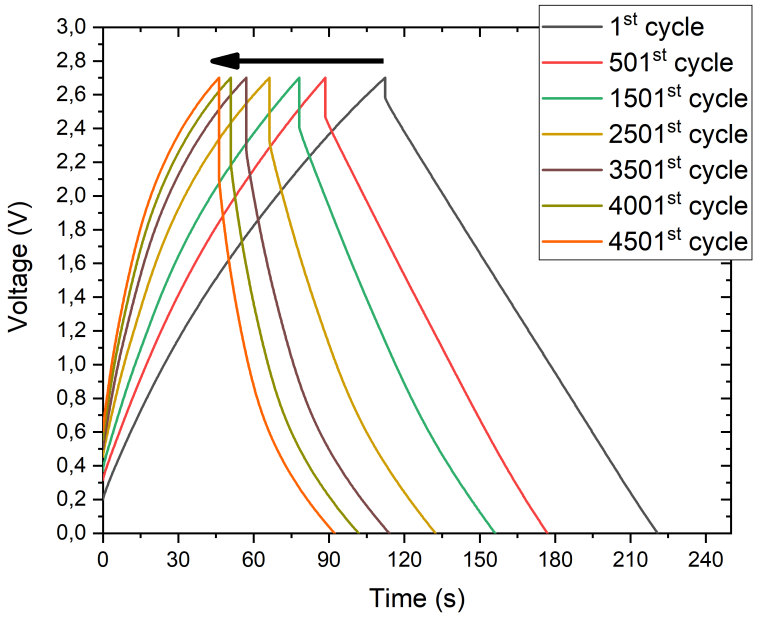

Figure 8.16: Variation of GCD during cyclic stability test for the AC/AC pouch cell device.

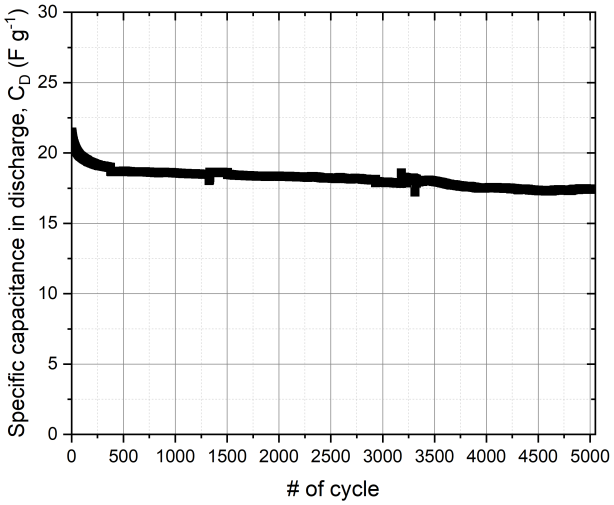

Figure 8.17: Capacitance retention of the AC/AC pouch cell device among GCD cycles.

8.3 Asymmetric MnO_2/AC device

8.3.1 Setup

As it was made for the symmetric AC/AC device, considerations about electrode mass choice were made. According to the characterization made of the two electrodes in 0.8 KPF_6 in EC:DEC, taking the maximum potential applicable for both, the final voltage will be 2.8 V, slightly higher w.r.t. the AC symmetric device. Due to the different OCP, the expected final one of the device will be the difference between the two of them, so around 400 mV. Using the Equation 8.3 and the evaluated parameters from characterizations, the mass ratio is:

$$\Pi_+ = \frac{m_+}{m_-} = \frac{1.5V \cdot 80.76F/g}{0.9V \cdot 44.49F/g} = 3.0254 \tag{8.6}$$

The choice of electrodes that respected this ratio was difficult, as the minimum mass loading limit obtained for the AC electrodes was 1.59 mg/cm^2 and the MnO_2 electrode should have a triple mass, the which exceeded the maximum mass loading limit such as to have a homogeneous structure without the presence of breakages (4.2 mg/cm^2). Considering that for small electrodes, such as those used for coin cells, the mass variations are higher, it was possible to respect this mass ratio, at least on the small scale, while for pouch cells the maximum ratio achieved did not exceed 2.2, which is in agreement with the mass loading values calculated previously.

The final specific capacitance expected, using again Equation 8.5, is 14.34 F/g, way lower than the symmetric AC device, due to the lower capacitance provided by MnO_2 electrode.

8.3.2 Small device

As a first characterization of the asymmetric device, small device was tested. From the activation cycles are reported the CV and Nyquist plot, in Figure 8.18.

The OCP evaluated is 332 mV, which is a bit less than the one expected. However, fluctuation of its value when single electrode was characterize in different measurements was not negligible, so this value is still acceptable. The shape of the CV is similar to that obtained with the symmetric device, with an accentuated current peak even towards 0 V. As in the previous case, the intensity of the two peaks gradually decreases with the activation cycles. However, during the first discharge phase, there is no drastic drop in current as occurred in the case of the small symmetrical AC device. This absence led to the assumption of a greater contribution in terms of internal resistance, which is in agreement with the resistance values found during the characterization of the single electrode of

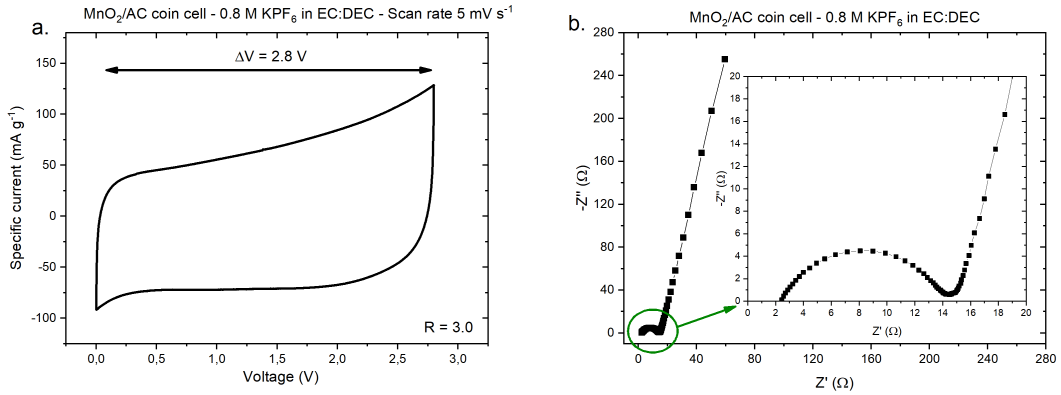

Figure 8.18: MnO_2/AC coin cell device. (*a*) CV from activation cycles and (*b*) Nyquist plot.

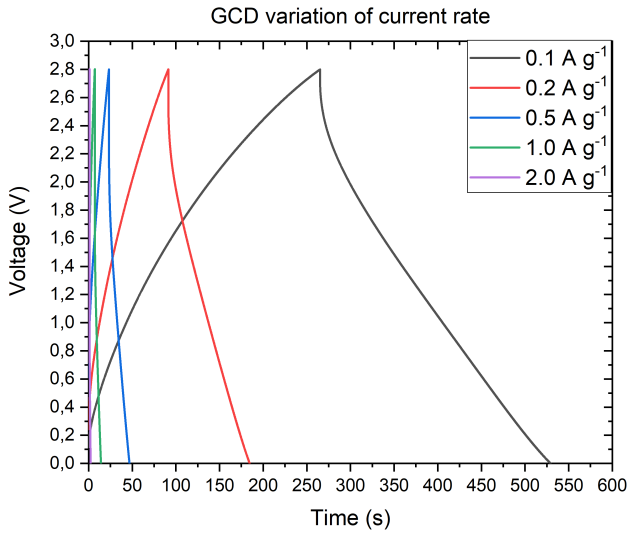

Figure 8.19: GCD of MnO_2/AC coin cell device at different current rate.

MnO_2. These assumptions are partly confirmed by the Nyquist plot, where the IR is almost three times greater (59.47 Ω) than that obtained in the other device. As has been noted in single electrode impedance spectroscopy, also in this case the presence of the semicircle at high frequencies is marked.

GCD with different current rate is shown in Figure 8.19. The voltage trend over time is no longer linear but takes on a more curved shape, and this respects the fact that there is no longer only EDLC type contribution but that of a pseudocapacitive type also takes over. A more linear trend is noted mainly during discharge profile.

As assumed during the CV analysis, the variation of the iR-drop is notable between one rate and another. Already from the lowest rate its value is 116.2 mV, an order of magnitude larger than its AC/AC counterpart. Furthermore, the values found in the other rates were 242.8 mV, 615.7 mV, 1.1 V and 1.9 V respectively.

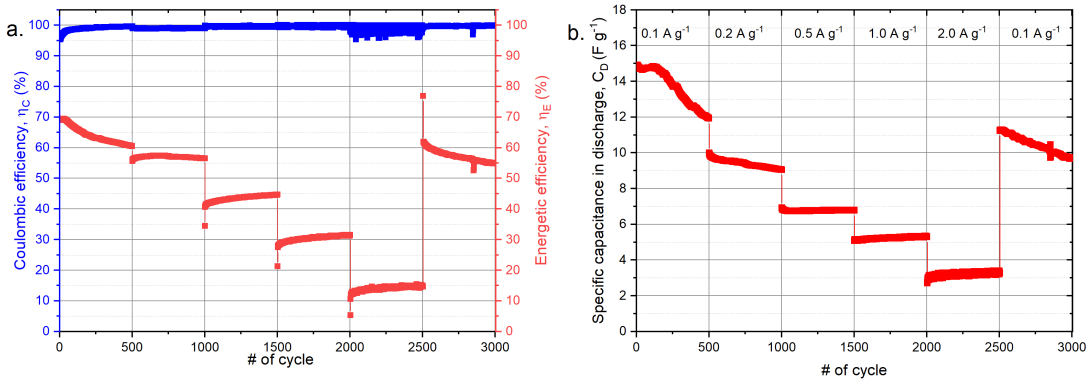

Figure 8.20: MnO_2/AC coin cell device. (a) Variation of coulombic and energetic efficiencies w.r.t current rate and cycles. (b) Capacitance retention of the device with different current rate.

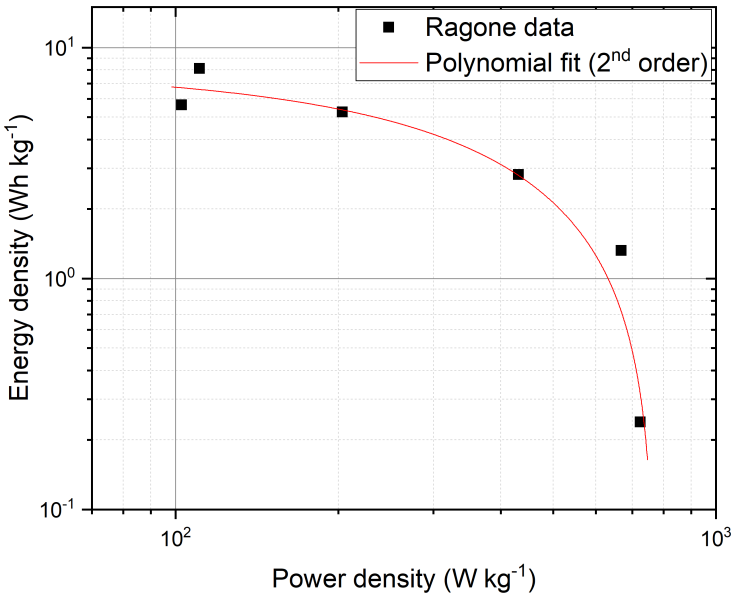

Figure 8.21: Ragone plot of MnO_2/AC coin cell device. The raw data were fitted with polynomial fit at 2^{nd} order, in order to roughly evaluate the trend.

As happened in the case of the symmetric pouch cell device, the rates that allow

the device to function correctly without having an excessive resistive contribution are the first three. Even looking at energy efficiency it is possible to confirm the previous statement. Furthermore, since for the highest rates iR-drop is too large compared to the applied voltage, the coulombic efficiency presents a notable variation in the range between 95 and 99% between one cycle and another, in addition to an energy efficiency less than 30% most of the time. The specific capacity evaluated in the first rate is slightly lower than that calculated previously, but the main problem is the instability along the various C/D cycles. Stability is achieved only in the highest rates, whose values do not correspond to initial expectations.

Ragone plot is reported in Figure 8.21. The resistive contribution of the device is most marked by the drastic drop in energy density at larger powers. This drop is more than an order of magnitude between the two limits. Furthermore, there is a notable variation in the powers and energies calculated in the last rate, and this is also due to the instability of the iR-drop in the various cycles, significantly changing the charging and discharging periods. This variation is marked even in the lowest rate, confirming the instability assumed in the first analysis.

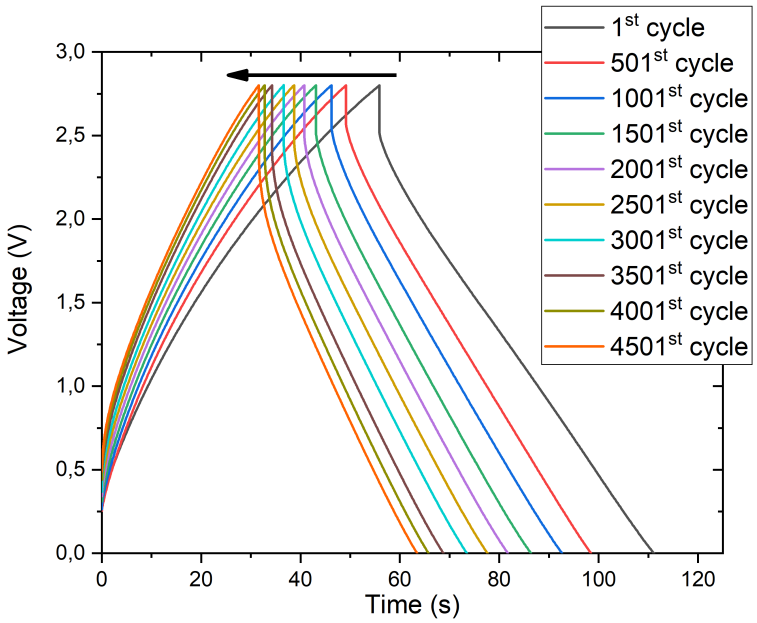

Figure 8.22: Variation of GCD during cyclic stability test for MnO_2/AC coin cell device.

Despite the conclusions dictated previously, to define terms of comparison between the various devices, the cyclic stability was evaluated again at a rate of 0.5 A/g. GCD variation among the cycles is reported in Figure 8.22. As happened in

the case of the symmetric device, the increase in iR-drop is marked in the various C/D cycles. We go from an initial value of 285.9 mV, moving towards intermediate values of 310.2 and 374.2 mV, up to a final value of 490.1 mV, almost double the first. As before, the shape of the GCD shows a non-linear trend in all cycles considered. Capacitance retention (Figure 8.23) set at 70 %, which is still low compared to those obtained for the AC/AC device, but considering the problems found, it's still acceptable.

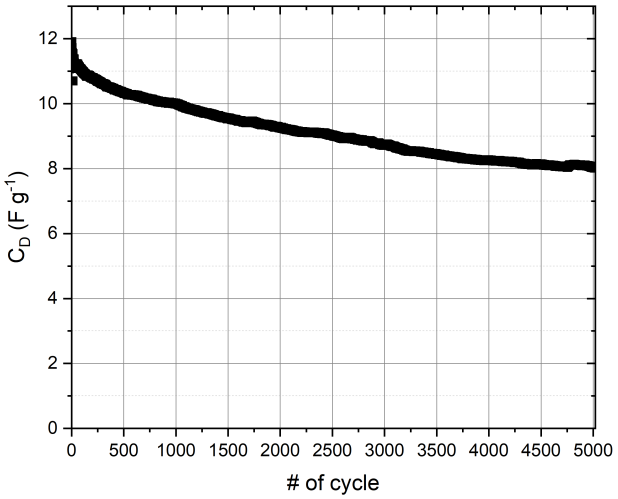

Figure 8.23: Capacitance retention of MnO_2/AC coin cell device among GCD cycles.

The performance of this device is not such as to take into account a scalability process, even on a small scale. Furthermore, the scalability process used did not bring good results compared to those obtained on a small scale, due to the problems encountered during its development. An attempt at scalability was carried out anyway, but as expected it was not possible to obtain results that were comparable with those obtained so far. Furthermore, it presented relative problems regarding its stability after a few charge and discharge cycles.

8.4 Hybrid AC/CB device

8.4.1 Setup

As regards the hybrid device, charge balancing is more to be investigated, since however simple and reductive the method is, it does not take into account the

charge accumulation method. If on the one hand we have an EDLC electrode which exploits the separation of charges, on the other both EDLC-type, albeit in minimal quantities, and redox-type reactions occur, in which the latter uses the intercalation of ions in the structure. Since the processes are distinct, it turns out to evaluate the Equation 8.1 simply using the ratio between specific capacity in charge and discharge:

$$\Pi_+ = \frac{m_+}{m_-} = \frac{Q_-(mAh/g)}{Q_+(mAh/g)} \tag{8.7}$$

According to the evaluated capacity for both the electrodes, it turns out that:

$$\Pi_+ = \frac{m_+}{m_-} = \frac{388.35mAh/g}{26.96mAh/g} = 14.4046 \tag{8.8}$$

which is impossible to reach with the electrode made in this thesis. It turns out that for that device it was impossible to define a right mass ratio, therefore as a procedure it was chosen to use the highest ratio obtainable with the electrodes under consideration.

According to the potential boundaries evaluated through characterization, the maximum voltage applicable is 3.6 V

8.4.2 Small device

Activation cycle and EIS are reported in Figure 8.24. From 0 V to 2 V there is a purely EDLC-type contribution, the intensity of which is negligible compared to that obtained with only EDLC-type electrodes. This is because the capacitive contribution of the Super C65 electrode is minimal compared to that of the AC, therefore with two capacitors in series the one with the lower capacity prevails. From 2 V upwards the faradic contribution of the cathode electrode begins, with a current increase of up to 350 mA/g, a much higher value than the symmetric (AC/AC) and asymmetric (MnO_2/AC) counterparts. During the discharge phase, the current almost immediately reaches negative values, but the intensity is not comparable with that obtained during charging, leading to a coulombic efficiency of no more than 50 %. Also it's noted a slight current peak towards the lowest potential. Due to that unwanted peak, the settings were changed in order to bring the voltage back to OCP instead of 0 V, which for this device was around 196 mV. In subsequent cycles, the intensity of charging and discharging in the range between 2 V and 3.6 V is significantly reduced. However, a settlement of the coulombic efficiency above 60 % was reached. Regarding the impedance, the ESR is decreased compared to the other cases, but due to the CB electrode, the IR is not remotely comparable (685 Ω).

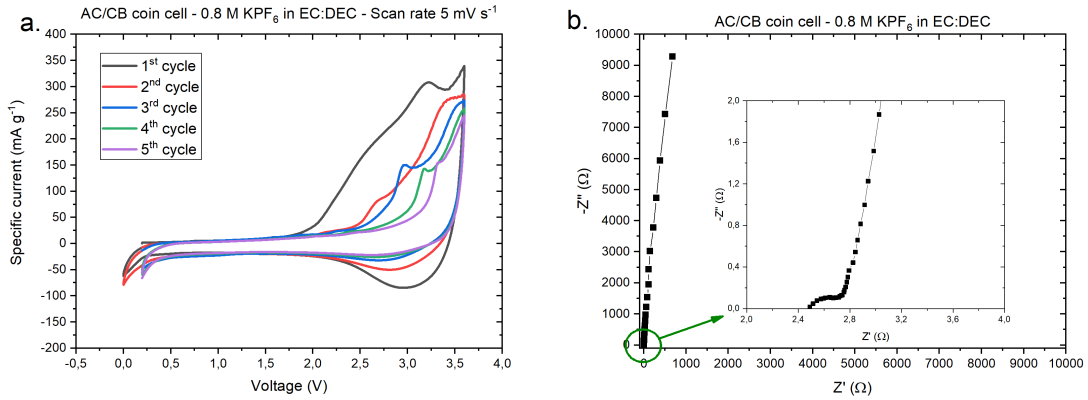

Figure 8.24: AC/CB coin cell device. (*a*) CV from activation cycles and (*b*) Nyquist plot..

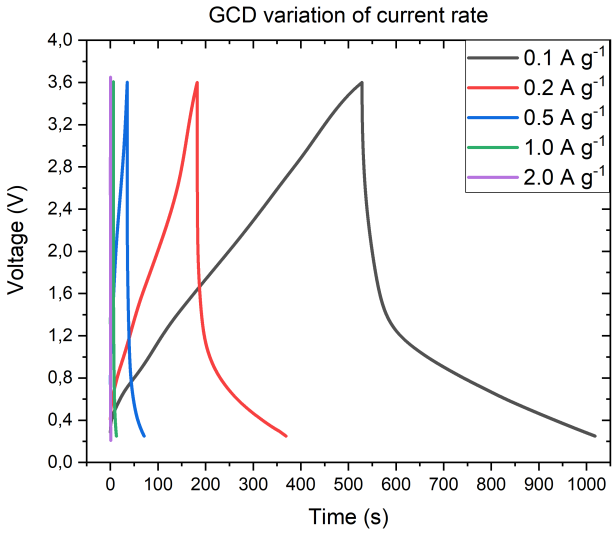

Figure 8.25: GCD of AC/CB coin cell device at different current rate.

Despite the not good expectations after the first analyzes of the device, the measurement of variable current rate was carried out, with the same settings as the previous two cases except for the lower limit, set at OCP instead of 0 V. In Figure 8.25 are reported the profiles of GCD. The almost linear growth during the charging phase leads to the assumption that the major contribution is due to the AC electrode. During the discharge, a sharp drop in voltage was noticed after the first few seconds. This drop is not to be understood as relating to the iR-drop, as in the first rate it was estimated at 86.6 mV, but relating to a significant loss of

accumulated charge. This behavior was found to be repetitive over all cycles. The iR-drop variation in the other rates were evaluated as 207.7 mV, 542.8 mV, 1.11 V and 2.34 V.

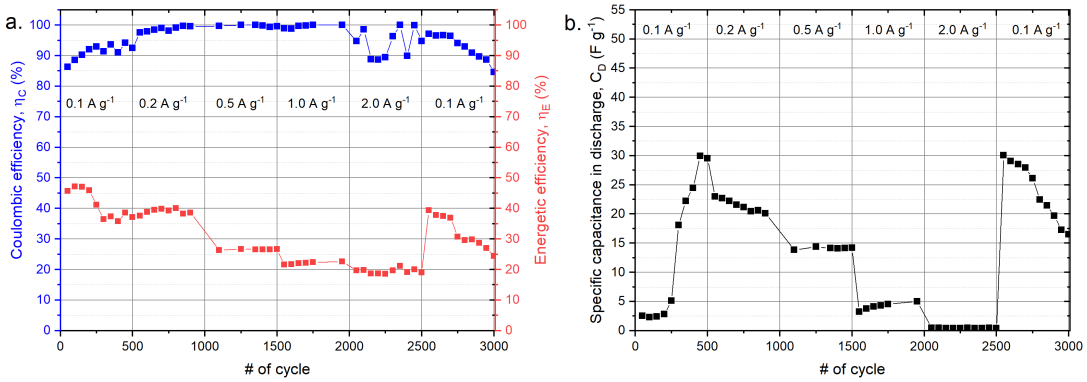

Figure 8.26: AC/CB coin cell device. (a) Variation of coulombic and energetic efficiencies w.r.t current rate and cycles. (b) Capacitance retention of the device with different current rate.

Due to this drastic drop in potential during the discharge phase, the energy efficiency does not exceed 50 %. Furthermore, due to these sudden changes in voltage, which do not appear to be constant in the various cycles, the efficiency Coulombic does not appear to be stable but presents fluctuations that are uncorrelated with each other, even leading to values greater than 100 %, which is physically and mathematically impossible and therefore to be attributed to instrument errors. It should be noted that this instability has repercussions on the estimated value of specific capacity, which seems to reach values around 30 F/g but subsequently decreases to lower values, up to the striking case of the highest rate in which it does not even exceed 1 F/g.

As a matter of comparison, Ragone plot of hybrid AC/CB configuration is reported in Figure 8.27. The high dispersion of the energy and power values for each rate led to an estimate of the trend with a high error rate. In addition, the energy density values drop by more than an order of magnitude for higher power densities.

8.4.3 Further investigation

Since the treatment of this last device has not been completely explored, more complete investigations have been carried out in this regard.

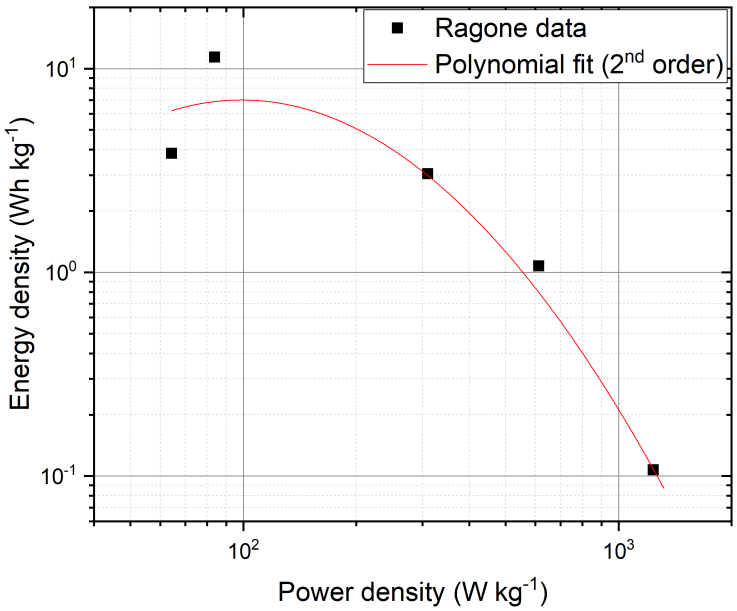

Figure 8.27: Ragone plot of AC/CB coin cell device. The raw data were fitted with polynomial fit at 2^{nd} order, in order to roughly evaluate the trend.

Intercalation test

During the development of this device, the concept of intercalation was never considered, as the required process is not always scalable and always requires a quantity of K ions coming from an expendable layer or from the anode of the cell itself[30], which in battery systems it always has an excess of ions. In the case in question this availability is not present, as the electrodes are mainly carbon-based. The only source of K ions is due to the electrolyte itself, which however requires these ions for the device to work correctly. Knowing this concept, an intercalation process has been studied in the literature[30] based on the availability that the electrolyte can provide to the intercalation process. However, since this availability is more limited compared to an external source of ions, such as an expendable layer or the anode itself, it was decided to significantly increase the quantity of electrolyte inside the cell so that the quantity of ions remains such as to allow the device to function even after intercalation[30]. This type of process is much simpler as it does not require disassembly of the cell to remove worn sacrificial layers, but only additional activation steps before its use. The intercalation process consists of periods of charging at progressive voltages up to the calculated maximum value followed by moments of relaxation in which no voltage or current is applied.

This test was performed into a pouch cell with as separator GF/D, since it provide an higher quantity of electrolyte w.r.t. to the thinner Celgard 3501 one.

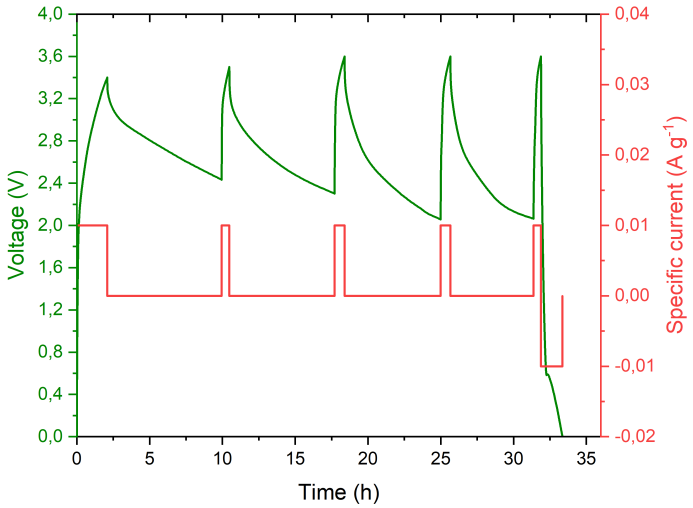

Figure 8.28: Voltage VS Time during charge/relaxation step of the intercalation test of K-ion using as source the electrolyte salt KPF_6.

Even if from previous test assembly of a pouch cell didn't provide nice results, in that case it was more suitable since the higher thickness of the separator together with the vacuum sealing provided enough contact pressure between the two micrometric electrodes. The current chosen for the intercalation test was 0.01 A/g, as to avoid resistive contribution and enhance the intercalation process. The profile of the voltage across time is reported in Figure 8.28. The progressive voltage values chosen were 3.4 V, 3.5 V and finally 3.6 V. In agreement with the profiles found in the literature[30], the charge time is faster up to 2 V, while moving forward the voltage start to slowly increase until the limit imposed. During discharge time, the voltage drops significantly up to 3 V, while the trend start to decrease until it stopped in the range between 2 and 2.4 V. As it was stated before, this potential drop cannot be attributed to a high iR-drop, as in this case it was estimated to be equal to 3.1 mV, but to a rapid discharge of the CB electrode in the first seconds of discharge. The fast discharge started to increase significantly as the maximum voltage increased. All the profile found were in agreement to the one expected.

In order to evaluate the effectiveness of this step, multiple GCDs at the same current rate were performed, and the profiles are reported in Figure 8.29. Those reported were sampled from those carried out in reality. The first change noticed in the first cycles was regarding the charging tendency in the first voltage values, in which there is no longer a rapid charge but a more gradual process. The potential drop during the discharge, however, still remains an excessive factor.

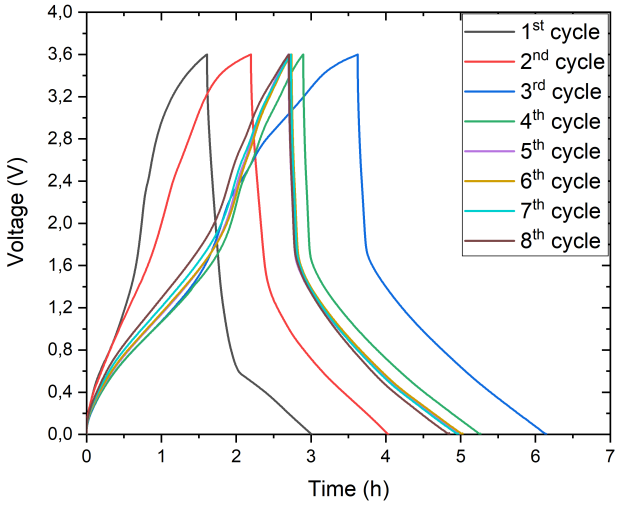

Figure 8.29: Evaluation of single potential of both AC and CB electrodes

In the subsequent cycles it's noted an increase in charging and discharging times and the profile during charging begins to no longer present the sudden increase in voltage up to 2 V. Furthermore, the rapid discharge of the CB electrode decreases in the various cycles to follow, leading to the statement that this intercalation process has effectively modified its structure, changing its performances. From subsequent cycles, the GCD appears to have stabilized, maintaining a profile similar to subsequent ones with reduced charging and discharging times.

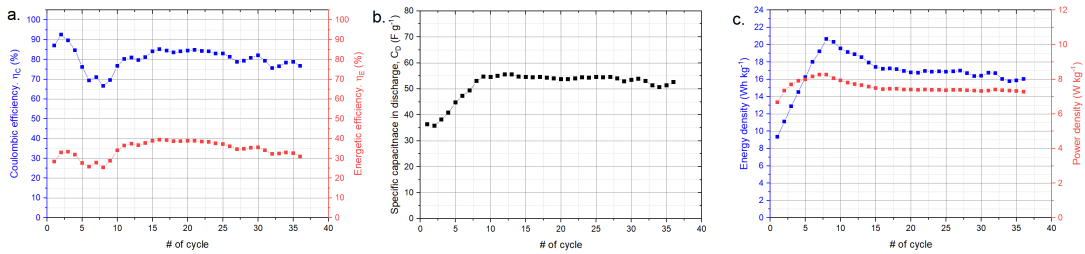

Figure 8.30: All the evaluated parameters of the AC/CB pouch cell device after intercalation. In order: (*a*) coulombic and energetic efficiency, (*b*) specific capacitance in discharge, (*c*) energy and power density w.r.t. cycles.

All the evaluated parameters of this device are reported in Figure 8.30. Despite an initial drop in coulombic and energy efficiencies, their values settled at values above 80% and 30% respectively, however presenting a decline in the final cycles.

As regards the energy density, an improvement was obtained compared to the case without intercalation, even if the power values are not remotely comparable with the others obtained, and this is due to the different current rates.

Differential potential of the electrodes

Since the previously analyzed GCD profile was not fully understood, a 3-electrode measurement was performed, with the AC electrode as WE, the CB electrode as CE and the OCE as reference. The separator used in this test was again glass fibre, this to provide a greater quantity of electrolyte to the system. The measurement consisted of a first charging phase at a very low constant current (0.01 A/g) until reaching 3.1 V, a value found by the sum of the maximum potential of the AC electrode and the 2 V obtained by the CB electrode without the final current peak, maintaining this voltage until the accumulated charge exceeded half of the estimated specific capacity of the CB electrode ($\sim$ 200 mAh/g) and finally relax the cell for 4 hours, with no current and potential applied. The profile of potential are reported in Figure 8.31. As expected, the WE electrode charged itself until almost 1.1 V, while the CE reached the 2 V upper limit. It's noted that the rapid growth in potential of the device was mainly due to CB electrode, since it is the easiest to polarize in the voltage range in which it works as an EDLC type electrode.

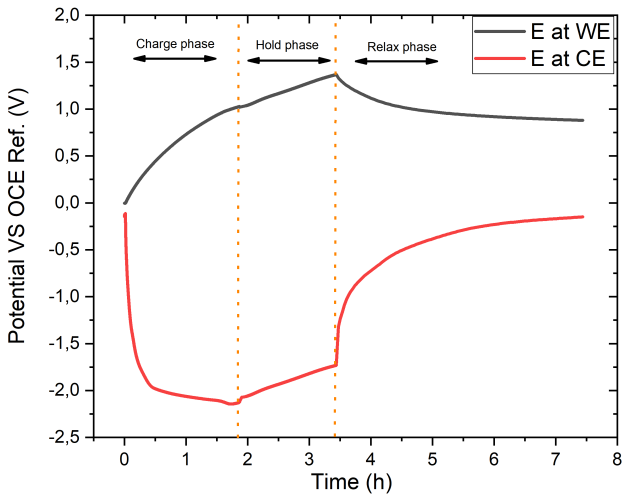

Figure 8.31: Evaluation of single potential of both AC and CB electrodes.

During the hold phase, the AC electrode begins to increase its potential up to values of 1.3 V, while the CB electrode, with the same tendency evaluated in the

other electrode, decreases until it reaches 1.8 V. This behavior, in accordance with the characterizations made regarding the AC electrode, it is a factor that leads to its degradation, as it is exiting the ESW. When there is the relaxation phase, as hypothesized in the other measurements, the abrupt drop in potential mostly concerns the CB electrode, while the AC electrode presents the classic discharge profile of a capacitor with a time constant lower than to that found for the CB electrode. This behavior leads to the inference that the CB electrode is not reliable for this type of device, at least without processes that correct these charge losses.

Chapter 9

Conclusions and future developments

9.1 Conclusions

The scalability process of a SC is a complex challenge from every point of view. The study required analyzing the electrode manufacturing process and their characterization to understand the best configuration suitable for them, between the choice of the electrode itself and the maximum applicable voltage. From the study of rheology, a marked dependence on temperature was found regarding the slurries, which leads to the assumption of keeping the ambient temperature fixed in order to avoid such variations. In accordance with the studied theory, the variations in the electrode coating mainly depend on the amount of solvent used for the preparation of the slurry, the type of active material used and the distance between the blade and the contact surface. From the calculated variations it is possible to predict the thickness and mass of the final electrode when the manufacturing process is subsequently repeated on a large scale. According to the methodology used for the electrode manufacture, calendering didn't provide improvement in the overall performance. From the characterizations it was possible to identify the performance of the individual electrodes in response to variations in potential, anodic or cathodic as they are, quantifying them. Taking these parameters into consideration, it was possible to identify the possible configurations between multiple electrodes of the same type or not, additionally evaluating the concept of charge balancing, which made it possible to further increase the performance of the individual SCs. In order to evaluate the concept of scalability of the final device, small (coin cell) and medium (pouch cell) scale measurements were carried out in order to determine the advantages and disadvantages, also evaluating the possible problems of such scalability.

The final results of this thesis were three different devices, whose parameters are reported in Table 9.1. Despite the idea of using asymmetric devices to increase the performance of the supercapacitor in question, at present the device that provided the best performance was the symmetric one with carbon-based electrodes, since according to Figure 9.1, it is the one with the highest energy and power density. In a situation in which the parasitic resistance of the medium device are reduced, its Ragone plot could be ideally superimposed on that of the small device one. As a future perspective in exploiting asymmetric and/or hybrid systems, the common idea is to minimise parasitic resistance contributions in order to increase energy density and, directly related, power density.

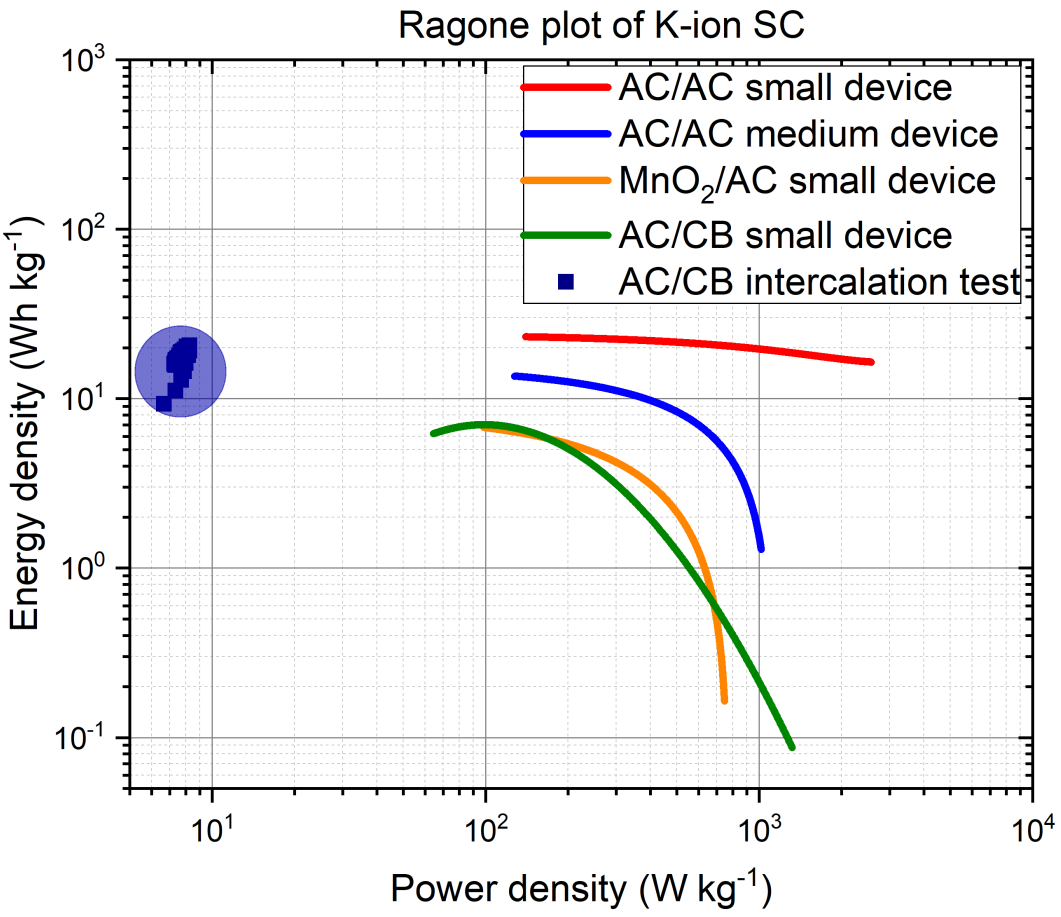

Figure 9.1: Ragone plot with all the device of this thesis.

Table 9.1: Summary of the main parameters evaluated of the devices studied.

	ΔV (V)	**ESR (Ω)**	**IR (Ω)**	**Max. Energy (Wh/kg)**	**Max. Power (kW/kg)**
AC/AC small device	2.7	3.0	28.3	25.0	2.5
AC/AC scaled device	2.7	0.24	3.26	15.0	1.0
MnO_2/AC small device	2.8	2.4	59.5	7.0	0.7
AC/CB small device	3.6	2.5	685.7	8	1.0

9.2 Future developments

In this section are present possible developments that can be useful to optimize the devices listed above. All these are considerations made along the development of the thesis.

The choice of Super C65 as the active material for the battery-type electrode was made on the basis of a recent article, which although promising performance had not yet been used for a final device. In order to improve it, more in-depth investigations are needed regarding the mechanisms that allow it to work properly. From this, it's also necessary to delve deeper into the intercalation process, in particular regarding K-ions, the literature on which is still poorly provided.

From the analyses carried out during the choice of the separator, a positive factor was found regarding those of the cellulose type. In addition to their ease of use, they are also promising in their resistance to external stress. The fact that they were not used for the devices considered is linked to the non-reproducibility of the results obtained. Since it still presented promising results, it would be necessary to further investigate their use in hybrid devices.

The concept of scalability between small- and medium-scale devices has been strongly influenced by cell assembly methodology. This is because the self-produced package system was not suitable for the type of device considered, the thickness of the electrodes and the separator were such that they were more sensitive to vibrations and did not allow good adhesion between them. In order for this problem to be resolved, it is necessary to modify the packaging system, which may include the transition from mono-layer to multi-layer and/or the addition of spacers that allow a greater contact pressure between the two electrodes.

Bibliography

[1] Yuanlong Shao, Maher F. El-Kady, Jingyu Sun, Yaogang Li, Qinghong Zhang, Meifang Zhu, Hongzhi Wang, Bruce Dunn, and Richard B. Kaner. «Design and Mechanisms of Asymmetric Supercapacitors». In: *Chem. Rev.* 118.18 (Sept. 26, 2018). Publisher: American Chemical Society, pp. 9233–9280. ISSN: 0009-2665. DOI: 10.1021/acs.chemrev.8b00252. URL: https://doi.org/10.1021/acs.chemrev.8b00252 (cit. on p. 2).

[2] Brian Evans Conway 1927-2005 (viaf)61608743. *Electrochemical supercapacitors : scientific fundamentals and technological applications*. New York (N.Y.) : Plenum press, 1999. ISBN: 0-306-45736-9. URL: http://lib.ugent.be/catalog/rug01:000540254 (cit. on pp. 3, 10).

[3] Jianzhong Wu. «Understanding the Electric Double-Layer Structure, Capacitance, and Charging Dynamics». In: *Chem. Rev.* 122.12 (June 22, 2022). Publisher: American Chemical Society, pp. 10821–10859. ISSN: 0009-2665. DOI: 10.1021/acs.chemrev.2c00097. URL: https://doi.org/10.1021/acs.chemrev.2c00097 (cit. on pp. 3, 4).

[4] Xi Liu, Yingjuan Sun, Yong Tong, Xinyue Wang, Jiefeng Zheng, Yunaji Wu, Hongyan Li, Li Niu, and Yang Hou. «Exploration in materials, electrolytes and performance towards metal ion (Li, Na, K, Zn and Mg)-based hybrid capacitors: A review». In: *Nano Energy* 86 (Aug. 1, 2021), p. 106070. ISSN: 2211-2855. DOI: 10.1016/j.nanoen.2021.106070. URL: https://www.sciencedirect.com/science/article/pii/S221128552100327X (cit. on p. 4).

[5] Hong Tan and Xiuyi Lin. «Electrolyte Design Strategies for Non-Aqueous High-Voltage Potassium-Based Batteries». In: *Molecules* 28.2 (2023). ISSN: 1420-3049. DOI: 10.3390/molecules28020823 (cit. on p. 5).

[6] Ta-Jo Liu, Carlos Tiu, Li-Chun Chen, and Darjen Liu. «The Influence of Slurry Rheology on Lithium-ion Electrode Processing». In: *Printed Batteries*. Mar. 23, 2018, pp. 63–79. ISBN: 978-1-119-28790-2. DOI: 10.1002/9781119287902.ch3. URL: https://doi.org/10.1002/9781119287902.ch3 (visited on 01/16/2024) (cit. on pp. 6, 22, 23).

[7] Alexander Diener, Stoyan Ivanov, Wolfgang Haselrieder, and Arno Kwade. «Evaluation of Deformation Behavior and Fast Elastic Recovery of Lithium-Ion Battery Cathodes via Direct Roll-Gap Detection During Calendering». In: *Energy Technology* 10.4 (Apr. 1, 2022). Publisher: John Wiley & Sons, Ltd, p. 2101033. ISSN: 2194-4288. DOI: 10.1002/ente.202101033. URL: https://doi.org/10.1002/ente.202101033 (visited on 01/16/2024) (cit. on pp. 7, 25, 26).

[8] Mutawara Mahmood Baig, Iftikhar Hussain Gul, Sherjeel Mahmood Baig, and Faisal Shahzad. «The complementary advanced characterization and electrochemical techniques for electrode materials for supercapacitors». In: *Journal of Energy Storage* 44 (Dec. 1, 2021), p. 103370. ISSN: 2352-152X. DOI: 10.1016/j.est.2021.103370. URL: https://www.sciencedirect.com/science/article/pii/S2352152X21010616 (cit. on pp. 9, 13, 16, 18, 20).

[9] Sonia Dsoke, Xu Tian, Corina Täubert, Steffen Schlüter, and Margret Wohlfahrt‡ Mehrens. «Strategies to reduce the resistance sources on Electrochemical Double Layer Capacitor electrodes». In: *Journal of Power Sources* 238 (Sept. 15, 2013), pp. 422–429. ISSN: 0378-7753. DOI: 10.1016/j.jpowsour.2013.04.031. URL: https://www.sciencedirect.com/science/article/pii/S0378775313006253 (cit. on pp. 10, 26, 71, 76).

[10] Sanliang Zhang and Ning Pan. «Supercapacitors Performance Evaluation». In: *Advanced Energy Materials* 5.6 (Mar. 1, 2015). Publisher: John Wiley & Sons, Ltd, p. 1401401. ISSN: 1614-6832. DOI: 10.1002/aenm.201401401. URL: https://doi.org/10.1002/aenm.201401401 (visited on 01/26/2024) (cit. on p. 13).

[11] Tyler S. Mathis, Narendra Kurra, Xuehang Wang, David Pinto, Patrice Simon, and Yury Gogotsi. «Energy Storage Data Reporting in Perspective—Guidelines for Interpreting the Performance of Electrochemical Energy Storage Systems». In: *Advanced Energy Materials* 9.39 (Oct. 1, 2019). Publisher: John Wiley & Sons, Ltd, p. 1902007. ISSN: 1614-6832. DOI: 10.1002/aenm.201902007. URL: https://doi.org/10.1002/aenm.201902007 (visited on 01/26/2024) (cit. on pp. 13, 14, 18–21).

[12] John Wang, Julien Polleux, James Lim, and Bruce Dunn. «Pseudocapacitive Contributions to Electrochemical Energy Storage in TiO2 (Anatase) Nanoparticles». In: *J. Phys. Chem. C* 111.40 (Oct. 1, 2007). Publisher: American Chemical Society, pp. 14925–14931. ISSN: 1932-7447. DOI: 10.1021/jp074464w. URL: https://doi.org/10.1021/jp074464w (cit. on p. 15).

[13] Swati Sharma and Prakash Chand. «Supercapacitor and electrochemical techniques: A brief review». In: *Results in Chemistry* 5 (Jan. 1, 2023), p. 100885. ISSN: 2211-7156. DOI: 10.1016/j.rechem.2023.100885. URL: https://www.

sciencedirect.com/science/article/pii/S2211715623001248 (cit. on p. 18).

[14] *Rheology Basics: RheoStream - Fluida*. Nov. 2020. URL: https://fluidan.com/rheology-basics/ (cit. on pp. 20, 22, 41).

[15] O. Cohu and A. Magnin. «Rheology and flow of paints in roll coating processes». In: *Surface Coatings International* 80.3 (Mar. 1, 1997), pp. 102–107. ISSN: 1356-0751. DOI: 10.1007/BF02692623. URL: https://doi.org/10.1007/BF02692623 (cit. on p. 23).

[16] *Time Dependent Stability of Aqueous Based Anode Slurries with Bio-Derived Binder by Rheological Methods*. URL: https://www.tainstruments.com/applications-notes/time-dependent-stability-of-aqueous-based-anode-slurries-with-bio-derived-binder-by-rheological-methods/ (cit. on p. 24).

[17] Saleh Hasson Abud. «Porous InxGa1-xN for sensing and solar cell applications». In: *Physics USM, Malasia* (2014) (cit. on p. 28).

[18] Małgorzata Kot. «In-operando hard X-ray photoelectron spectroscopy study on the resistive switching physics of HfO2-based RRAM». PhD thesis. June 3, 2014 (cit. on p. 31).

[19] H. Buqa, M. Holzapfel, F. Krumeich, C. Veit, and P. Novák. «Study of styrene butadiene rubber and sodium methyl cellulose as binder for negative electrodes in lithium-ion batteries». In: *Journal of Power Sources* 161.1 (2006), pp. 617–622. ISSN: 0378-7753. DOI: https://doi.org/10.1016/j.jpowsour.2006.03.073. URL: https://www.sciencedirect.com/science/article/pii/S037877530600591X (cit. on p. 34).

[20] Xun Wang and Yadong Li. «Rational synthesis of alfa-MnO2 single-crystal nanorods». In: *Chem. Commun.* 7 (2002). Publisher: The Royal Society of Chemistry, pp. 764–765. ISSN: 1359-7345. DOI: 10.1039/B111723H. URL: http://dx.doi.org/10.1039/B111723H (cit. on p. 35).

[21] Przemysław Galek, Jacek Różański, and Krzysztof Fic. «Toward better porous carbon-based electrodes by investigation of the viscoelastic properties of carbon suspension». In: *Chemical Engineering Journal* 463 (May 1, 2023), p. 142476. ISSN: 1385-8947. DOI: 10.1016/j.cej.2023.142476. URL: https://www.sciencedirect.com/science/article/pii/S138589472301207X (cit. on pp. 55, 71, 76).

[22] Anetta Platek, Cristina Nita, Camélia Matei Ghimbeu, Elżbieta Frąckowiak, and Krzysztof Fic. «Electrochemical capacitors operating in aqueous electrolyte with volumetric characteristics improved by sustainable templating of electrode materials». In: *Electrochimica Acta* 338 (Apr. 1, 2020), p. 135788. ISSN: 0013-4686. DOI: 10.1016/j.electacta.2020.135788. URL: https://www.sciencedirect.com/science/article/pii/S0013468620301808 (cit. on p. 55).

[23] Peter Ruschhaupt, Alberto Varzi, and Stefano Passerini. «Natural Polymers as Green Binders for High-Loading Supercapacitor Electrodes». In: *ChemSusChem* 13.4 (Feb. 21, 2020). Publisher: John Wiley & Sons, Ltd, pp. 763–770. ISSN: 1864-5631. DOI: 10.1002/cssc.201902863. URL: https://doi.org/10.1002/cssc.201902863 (visited on 03/13/2024) (cit. on p. 56).

[24] Masaoki Oku. «X-ray photoelectron spectra of KMnO4 and K2MnO4 fractured in situ». In: *Journal of Electron Spectroscopy and Related Phenomena* 74.2 (Oct. 31, 1995), pp. 135–148. ISSN: 0368-2048. DOI: 10.1016/0368-2048(95)02374-7. URL: https://www.sciencedirect.com/science/article/pii/0368204895023747 (cit. on p. 64).

[25] Mark C. Biesinger, Brad P. Payne, Andrew P. Grosvenor, Leo W.M. Lau, Andrea R. Gerson, and Roger St.C. Smart. «Resolving surface chemical states in XPS analysis of first row transition metals, oxides and hydroxides: Cr, Mn, Fe, Co and Ni». In: *Applied Surface Science* 257.7 (Jan. 15, 2011), pp. 2717–2730. ISSN: 0169-4332. DOI: 10.1016/j.apsusc.2010.10.051. URL: https://www.sciencedirect.com/science/article/pii/S0169433210014170 (cit. on pp. 66, 67).

[26] Matthias Young, Aaron Holder, S.M. George, and Charles Musgrave. «Mechanism of Pseudocapacitive Charge Storage in MnO2». In: (June 23, 2014) (cit. on p. 85).

[27] L. Demarconnay, E. Raymundo-Piñero, and F. Béguin. «Adjustment of electrodes potential window in an asymmetric carbon/MnO2 supercapacitor». In: *Journal of Power Sources* 196.1 (Jan. 1, 2011), pp. 580–586. ISSN: 0378-7753. DOI: 10.1016/j.jpowsour.2010.06.013. URL: https://www.sciencedirect.com/science/article/pii/S0378775310009961 (cit. on p. 85).

[28] Sabrina Trano, Daniele Versaci, Micaela Castellino, Marco Fontana, Lucia Fagiolari, Carlotta Francia, and Federico Bella. «Exploring nature-behaviour relationship of carbon black materials for potassium-ion battery electrodes». In: *Energy Materials* 4.1 (2024), p. 400008. DOI: 10.20517/energymater.2023.79. URL: http://dx.doi.org/10.20517/energymater.2023.79 (cit. on pp. 99, 100).

[29] Aqib Muzaffar, M. Basheer Ahamed, Kalim Deshmukh, and Jagannathan Thirumalai. «A review on recent advances in hybrid supercapacitors: Design, fabrication and applications». In: *Renewable and Sustainable Energy Reviews* 101 (Mar. 1, 2019), pp. 123–145. ISSN: 1364-0321. DOI: 10.1016/j.rser.2018.10.026. URL: https://www.sciencedirect.com/science/article/pii/S1364032118307299 (cit. on p. 108).

[30] María Arnaiz and Jon Ajuria. «Pre-Lithiation Strategies for Lithium Ion Capacitors: Past, Present, and Future». In: *Batteries & Supercaps* 4.5 (May 1, 2021). Publisher: John Wiley & Sons, Ltd, pp. 733–748. DOI: 10.1002/batt.202000328. URL: https://doi.org/10.1002/batt.202000328 (visited on 03/21/2024) (cit. on pp. 125, 126).